Micro-structural modifications of semiconductor systems under irradiation: experiment, modeling and simulation analysis.

Giuseppe Fisicaro

PhD in Physics XXIV Cycle
Department of Physics and Astronomy
University of Catania

Tutor: Prof. Giovanni Piccitto

Supervisor: Dr. Antonino La Magna

PhD Coordinator: Prof. Francesco Riggi

Keywords: laser annealing, silicon, defects, dopant activation, dopant pile-up, simulation, modeling, Kinetic Monte Carlo.

An electronic version of this thesis, including color figures, is available at: http://dspace.unict.it/jspui/

a.a. 2008/2011

To my family

Contents

Abstract

Research on the micro-structural modifications of semiconductor systems has played a central role in the last decades. In particular, Laser Thermal Annealing receives a great interest in the formation of ultra-shallow junctions essential in nanoscale metal-oxide-semiconductor technology. An intriguing poorly understood issue is the post-implant kinetics of the defects-dopant system in the extremely far-from-the equilibrium conditions caused by the laser irradiation both in the non-melting and melting regime. For this purpose, the activation mechanism in the solid phase of phosphorus implanted silicon under excimer laser irradiation has been investigated by means of experimental analysis and modeling. The models have been originally formulated and implemented in numerical codes, which belong to the class of the continuum (based on Partial Differential Equations) and atomistic (Kinetic Monte Carlo) approaches for kinetic simulation of the dopant-defect system under laser irradiation. Continuum models will be also presented which clarified the boron non-equilibrium segregation during the fast solidification, i.e. the dopant pile-up phenomenon at the maximum melt depth. We will elucidate the dopant evolution mechanism in the melting phase considering the possibility of two different states governing the dopant diffusion in a tight temperature range around the melting temperature. Finally, an accurate study of the feasibility of laser irradiation as a heat source for real patterned substrates has been carried out for the case of SiGe and Ge based MOS devices. We developed a continuum simulation code which simulates the interaction between the laser light and the transistor periodic structure in order to estimate the heat source as well as the heat diffusion, phase changes and material redistribution under irradiation.

Introduction

Research on the micro-structural modifications of semiconductor systems started at the beginning of the 50's and the 60's. Researchers were looking to replace the electrical components of that time, namely electron tubes, turning them to semiconductor devices. This class of materials were highly valued because they could be used as diodes due to their gap on the conduction band, allowing electron- or hole-type conduction if doped with different impurities. The first semiconductor-based device was produced by Russell Ohl of the Bell Telephone Laboratories and his group. This prototype acted like an electron tube diode exploiting the conductance properties of a junction formed by two oppositely doped samples of germanium. Subsequently, John Bardeen and Walter Brattain developed a device that worked not only as a diode valve but also as an amplifier. This ”point-contact transistor” was made-up by a slice of germanium with a few carefully placed wires touching it. Development and engineering of germanium transistors was unfeasible due to a series of technological problems and researchers focused their attention on other semiconductor materials. They found the answers to the majority of these problems in silicon and its oxide SiO_2.

Silicon gained a central role in the microelectronics area thanks to its appropriate gap on the conduction band (a middle way between pure insulators and conductors), which allowed the fabrication of electronic devices on the micrometer and, nowadays, nanometer scale. On the other hand, advantages came also from the well controlled manipulation of its conduction properties by the addition of impurities.

Differently from a metal, in a semiconductor the current conduction can occur via mobile or ”free” electrons and holes, collectively known as charge carriers. An intrinsic semiconductor, not being quite an insulator, contains a small concentration of free electrons at room temperature. Since this concentration has been created by freeing electrons from bonds, an equal number of holes must also be present. The possibility of both carriers co-existing is vital to the operation of devices.

Doping a semiconductor such as silicon with a small amount of impurity atoms, such as phosphorus or boron, greatly increases the number of free electrons or holes within the semiconductor. The semiconductor material used in devices is doped under highly controlled conditions in a fabrication facility to precisely control the location and concentration of p- and n-type dopants.

Generally dopant atoms are introduced in a semiconductor substrate by means of ion implantation, being this technique the most feasible and scalable for large-scale device fabrication. The interaction between penetrating ions and the material atoms cause undesired defect cascades, just inside the implanted region. Subsequently, in order to restore the crystalline order and displace impurity atoms in substitutional positions (where they become electrically active), heat treatments become necessary. This process significantly affects the initial impurity density profile due to the thermal activated diffusion which can be modeled by means of the Fick-law. The solutions of the related diffusion equation has contributed to the predictions of the thermal process results and, as a consequence, to the accurate process control in the early generations of microelectronic devices.

However, the further developments posed new fundamental questions which did not find the correct understanding in the framework of the thermal equilibrium diffusion. Indeed, for thermal process in the time scale of few tens of seconds and below, non-equilibrium kinetics of the coupled system point defects-impurities dominate the impurity redistribution. From this point of view, an increasing interest raised on the investigation of the non-equilibrium caused by a point defect excess and in the role played by this excess in the dopant transient enhanced diffusion (TED) phenomena in Si. As a consequence, being the defect super-saturation the only relevant driving force of the non-equilibrium kinetics, the different stages (diffusion, aggregate nucleation, formation and annihilation of extended defects) of the defect evolution in

Si at quasi-constant temperature are now well known. Moreover, a consistent modeling approach has been derived and validated by experimental works [30, 71, 91].

In order to fabricate smaller and smaller microelectronic devices, the current trend of the dopant activation process in Si is characterized by an extreme reduction of the annealing time (from the ms to ns regime for the ultra-fast thermal processes) and a correspondent increase of the peak temperature, eventually using the laser irradiation (LI) as a heat source [49, 50, 70, 105]. These processes should complement or substitute the actual rapid thermal annealing in the activation module of future nanoelectronic devices.

The extreme consequences of these concepts find their realization in the laser melting processes. The advantages offered by the Laser Thermal Annealing (LTA) process in the melting regime, compared to conventional Rapid Thermal Anneal (RTA) procedures, are represented by a better control of the junction depth and a higher dopant activation efficiency. Indeed, the LTA causes the melting of a well defined region in the Si sample (with the melting depth depending essentially on the laser beam energy), where the dopant atoms redistribute themselves uniformly due to their huge diffusivity ($\sim 10^{-4}\text{cm}^2/\text{s}$ in the liquid phase), orders of magnitude higher than in the solid phase. Moreover, the non-equilibrium segregation during the fast solidification phenomenon, occurring after irradiation, enhances dopant trapping and favors the incorporation of a high density of dopant atoms in substitutional positions.

Although the junction depth can be easily defined using LTA, the control of the LTA process is far from being satisfactory. In particular, the LTA process integration in the process sequence applied to device manufacturing is critical. The most important problems concern the precise dopant profile definition in the two dimensional (2D) device geometry, the optimization of the LTA conditions (substrate temperature, pulse energy, number of pulses) on the basis of the required profile depth and shape, the effect of LTA on pre-formed structures (e.g. dielectric and polysilicon films), and the role of defects remaining after the LTA process.

As a consequence the predictions of the process results are fundamental, and we have dedicated chapter 1 to the presentation of the state-of-the-art modeling approaches of the LTA simulation, considering also particular applications to a series of experimental works which we have supported with simulations during the PhD period.

Conventional modelling [105, 106] of the dopant distribution during LTA is based on the numerical solution of the heat diffusion equation, that allows to simulate the liquid-solid interface evolution. Furthermore, the dopant diffusion is based on a sharp-interface model of the alloy solidification and a step-like change of the mass transport properties across the interface. The matching between the solutions in the liquid and solid zones at the solid-liquid interface is obtained from the mass conservation and from a segregation model ruling the jump in concentration across the interface itself. The sharp-interface model, which decouples thermal and mass evolution and does not consider the physical properties of the interface layer itself, allows only a phenomenological approach of the segregation problem. Indeed, the dependence of the segregation coefficient on the interface speed can be included by fitting the experimental results. However, an obvious computational drawback of this methodology is that the instantaneous interface position and speed should be tracked down. This introduces some limitations, in particular for the applications of 2D calculations or the cases where the whole device structure must be considered.

The phase-field methodology [3, 15] improves the physical description of the moving phase boundary problem by considering a finite dimension of the transition region between the two phases. The boundary location can be, in principle, tracked as a level set of the phase function. However, such tracking is not needed for the problem solution since phase, temperature and dopant density evolve concurrently according to three coupled differential equations. Therefore, the dopant redistribution is automatically evaluated solving the complete evolution problem. In this thesis work the phase-field method is our preferred approach to simulate thermal field and dopant density evolution during the LTA process. In spite to its rather complicated formulation, we can consider the phase-field as the ”zero order” model for the LTA simulation, i.e the analogous of the Fick diffusion law in the simulation of the conventional thermal process. It is the starting point of the model that we have originally formulated, implemented and applied during the PhD period.

Indeed, the post-implant kinetics of the defects–dopant system in the extremely far-from-the equilibrium conditions caused by the laser irradiation both in the non-melting and the melting regime is almost totally unknown and cannot be modeled with the standard phase field equations. From the theoretical point of view some relevant questions have to be addressed: the formalization of a reliable kinetic formalism for the evolving defect-impurity system in a non-uniform fast-varying thermal field [25, 26, 37, 53], the generalization of the kinetic parameters (e.g. diffusivity, clustering rate constants, etc.) in this regime, the inclusion in the formalism of eventual phase transitions [49], the interaction between the defects generated by the implant and the defects generated by the process [52].

We will present our investigation and the achieved results concerning the evolution of the dopant-defect system in implanted silicon under LTA in the chapter 2 and chapter 3 of the present thesis. The case of phosphorus doping will be dealt in detail, focusing the attention on the activation mechanism under excimer laser irradiation. For this purpose, the activation efficiency in the solid phase has been measured in a wide range of irradiation conditions, varying the laser fluence and the number of shots. The total active fraction varies in a range spanning several orders of magnitude and shows a complex trend depending on the process conditions. We investigated this system developing a continuum models, formed by a set of coupled Partial Differential Equations (PDE model), which allow for an accurate determination of thermal fields and melting evolution by means of the phase-field methodology [41, 49, 50]. This last equations have been coupled with a diffusion-reaction model which can simulate the evolution of the dopant-defects system during the annealing process [25, 26, 37, 53]. Our continuum model will be able to explain the whole scenario[25, 26].

In the second part of chapter 3, we will discuss widely our investigation on the dopant evolution mechanism in the melting phase of boron implanted silicon under laser irradiation. In particular, laser processes where the maximum melt depth is much larger than the implanted B ion projected range are considered (i.e. the implantation defects are fully annihilated by the melting). Experimental analysis suggests that the dopant evolution and its redistribution in the molten regions can be divided in three different regimes as a function of the laser fluence (or the maximum melt depth): against-gradient, pile-up and no-pile-up regimes. We will elucidate the dopant evolution mechanism in the melting phase considering the possibility of two different states governing the dopant diffusion in a tight temperature range around the melting temperature.

We will try to demonstrate that simulations of laser processes are crucial in order to understand the effects of irradiation on material modification both in the melting and solid phase. It is due to the intrinsic features of the laser annealing processes (evolution of bulk and surface material properties on a scale less than micro and nanoseconds). Within continuum models the entire physics of the system is formulated as a set of differential equations ruling the density field kinetics of each particle considered to be relevant in the process. This technique has the advantages to be easily implemented in commercial simulation tools with a quick setting of the problem. Moreover, in general, the simulation time is short and large systems can be studied by adjusting the grid used for the spatial discretization of the equations.

Most of these limitations can be overcome tackling the problem with a Kinetic Monte Carlo (KMC) approach. In this way, there are no limitations in the number of interactions between dopant atoms and defects. A detailed dopant clustering can be considered as well as dopant-defect cluster complexes (in a explicit way than done until now). At the same time, great part of the parameters will be directly extracted from atomistic calculations. We have developed an innovative KMC code, which rules the post-implant kinetics of the defects-dopant system in the extremely far-from-the equilibrium conditions caused by the laser irradiation both in the non-melting, melting and partial melting regimes. In chapter 4 the KMC approach will be described in detail and its results will be compared with a similar simulation analysis carried out by means of the continuum model.

The previous research issues have been conducted from a fundamental point of view in non-patterned structures. However, for application purposes, due to the comparable dimensions of the nano-device periodic structure and the laser wave length, an accurate study of the feasibility of laser irradiation as a heat source for real patterned substrates is needed. This study reveals some crucial drawbacks when applied to conventional Si based devices. In this sense, laser irradiation brings the technology back to the beginning of microelectronics. Indeed, the application of this process seems more effective in the case of Ge and Ge-based devices.

Therefore a deeper analysis of the integration of laser annealing in SiGe and Ge-based MOS devices is needed. We developed a simulation code based on two modules: the former simulates the interaction between the laser light and the transistor structure in order to estimate the heat source. The latter simulates heat diffusion, phase changes and material redistribution under irradiation and it corresponds to the two-dimensional case of the approach described in the first chapter. The model is calibrated in the case of different atomic species (namely Si, Ge and common dopant impurities), considering the thermal properties of the materials and the impurity-dependent diffusivity in the solid, liquid and interface region. In chapter 5, we present several simulation results obtained by varying materials, implanted impurity profiles and geometry of the Complementary Metal Oxide Semiconductor (CMOS)-like structures. With the support of the simulation results we discuss the possible perspectives of excimer laser annealing applications for the fabrication of post-Si CMOS devices [27].

1. Laser annealing of semiconductors: a general overview

1.1. Overview

The introduction and the subsequent investigation of laser irradiation in order to modify material properties has a parallel origin to the laser development. At the beginning of the 50's and the 60's, several research groups started to investigate the feasibility to produce coherent micro- and nanometer electromagnetic waves, both in pulsed and continuous emission. Early Maser (Microwave Amplification by Stimulated Emission of Radiation) equipments, exploiting Einstein theory on the stimulated light emission of excited systems, were based on the dis-excitation of a gas (ammonia) or solid state materials (chrome-ruby). Subsequently, the need to produce visible electromagnetic waves led to Laser (Light Amplification by Stimulated Emission of Radiation) devices. As maser systems, they were based on the dis-excitation of a gas system (helium-neon) or solid state materials (ruby, gallium arsenide).

The introduction of semiconductor-based laser allowed researchers to use stimulated light in continuous emission. In order to improve the device performances and their application, the effects of laser irradiation on the irradiated materials started to stimulate the interest of several scientists. From this point to the present days, important results have been achieved. Due to the intrinsic features of the laser annealing processes (evolution of bulk and surface material properties on a scale less than micro and nanosecond), an intensive use of computer simulation supported the whole investigation journey. Concerning the chapter content, after a brief historical survey, we will deal with some interesting cases where material modifications are provoked by millisecond (continuous scanning) and nanosecond (pulsed) laser annealing. Starting from experimental observations, the investigation will be carried out mainly by means of simulations and the proper theoretical models will be presented.

1.2. Laser processing of semiconductors: historical survey

The history of the investigation of the physical properties of semiconductors starts at the beginning of the 60's with several groups of research in the Soviet Union and the USA [7, 8, 9, 65].

In this first phase, the optical properties and recombination in strongly excited silicon was experimentally studied. Blinov investigated an unusual behavior of reflectivity increase from the surface of a strongly excited semiconductor and suggested that it was due to the melting of a thin surface layer, which exhibits metal properties.

Laser annealing of implanted layer was investigated for the first time by the Philipovich group in 1974 [74]. In the same year, using a heavy dose Phosphorus implant annealed by laser, another research grop directed by Prof. Khaibullin (University of Kazan) studied the effects of laser annealing in implanted layers [43]. Examples of their data are shown in Figure 1.1.

In 1977, papers started to be submitted by Russian research groups on these issues. A. V. Dvurechensky of the Institute of Semiconductor Physics of Academy of Science of the USSR in Novosibirsk and his co-workers found that both millisecond and nanosecond laser pulses affect dopant distribution. Their works suggested that excess of vacancies or the regrowth of the molten region play a central role on the dopant redistribution at high power densities. Concurrently, Prof. I. B. Khaibullin's group (Kazan Physical Institute of Academy of Sciences of the USSR) investigated the reordering of damaged implanted

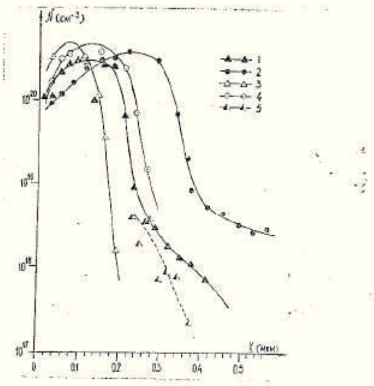

Рис.5. Профили распределения концентрации носителей заряда по глубине ИЛС на кремнии, полученных при лазерном (λ=1.06 мкм, $\tau_{имп}$=20 нсек, J_0=2.5·10^7 вт·см$^{-2}$) и термическом ($T_{отж}$=800°C, $t_{отж}$=30 мин) отжиге.

I – $Si \leftarrow P^+$, E=100 кэВ, Δ=6·10^{15} ион·см$^{-2}$, отжиг термич.
2 – $Si \leftarrow P^+$ 150, 3·10^{16}, отжиг термич.
3 – $Si \leftarrow P^+$ 100, 6·10^{15}, отжиг лазерный
4 – $Si \leftarrow P^+$ 150, 3·10^{16}, отжиг лазерный
5 – "хвост" профиля распределения $N(x)$ образца № 3, выявленный после дополнительного термического отжига.

Figure 1.1.: Dopant redistribution after laser annealing [43].

Si layers by means of laser pulse irradiation. These Russian pioneering works raised an incredible interest in the scientific community.

Bell Laboratories started to investigate laser annealing of an implanted layer, developing a thermal melting model of laser annealing of implanted layers in 1978. This model clarified many experimental results provoked by pulsed excitations. In 1979 the Naval Research Laboratory started to explore laser radiation effects on semiconductor materials.

J. Meyer, F. Bartoli, and other scientists in 1980 developed the theoretical formalism of laser beam interaction with semiconductors. The formalism was able to account for some previously unexplained trends in the InSb data, and was confident enough of its generality that it made sense to go ahead and apply it to other semiconductors and other wavelength regimes as well [58].

Richard Wood, C. W. White, R. T. Young, and G. Jellison, Jr. (Solid State Division of Oak Ridge National Laboratory) in the early 80's investigated laser effect on semiconductors. The measurement of the complex dielectric function of Si at elevated temperatures performed by Jellison was especially important in determining how laser radiation couples to the electronic and vibrational states of the system.

White from the Bell Labs as well as other research groups focused their attention on the application of pulse laser annealing. Stanford University focused primarily on the use of scanned CW laser for annealing of implanted layers. In 1979 Prof. J. Gibbons studied the application of scanning CW laser and electron beams in Si technology. The main point of his work may be summarized at the following:

- For thin amorphous layers of Si, the annealing process is a solid phase epitaxial regrowth
- No diffusion of implanted impurities occurs during annealing, irrespective of whether the amorphous layer is created by ion implantation
- The electrical activation can be $\sim 100\,\%$ even for the impurity concentrations that exceed the solid solubility limit.

Within 1978 and 1983, various works were published by Van Vechten based on an unconventional interpretation of laser annealing processes. He and his colleagues proposed a thermal component of laser annealing and presented a Plasma Annealing Model [99, and references therein].

New proposals appeared for light absorption on semiconductor materials, where electron-hole pair formation and excitation of free carriers play the main role.

Currently the investigation of laser annealing effects on semiconductor materials has made great strides on forward. We know more about the interaction of the light with the irradiated substrate. At the same time, the melting evolution during a laser annealing, the epitaxial regrowth process, the defect generation at the solid-liquid interface, and the dopant evolution in the molten regions have been deeply investigated both from an experimental and a theoretical point of view.

The laser community grew enormously in the past decades. The request of smaller and smaller microelectronic devices and the transition from micro to nano-sized structures, opened new possibility for laser processes.

New investigations regard: direct laser printing, laser assisted fabrication for sensors, laser processing in liquids, pulsed laser deposition of thin films, interface phenomena in thin film deposition, laser processing of polymers and bio-materials, ultrashort laser pulse interaction with materials, nano-scale processing by near field techniques, laser-based spectroscopy and plasma diagnostics, laser and photons for the synthesis, structuring and manipulation of new materials (nanotubes, clusters, thin films, and nanoparticles), 3D micro/nano-structuring for Micro Electro-Mechanical Systems (MEMS), Micro-Opto-Electro-Mechanical Systems (MOEMS), photonic crystals and photonic applications, multiphoton effects and materials processing. Therefore, today laser processes are used to modify both the material properties and the 3-D structure of the micro-devices.

Looking to the bulk properties modification of semiconductor substrate by laser irradiation, many phenomena are today still unclear. For instance, returning to the ever-green problem of laser irradiation of implanted silicon substrates, the activation mechanism of implanted dopant atoms under nanosecond laser annealing is poorly understood. At the same time, the anomalous behavior of some dopant atoms (As or B “pileup” at the melt depth region) in liquid phase during a laser annealing process is still a subject of investigation. A deep understanding of these issues due to the time and space nano-features of the processes can arise only by a strong interaction between experimental and theoretical analysis. Our work goes on this direction. Dopant-defect system evolution in implanted silicon under laser annealing both in liquid and solid phase will be widely discussed in the present thesis.

In the present chapter, a complete description of issues which arise when a laser irradiation process has to be simulated will be given. The simulation approaches for non-melting and melting annealing will be treated, focusing the attention on systems subjected to state of the art investigations.

1.3. The thermal problem for non-melting laser processes

Generally, when we deal with the simulation of a laser annealing process, we have to put the attention to different fundamental questions which characterize the simulation approach. These are the duration of the irradiation and the structure of the irradiated sample. The first point concerns the photon-material interaction at the atomic and sub-atomic scale, whilst the second is related to the interaction of the laser light with the irradiated structure at the laser wavelength scale. Both issues affect the light absorption on the irradiated sample and, as a consequence, the heat source determination. In the following we deal in detail with the problem of the heat source determination for a laser annealing process in non-melting conditions.

Laser heating is characterized by three important time scales : $\tau_e = C_e/\lambda$, the electron cooling time, $\tau_i = C_i/\lambda$, the lattice heating time, and τ_l, the duration of the laser pulse. Here C_e and C_i are the heat capacities of the electron and lattice subsystems, respectively, and λ a parameter characterizing the electron-lattice coupling in the target. Figure 1.2 shows the typical times for the scattering and recombination processes in silicon as a function of electron density (left hand scale). The distances of the thermal diffusion at room temperature and the melting point are also reported (right hand scale). Being the atom mass too large to interact with the high frequency photons, a laser light interacting with an absorber releases its energy by means of the (valence) electron and phonon systems. This energy can be re-irradiated or transformed in heat. The conversion occurs by means of electron-phonon interactions or Auger recombination. If τ_e is of the order of 1 ps and τ_l is of the order of ns or less (see blue and red line of Figure 1.2), the electron absorbed energy has enough time to be transferred to the lattice.

Consequently, the electrons and the lattice reach thermal equilibrium and heat conduction in the target can be described by means of Fourier's law, provided that the heat flux is constant over several mean free paths of the electrons that carry the heat. In these condi-

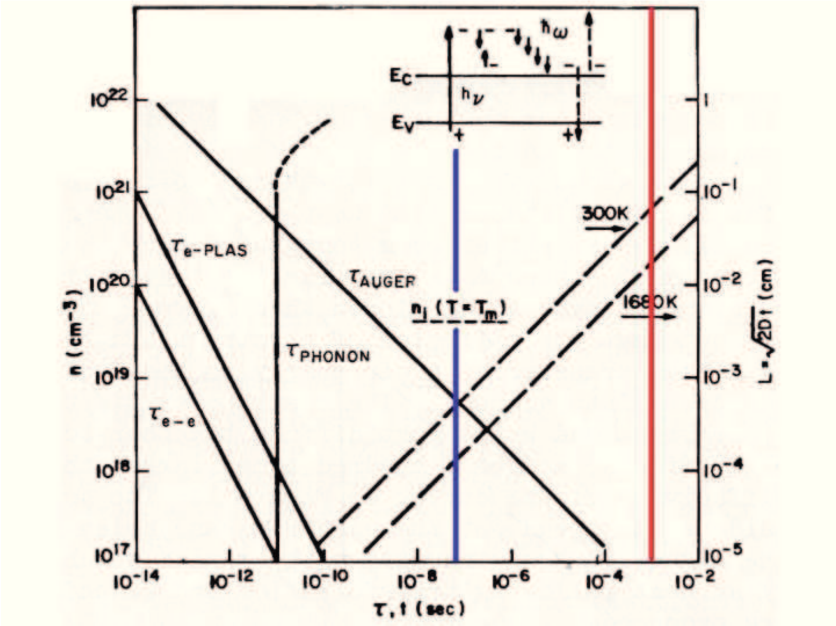

Figure 1.2.: Time for scattering and recombination processes in silicon as a function of electron density (left). Distances of thermal diffusion at room temperature and the melting point (right). As reference, the blue and red line indicate respectively, the typical time scale of an 180 ns excimer laser process and a millisecond continuous laser scanning.

tions, approximations can be done for the heat source. In turn, for irradiation pulses with duration less than one nanosecond, a model which considers explicitly the electron and lattice system has to be taken into account. The celebrated two-temperature model (TTM), developed by Anisimov *et al.* in 1974 [4], belongs to this model class.

The second point to be considered is the interaction of the laser light with the irradiated structure at the laser wavelength scale. The limiting case, where these interactions do not play any role in the irradiation, is that of a unique substrate with a thickness greater than its absorption length at the considered light frequency. In this case we can implement the source in the heat equation in a easy way by means of the following equation

$$S(t, z) = I(1 - R)\,\alpha e^{-\alpha z} \tag{1.1}$$

where I is the incident laser energy, R and α are the phase and temperature dependent surface reflectivity and the material absorption at the laser wavelength, respectively. In this form it gives the heat quantity absorbed by the irradiated sample at the time t and position z in depth. If our simulation is 2 or 3 dimensional, than the laser shape in the normal directions with respect to the laser beam has to be introduced by means of proper normalized functions. This kind of laser processes play a role only in the investigation of the direct or indirect effects of laser irradiation on particular materials.

Today laser processes involve very complex structures with a characteristic scale of the order of the laser wavelength. In particular we could refer to multilayer structures and patterned samples. In the first case a source like Equation 1.1 can be considered in the heat equation only if the component that rules the absorption in the bulk material (i.e. $(1 - R)\,\alpha e^{-\alpha z}$) becomes negligible in the first irradiated layer. If this condition it not verified we must consider multiple internal reflections that occur in such structures, based on the assumption that light combines coherently (or incoherently in the case of a disordered material) at each point in the layer under consideration. As a consequence the heat equation must be coupled with a proper code which calculates the real source, determining the optical absorption spectrum and optical absorption profile for any layer in the irradiated thin-film multilayer.

Concerning the laser irradiation of patterned structures, generally the problem lies on the interface where the interaction between the light and the periodic geometry of the integrated electronic devices has to be taken into account. In these conditions, a direct determination of the source starting from the numerical solution of the Maxwell equations is needed. They have to be solved in a box which mimics the real periodic structure.

In the following we will give the implementation details, presenting particular examples where the laser process simulations have supported the process design. This work has been carried forward in collaboration with experimental teams during the Ph. D. activity. In this research, the support of the experimental analysis with computer simulation of the annealing process has been fundamental both in predicting the melting phenomenon and the temperature evolution with the aim to determine convenient process windows and, in general, bulk effects of the laser light. In particular, focusing on the heat problem and the simulation details, the case of the crystallization of implanted amorphous silicon during millisecond annealing by infrared laser irradiation will be described [57]. Moreover, irradiation effects on multi-layer structures with the related issues and solutions will be also discussed. Concerning laser irradiation of patterned structures in the melting regime, we remand the reader to the chapter 5, which deals in detail with the problem in 2 dimensions.

1.3.1. Cristallization of amorphus silicon by scanning millisecond laser annealing

One of the main advantages of amorphous Si (a-Si) compared to crystalline Si (c-Si) is its production technique, as a-Si can be easily deposited at very low cost. This advantage is paid in terms of worse electronic properties which are not sufficiently good in order to satisfy the increased performance requirements of fast electronic device. However, starting from a low cost a-Si substrate, polycrystalline silicon layer can be generated by means of solid phase epitaxy SPE [67], spontaneous crystallization [89], or excimer laser annealing [28]. Most of the studies concerning crystal grain nucleation and growth are based on the Avrami–Johnson–Mehl description under the hypothesis that the nucleation rate, abruptly approaches a constant steady state value after a given incubation time. The characteristic crystallization time, depends on the steady-state nucleation rate and grain growth velocity, and it is about 20 s at 780 °C. Higher temperature cannot be easily investigated, by rapid thermal annealing, because the nucleation rate and the growth velocity are so high that the sample is

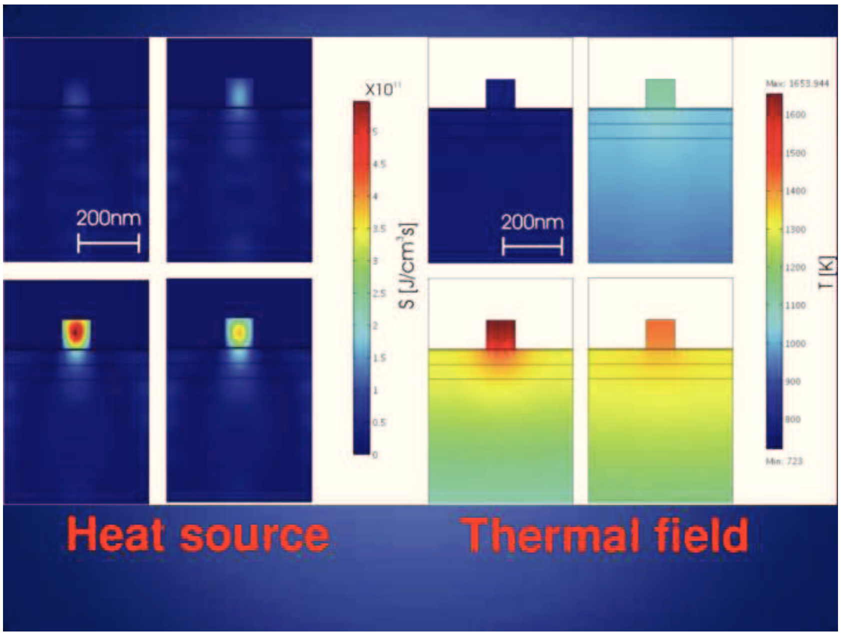

Figure 1.3.: Snapshots of the heat source (left side panels) and temperature (right side panels) during a 2 dimensional laser irradiation simulation of a real device structure.

crystalline already during the heating up. Hence, it arises the need of smaller annealing time scale.

In the work [57], Mannino *et al.* extended the description of the spontaneous crystallization up to 1323 K, i.e. 250 K above the temperature investigated by conventional annealing. In particular, we described the time evolution of the crystallized fraction during the infrared (IR) laser irradiation process of amorphous Si. A CW GaAs solid-state laser emitting at the wavelength of 808nm in the scanning configuration was used. The experimental equipment, by means of a fine tuning of the laser fluence and the scanning velocity, allows us to set the overall thermal budget supplied to the irradiated substrate. In order to reliably simulate the process, we have solved the time evolution of the nucleation rate following the theoretical model proposed by Kelton *et al.* [42], based on the numerical solution of the system of coupled differential equations governing the time dependence of the Si cluster concentration. After a check and a calibration of the model for several conventional thermal processes given in ref. [89], we have coupled the nucleation model with the time-dependent thermal field solver developed by our theoretical group for the particular laser process considered. We have calculated the temperature profile induced by laser irradiation simulating the thermal field $T(\boldsymbol{r},t)$ evolution during the laser scanning process. The heat equation

$$\rho c_p \frac{\partial T(\mathbf{r},t)}{\partial t} = \nabla \cdot [K\, \nabla T(\mathbf{r},t)] + S(\mathbf{r},t) \tag{1.2}$$

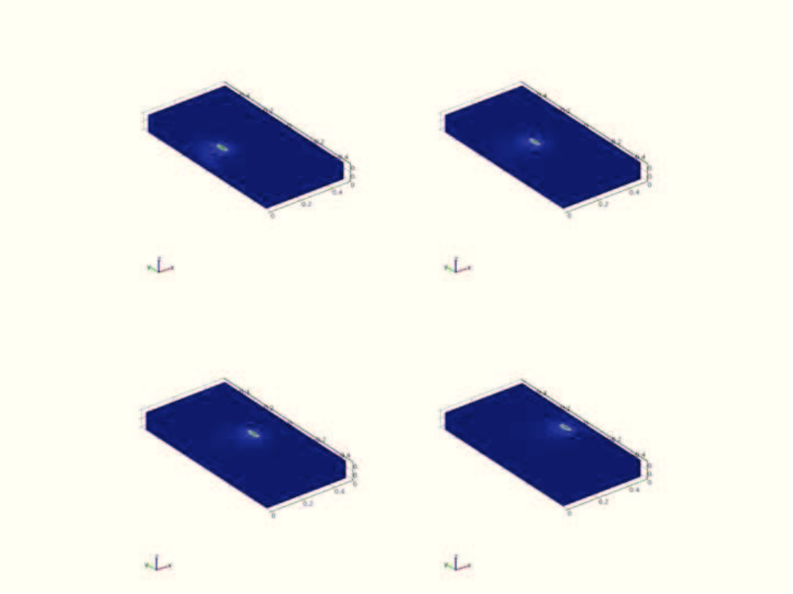

Figure 1.4.: Snapshot sequence taken from the numerical simulation of heat diffusion equation, corresponding to four different times belonging to the same process of continuous laser scanning. The simulation refers to a laser scan with a velocity $v = 7$ cm/s and a power equal to $P = 114.45$ W.

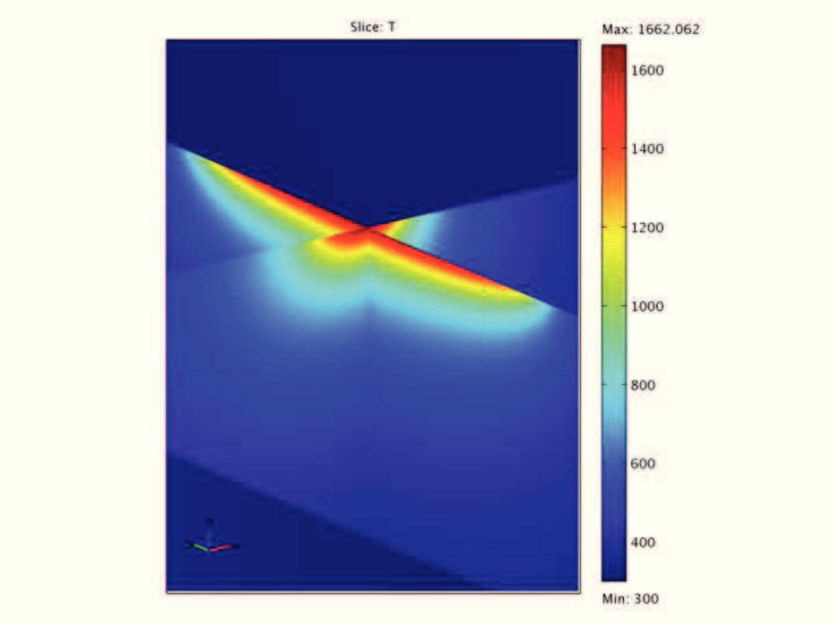

Figure 1.5.: Temperature field in the two perpendicular planes to the surface (xz and yx) of the crystal, which both pass through the spot center. The temperature is given in a color scale. The simulation refers to a laser scan with a velocity $v = 7$ cm/s and a power equal to $P = 114.45$ W.

has been solved in a three-dimensional computational box simulating the sample with the proper temperature and space dependent thermal and optical properties [53]. We would like to stress that in Equation 1.2 the material density ρ, the heat capacity at constant pressure c_p and the thermal conductivity K are temperature dependent. The implemented values are listed on Table C.1 of Appendix C. The irradiation has been considered by means of a volume heat source, reproducing the spot characteristics in terms of power and space distribution, thus mimicking the relative motion between spot and sample.

We have implemented the present and future PDE based continuum models and determined the corresponding numerical solutions in different conditions using the finite element COMSOL solver of differential equations (Appendix A). Here, the main simulation difficulty (common with other irradiation processes discussed in this thesis) is related to the implicit dependence of the source on T. Indeed, apart from the usual variations with time and space, the heat source depends also self-consistently on the thermal field itself due to the dependence of the optical properties on T. As an example, we can observe in Figure 1.3 how the heat source changes during a laser irradiation process for a 2 dimensional simulation case. The four graphs are snapshots of the heat source (left side panels) and temperature (right side panels) during the laser irradiation of a real device structure. In this case near field solutions of the Maxwell equations are necessary to quantitatively determine the heat source.

In the case of the crystallization experiment we can apply the simulation setting for the continuous wave irradiation of plane samples which are homogeneous in depth in the light absorption region. Therefore, if we choose x as the scan direction and z the laser beam direction,

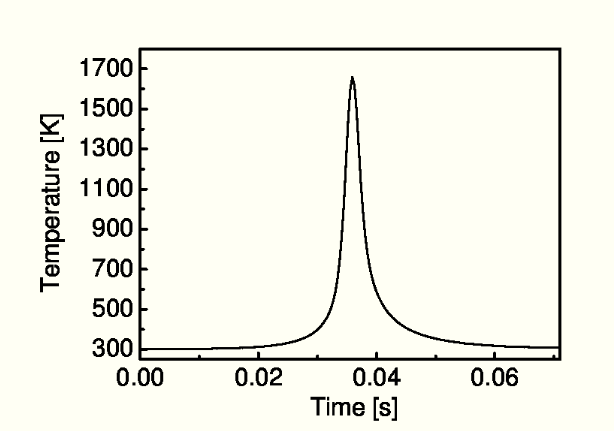

Figure 1.6.: Thermal field associated to a laser process with a scanning speed $v = 7$ cm/s and a power of $P = 114.5$ W. The plot shown is the temperature variation seen by a generic point on the surface as a function of time.

then the source term $S\left(x,t\right)$ can be written as following:

$$S\left(x,t\right)=\Phi\left(z\right)\cdot F\left(x,y,t\right), \tag{1.3}$$

where $\Phi\left(z\right)$is the absorbed power density in the z direction, approximated with the functional relation of Equation 1.1 where reflectivity and absorption length are T dependent expressions, and $F\left(x,y,t\right)$ is a normalized function which describes the laser shape on the orthogonal plane to the z direction of laser propagation. The experimental equipment allow to visualize and extract the x and y spatial distribution of the laser intensity. In our case, $F\left(x,y,t\right)=G\left(x,t\right)\cdot R\left(y\right)$ where $G\left(x,t\right)$ and $R\left(y\right)$ are, respectively, a gaussian and rectangular function.

Figure 1.4 shows the snapshot sequence taken from the numerical simulation of heat diffusion equation, corresponding to four different times belonging to the same process of continuous laser scanning on a crystalline silicon substrate. The simulation refers to a laser scan with a velocity $v=7$ cm/s and a power equal to $P=114.45$ W. Referring to the same laser process, Figure 1.5 and Figure 1.6 show, respectively, the space and temporal distributions of the temperature taken at the laser spot center (in a generic point on the surface during the constant velocity laser scan).

In the amorphous silicon case, the peak temperature estimated in one of the central points along the scanning direction [Figure 1.7(a)] is of 1323 K. Note that apart from two regions at the borders of the annealed samples the temperature pulse is similar for all these points.

The results of Figure 1.7(b) have been obtained solving the coupling models for thermal field and nucleation evolution. Nucleation rate (full line) is significantly different from zero only after 12.5 ms when temperature reaches its maximum value (1323 K), then rapidly increases to a peak value of 3.5×10^{17} cm^{-3} s^{-1}, and finally decreases to zero in a time interval as short as 7 ms. In the meanwhile, the crystalline volume fraction χ_c [dashed line in Figure 1.7(b)] monotonically increases approaching the final value χ_c= 0.83 and then keeps

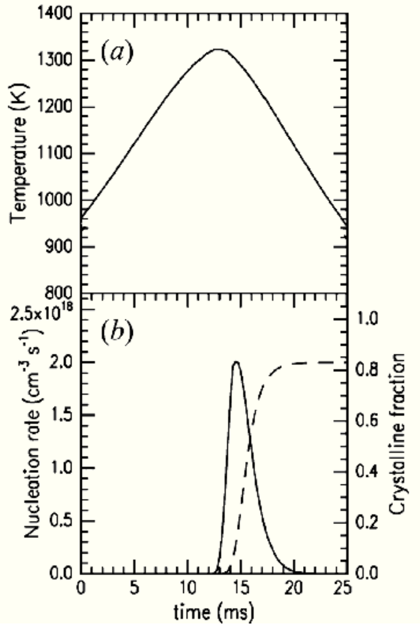

Figure 1.7.: (a) Temperature profile reached by *a*-Si in the middle of the laser scan by thermal field evolution simulation, and (b) nucleation rate of crystalline grains in *a*-Si (full line) and crystalline volume fraction (dashed line) during the temperature profile in (a).

constant because grain growth velocity strongly reduces decreasing the temperature.

The results have demonstrated that a general model, not necessarily based on the assumption of a steady state, can be used to draw a consistent scenario of *a*-c phase transition occurring up to temperatures as high as 1323 K, i.e. about 250 K higher than that reachable by conventional annealing, for few milliseconds. This investigation has been made accessible thanks to the use of process simulation: the knowledge of the transient variation of the temperature during the laser irradiation, namely during the crystallization process has been fundamental in order to predict the correct nucleation rate. On the other hand, due to the time and space dependence of the heat source, the access to this bulk thermal properties during the millisecond annealing process is only possible by means of the simulations, making them fundamental for the analysis and the investigation of the laser effects on the material modifications.

1.3.2. Irradiation of multi-layer structures

Electronic devices based on thin-film multi-layer structures have received a great interest in the last years. They find application in many areas as solar cells, data storage, light emission, light trapping devices and involve various materials like metals, semiconductors, oxide, chalcogenides or organics. Laser irradiation of these multi-layered structures can be used as a heat source achieving high process temperature in a short annealing time, which goes from millisecond (continuous scanning configuration) to nanosecond (pulsed laser irradiation). Generally the knowledge of the temperature as a time and space function during the heating process as well as the determination of the process window for melting, partial melting or no-melting irradiation is vital. All these requests can be supplied by means of a simulation support as seen in the previous paragraph.

On the other hand, multi-layer structures introduce new difficulties on the heat source estimation. In fact, multi-layer systems are usually composed by few nanometers thick films, i.e. critical dimensions of the order of the wave length of the used laser equipment. Therefore, simplified implementations of laser source on the heat equation which do not consider coherent (or incoherent) interference between light waves in the structure are totally wrong. Heat equation has to be coupled with a proper code which can calculate the real source, determining the optical absorption spectrum and optical absorption profile for any layer in the irradiated thin-film multilayer structure.

In order to achieve this goal, we have developed a one-dimensional model which takes into account the multiple internal reflections that occur in such structures, based on the assumption that light combines coherently at each point of the layer under consideration. Without entering in the implementation details [76], considering an incident

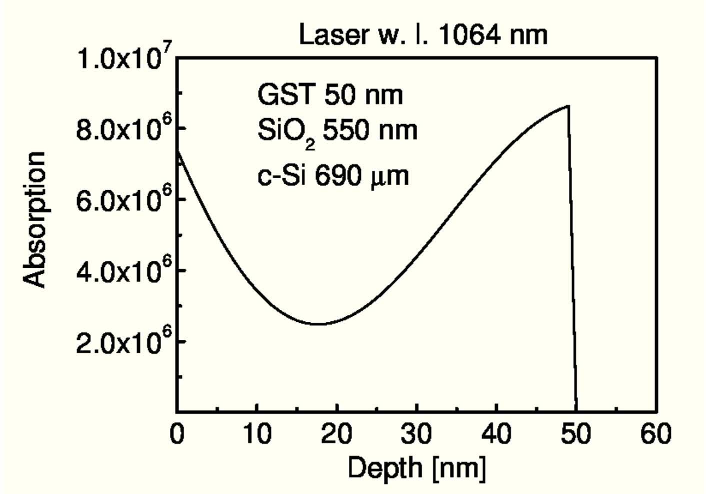

Figure 1.8.: Absorption profile on the GST layer obtained with the matrix method for a wave length of 1064 nm (multilayer composed by: 50 nm GST, 550 nm SiO_2, 690 μm c-Si).

wave monochromatic and incident normal to the front layer, the code calculates the reflected, transmitted and absorbed fractions of the electromagnetic radiation intensity. Furthermore, the absorption profile on each single layer is determined as a function of the depth orthogonal to the multilayer system. The data needed for the calculations are the complex index of refraction and the dimension of each layer of the system. The model is based on the solutions, derived by means of the matrix method, of the equations relating the four electromagnetic field amplitudes on either side of an interface.

As an example, we consider a multi-layer substrate formed by 50 nm of GST, 550 nm of SiO_2 and 690 μm of c-Si. We have calibrated the code with the known refractive index dependence of the different substances on the laser frequency. Considering that we irradiate the sample with a pulsed 12ns Nd:YAG monochromatic laser having a wave length of 1064 nm, the absorption profile can be calculated. Results suggest that only the GST layer absorbs the light, being the c-Si substrate almost transparent for the photon energy here considered (E_{1064}=

1.16 eV). Figure 1.8 shows the results for the first 60 nm from the irradiated surface. As we can see, the coherent interference between light waves in the structure produces an absorption profile totally different from the simple exponential one

$$A(x) = \alpha \exp(-\alpha \cdot x) \tag{1.4}$$

adopted for irradiation of single substrate with a thickness greater than the light absorption length. For the wave length of 1064 nm, the inverse of the absorption coefficient of GST is $1/a_{\mathrm{GST}}$= 38 nm [46].

1.4. The melting problem

In the investigations of the material modifications due to the laser irradiation of a processed substrate it is fundamental to know the temperature distribution as well as the melting and solidification details in the annealed regions. Since all these quantities are difficult to measure directly, a theoretical analysis of the problem by means of process simulations is a key point for the process control. In the last section we treated a laser irradiation process in a non-melting regime. Many experimental investigations lie on these conditions where material modifications due to laser irradiation play a role only in the solid phase and phase transitions do not occur.

However, interesting phenomena appear when the heat due to the irradiation melts the processed sample. Heat transfer in laser-induced melting and solidification is a transient, non-linear phenomenon with a moving solid/liquid interface corresponding to the release or absorption of latent heat during phase change. In order to deal with phase change problems, many numerical methods such as front tracking methods and fixed domain methods have been and are still being developed. The main advantage of fixed domain methods [78] is that no explicit tracking of the phase front is needed. A number of fixed grid methods have been proposed including effective specific heat methods [36], enthalpy methods [20, 44], source term methods

[101] and phase field models [41, 104]. In the following, we will deal with the laser melting problem from the simulation point of view, giving a description of the most common methods used. Firstly, a front tracking model for the resolution of the Stefan problem will be presented. Afterwards, we will give details of two fixed domain methods, i.e. the enthalpy and the phase field methods. The latter two can be implemented in order to solve the thermal problem for laser irradiated substrates.

1.4.1. Front tracking model

Many relevant heat conduction or diffusion problems involve phase transformations. A common example of such a problem is the ice-melting one that was firstly treated by Stefan [90]. Thereon, these kind of problems are widely referred to as Stefan problems. During melting or solidification, the moving boundary (interface) separating the liquid and the solid phases of the material changes with time. In both sides of this interface, the classical heat equation is satisfied. On the solid/liquid interface, the released or absorbed latent heat is balanced with the heat fluxes from both phases.

In order to give an idea of how the front tracking model deals with Stefan problems, in the following we present a particular model for the case of melting evolution, i.e. solid liquid phase transformation. It is important to note that front tracking methods consider explicitly the solid-liquid interface as a variable of the problem to be determined.

Let us consider a fixed domain $[0,\ l]$, where we have a material that is in its liquid state in a certain region $[0,\ s(t)]$ and in its solid state in the rest of the domain. The point separating the liquid and the solid phases determines the position of the interface $s(t)$. We denote the temperature in the point x at time t by $u(x,\ t)$. The governing equations for this problem are the heat equations in both the liquid and the solid phases

$$\frac{\partial u}{\partial t}(x,t) = \frac{\partial}{\partial x}\left(K_{\text{liq}}\frac{\partial u}{\partial x}\right), \quad x \in \Omega_{\text{liq}} \tag{1.5}$$

$$\frac{\partial u}{\partial t}(x,t) = \frac{\partial}{\partial x}\left(K_{\mathrm{sol}}\frac{\partial u}{\partial x}\right), \quad x \in \Omega_{\mathrm{sol}}, \tag{1.6}$$

where K_{sol} and K_{liq} denote the thermal diffusivities in the solid and the liquid phase respectively, which involve the heat capacity, density and the heat conduction coefficient of the materials. The velocity v of the interface is given by the jump condition

$$Lv = K_{\mathrm{sol}}\frac{\partial u}{\partial x}(x,t)\mid_{x\downarrow s(t)} - K_{\mathrm{liq}}\frac{\partial u}{\partial x}(x,t)\mid_{x\uparrow s(t)}, \tag{1.7}$$

where L denotes the latent heat of solidification. This last equation is frequently called the Stefan condition. At the interface we have the melting temperature. Generally here it is chosen to be zero without loss of generality: $u(s(t\ ),\ t) = 0$. If the position of the interface s is a differentiable function, the velocity of the interface v can be replaced by

$$L\frac{\partial s}{\partial t}(t) = K_{\mathrm{sol}}\frac{\partial u}{\partial x}(x,t)\mid_{x\downarrow s(t)} - K_{\mathrm{liq}}\frac{\partial u}{\partial x}(x,t)\mid_{x\uparrow s(t)}. \tag{1.8}$$

Subsequently boundary and initial conditions have to be fixed in order to have a unique solution.

1.4.2. Enthalpy model

Implicit or fixed domain methods are the natural alternative to front tracking methods. Within them the most used are the enthalpy method, the level set method and the phase field method. In the enthalpy method (ref. [18]) the enthalpy function is introduced. This function measures the total heat of the system, and it has a jump discontinuity at the interface given by the heat released (or absorbed) during the phase change. This discontinuity is helpful to determine the interface position. In the following we will present an enthalpy formulation for the heating-melting problem in the case of laser irradiation.

Heat conduction and phase changes in the target are ruled by the energy conservation law in terms of the (volumetric) enthalpy H

$$\partial_t H + \nabla \cdot \vec{Q} = S \,. \tag{1.9}$$

where $\vec{Q}$ is the heat flux and S a possible heat source.

The energy conservation law directly updates the enthalpy H (per unit volume) to new times, from which we need to find the new phase, temperature and phase fractions. Therefore, in order to determine the temperature evolution, it has to be coupled with an appropriate equation for T. The Equations of State $H = H(T, P, phase)$, consistent with the thermo-chemistry of the material, can support our request:

$$dH^i = {C_p}^i dT + [-\alpha^i T + 1]dP \quad i = S, L, \tag{1.10}$$

where C_p^i and α^i are the heat capacity (per unit volume) and thermal expansion coefficient of phase i, respectively. The enthalpy within each phase (Solid, Liquid) can be expressed in terms of the pair (T, P) by integration along constant T and constant P paths on the (T, P)-phase diagram relative to a *consistent* reference state. Integration of Equation 1.10 for constant P paths can be coupled with Equation 1.9 for H evolution.

H denotes volumetric enthalpy (per unit of volume), lower case h denotes specific enthalpy (per unit of mass). Clearly, $H = \rho h$ in each phase. The value h_{ref} (and thus also $H_{\mathrm{ref}} = \rho^S h_{\mathrm{ref}}$) of the enthalpy at the reference state can be arbitrary. Since the heat capacity is strictly positive and ΔH^{fus} and ΔH^{vap} are also positive (by our choice of h_{ref}), the dependence of H on T is monotonic. Thus T can be found from H.

1.4.3. Phase field methodology

The *phase field* approach has its roots in statistical physics. In particular, a new thermodynamic variable is introduced, the phase field *φ(x,t),* which is associated with the phase of the system as a function of the time and space and varies smoothly from one value in the liquid to another value in the solid across a spatially diffusive interface region of thickness *W*. The advantages of applying the phase-field methodology on phase transition problems are twofold: a) it provides a simple, elegant description that appears to embody a rich variety of realistic physical growth phenomena; b) from a computational point of view, it is in principle simple to obtain solutions since it is not necessary to distinguish between the different phases. These issues are important when solid or liquid regions change with time.

As for all the other thermodynamic variables, the Helmholtz free energy $\mathcal{F}(\varphi, ...)$ is also a functional of the phase field and its gradient is in the following form:

$$\mathcal{F}(\varphi, ...) = \int_{\Omega} \left[f(\varphi, ...) + \frac{1}{2}\epsilon^2 (\nabla\varphi)^2 + ... \right] d\Omega, \tag{1.11}$$

where Ω is the system domain, *f(φ,...)* the Helmholtz free energy density for a phase with no gradients (usually a “double-well” function of *φ* is chosen). The problem presented can be then formulated in terms of partial differential equations. The phase field is then assumed to evolve as

$$\dot{\varphi} \propto \mathcal{L}\left(\frac{\delta\mathcal{F}}{\delta\varphi}\right), \tag{1.12}$$

where $\mathcal{L}$ is some partial differential operator satisfying $\mathcal{L}(0)=0$. This equation is then supplemented by partial differential equations for the other thermodynamic variables. We adopt the following phenomenological free energy

$$\mathcal{F} = \int_{\Omega} \left[f(\varphi) + \frac{[W(\mathbf{n})]^2}{2} \mid \vec{\nabla}\varphi \mid^2 + b\lambda\frac{u^2}{2} \right] d\Omega, \tag{1.13}$$

where W is the interface thickness and $\mathbf{n}$ the normal direction to the interface

$$\mathbf{n} = \frac{\vec{\nabla}\varphi}{\mid \vec{\nabla}\varphi \mid}. \tag{1.14}$$

λ is a dimensionless parameter that controls the strength of the coupling between the phase and diffusion fields (typically of order unity), b a constant and u denotes the dimensionless temperature field

$$u = \frac{c_p \cdot (T - T_M)}{L}. \tag{1.15}$$

Here T_M is the melting temperature, L the latent heat of melting and c_p the specific heat at constant pressure. Applying a single Lyapounov functional (expressed in the variational form), the basic equations of the phase-field model can be obtained:

$$\tau(\mathbf{n}) \frac{\partial \varphi}{\partial t} = -\frac{\delta \mathcal{F}}{\delta \varphi} \tag{1.16}$$

$$\frac{\partial U}{\partial t} = \frac{D}{b\lambda} \nabla^2 \frac{\delta \mathcal{F}}{\delta U}, \tag{1.17}$$

for the independent variables phase field φ and the dimensionless enthalpy U defined by

$$U = u - \frac{h(\varphi)}{2}. \tag{1.18}$$

In the last equations, τ is the characteristic time of attachment of atoms at the interface ($\sim 10^{-13}$ s for metallic systems), D the thermal diffusivity and *h(φ)* is a function that describes the generation of latent heat. Equation 1.16 and Equation 1.17 imply that

$$\frac{\mathrm{d}\mathcal{F}}{\mathrm{d}t} \leq 0, \tag{1.19}$$

if there are no fluxes across the boundaries of the volume where $\mathcal{F}$ is defined, i.e., the dynamics drives the system towards a minimum of free energy. To obtain a phase-field model that reduces to the desired free-boundary problem, it is generally sufficient to require that *f(φ)* has the shape of a double-well potential. The simplest choice for *f(φ)* that has been traditionally used is

$$f\left(\varphi\right) = -\frac{\varphi^2}{2} + \frac{\varphi^4}{4}. \tag{1.20}$$

This last function has two local minima at $\varphi = \pm 1$, which correspond to the solid phase ($\varphi = +1$) and the liquid one (φ = -1). In order to ensure that a unit amount of latent heat is produced at the interface with the temperature field normalized by L / c_p and for *f(φ)* defined before, *h(φ)* has to satisfy the additional condition

$$\frac{h\left(+1\right) - h\left(-1\right)}{2} = 1. \tag{1.21}$$

Choosing *g(φ)* and *h(φ)* in a way that they satisfy the condition

$$g\left(\varphi\right) = \frac{b}{2} h\left(\varphi\right), \tag{1.22}$$

Equation 1.16 and Equation 1.17 reduce to the form

$$\tau \frac{\partial \varphi}{\partial t} = W^2 \nabla^2 \varphi - \frac{\partial F\left(\varphi, \lambda u\right)}{\partial \varphi} \tag{1.23}$$

$$\frac{\partial u}{\partial t} = D\nabla^2 u + \frac{1}{2} \cdot \frac{\partial h(\varphi)}{\partial t}, \tag{1.24}$$

where $F(\varphi, \lambda u) = f(\varphi) + \lambda g(\varphi) u$ is a function that has the form of a double-well potential where the relative height of the two minima is temperature dependent. However, it is important to stress that the constraint imposed by Equation 1.22 is not necessary to obtain phase-field equations that reduce to the desired free-boundary problem in the limit of a thin interface.

The following functional forms have been adopted for *g(φ)* and *h(φ)*:

$$g(\varphi) = \varphi - \frac{2\varphi^3}{3} + \frac{\varphi^5}{5} \tag{1.25}$$

$$h(\varphi) = \frac{15}{8}\left(\varphi - \frac{2\varphi^3}{3} + \frac{\varphi^5}{5}\right), \tag{1.26}$$

which satisfy Equation 1.22 with $b = 16/15$. Putting all the defined functions on Equation 1.16 and Equation 1.17 (or Equation 1.23 and Equation 1.24), we obtain the final phase field for the independent variables φ and T

$$\tau\frac{\partial \varphi}{\partial t} = W^2\nabla^2\varphi - \varphi\left(\varphi^2 - 1\right) - \lambda\frac{c_p}{L_{fus}}\left(T - T_M\right)\left(\varphi^2 - 1\right)^2 \tag{1.27}$$

$$\rho c_p\frac{\partial T}{\partial t} - \nabla^2(KT) = \frac{\rho L_{fus}}{2}\frac{15}{8}\left(\varphi^2 - 1\right)\frac{\partial \varphi}{\partial t} + S(x,t). \tag{1.28}$$

where L_{fus} is the latent heat of the crystalline substrate, respectively. The laser source term S, at time t and position z, is given by

$$S(t,z) = E_{las}P(t)(1-R)\,\alpha e^{-\alpha z}, \tag{1.29}$$

where E_{las} is the incident laser energy, $P(t)$ is the normalized laser pulse shape, and R and α are the phase and temperature dependent surface reflectivity and the material absorption at the laser wavelength, respectively.

Since the melt thickness is very small, convective effects do not arise in the melt. Thus the heat flux in the solid and liquid is due to heat conduction only, $\vec{Q} = -k\nabla T$, with k = thermal conductivity, T = temperature. On the contrary, the presence of strong advection in the plume domain requires solution of the continuity and momentum equations as well.

All the material properties (heat capacity c_p, heat conductivity K, and density ρ) are phase and temperature dependent. The phase field parameters (τ, W, and λ) are chosen in order to correctly achieve the thin interface limit [41]. The phase field model calibration of parameters used in this work is equivalent to that reported in Ref. [49].

1.5. The challenge to activate implanted dopant atoms by laser annealing

Laser Thermal Annealing (LTA) receives a great interest in the formation of ultrashallow junctions essential in nanoscale metal-oxide-semiconductor technology [2, 35, 70, and references therein]. A sequence of ion implantation and thermal processing is commonly used to modify the electronic properties of semiconductors, in particular to create a space dependent work function in the material. Samples can be processed with laser irradiation for two reasons (sometimes concurrent): a) melt the near surface irradiated regions causing a re-distribution of the dopant atoms, an annihilation of the implant damage in the molten regions and a crystal regrowth; b) recovering implantation damage, activating and redistributing by diffusion the doping impurities in the solid phase.

As an example, we would like to report two experimental investigations which consider dopant evolution in crystalline silicon substrate.

Following the organization of the present chapter, first the evolution of a dopant B-delta layers under a millisecond laser annealing in a scanning configuration is described. Subsequently we will deal with dopant evolution in a double implanted silicon sample under pulsed nanosecond laser irradiation, where melting and non-melting conditions occur.

1.5.1. Dopant evolution in the millisecond scale

The non-equilibrium kinetics of a coupled system of point defects and impurities in Si has attracted a broad interest in the last decades. The past interest essentially focused in the non-equilibrium caused by a point defect excess and in the role played by this excess in the transient enhanced diffusion (TED) phenomena in Si. As a consequence, being the defect super-saturation the only relevant driving force of the non-equilibrium kinetics, the different stages (diffusion, aggregate nucleation, formation and annihilation of extended defects) of the defect evolution in Si at quasi-constant temperature are now well known. Moreover, a consistent modeling approach has been derived and validated by experimental works [30, 71, 91]. The current trend of the dopant activation process in Si is characterized by an extreme reduction of the annealing time (from the ms to ns regime for the ultra-fast thermal processes) and a correspondent increase of the peak temperature, eventually using the laser irradiation (LI) as a heat source [49, 50, 70, 105]. These processes should complement or substitute the actual rapid thermal annealing in the activation module of future nanoelectronics devices.

However, the post-implant kinetics of the defects–dopant system in the extremely far-from-the equilibrium conditions caused by the laser irradiation both in the non-melting and melting regime is almost totally unknown. From the theoretical point of view some relevant questions have to be addressed: the formalization of a reliable kinetic formalism for the evolving defect-impurity system in a non-uniform fast-varying thermal field, the generalization of the kinetic parameters (e.g. diffusivity, clustering rate constants, etc.) in this regime, the inclusion in the formalism of eventual phase transitions [49], the interaction between the defects generated by the implant and the defects generated by the process [52].

In order to clarify all these issues, different experimental and theoretical studies have been carried out. In particular, we have investigated dopant-defect system evolution on the millisecon scale [53].

The experiments have been performed on silicon samples containing chemical vapor deposition grown B-delta layers. The samples were implanted with Si ions to a dose of 5×10^{13} atoms/cm^2 at an energy of 40 keV. Subsequent laser irradiations were performed using the GaAs solid-state laser which emitted a continuous radiation at the wavelength of 808 nm in the scanning configuration (same laser of subsection 1.3.1). Different annealing conditions have been investigated varying the velocity and the power of the laser beam. Experimental chemical profile before and after irradiation was performed by means of Secondary Ion Mass Spectroscopy (SIMS, see Appendix B for details).

Our investigation is focused on the effect of the Si interstitial supersaturation due to the Si ions implant on the substitutional dopant atoms of the B-delta layers. We arrange this particular experiment instead of a common dopant implant, in order to decouple Si interstitials with respect to the dopant atoms, preventing the formation of immobile dopant aggregates. In order to better understand the role of the silicon interstitial supersaturation on the dopant evolution, a substrate containing a B-delta layer has been annealed without a Si ion implant.

Solving the heat equation (simulation details are given in subsection 1.3.1), the temperature evolution in the whole irradiated substrate can be determined. Figure 1.4, Figure 1.5 and Figure 1.6 refer to the thermal problem of the laser annealing process here discussed. Concurrently a proper model for the dopant-defect system has been implemented. It is derived from the kinetic Boltzmann's formalism. The model will be described accurately in subsection 2.4.2 and subsection 3.3.3.

One of the results of our investigation is reported in Figure 1.9, where we compare the experimental (blue line) and simulated chemical boron profiles after an irradiation process carried out with laser scanning

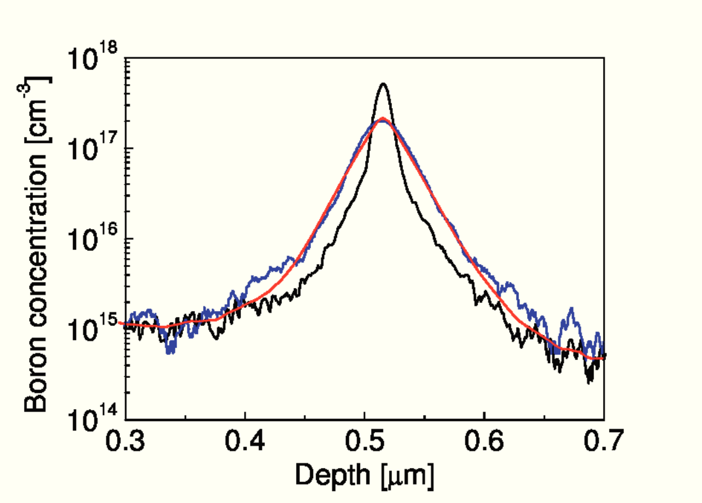

Figure 1.9.: Comparing the experimental (blue line) and simulated chemical boron profiles after an irradiation process carried out with laser scanning speed v = 7 cm/s and power P = 114.45 W. Th dark line refers to the as-grown B-delta layer.

speed v = 7 cm/s and power P = 114.45 W. The dark line refers to the as-grown B-delta layer. The temperature distribution associated to this laser process seen by a generic point on the surface as a function of time is shown in Figure 1.6. An almost perfect agreement can be found between the experimental and simulated data. On the other hand, samples annealed without the Si implant do not show any substantial dopant diffusion. These results allow us to conclude that the defect system rules dopant evolution also at the millisecond scale. An application of the kinetic theory to the analysis of scanning laser processes seems to indicate that the relaxation time of the energy is much smaller than the thermal pulses (lasting fewtens of millisecond). Therefore, a unique local temperature can be used in the case of such thermal process. A noteworthy result of the analysis presented here is the confirmation of the reliability, in the case the laser scanning processes, of the energetic calibration for the I-type defects [30, 71, 91], derived with the aid of experiments based on standard thermal annealing. This fact indicates that the energetic related to the stability of the complexes is (as we should expect) an intrinsic property of the system.

Millisecond laser irradiation causes non-equilibrium dopant diffusion. The scenario is totally different in the nanosecond scale, where dopant diffusion does not take place even for the high defect supersaturation here considered. Therefore dopant activation remains the unique physical observable quantity (i.e. a quantity showing a kinetic trend) which allows a possible investigation of damage evolution in the submicrosecond regime.

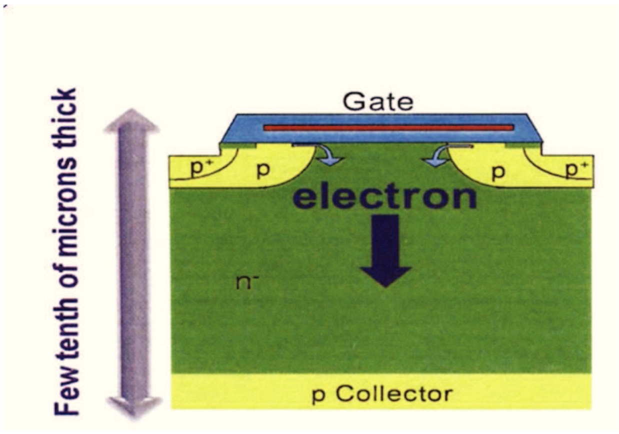

Figure 1.10.: Current IGBT Structure. Electrons move from the device top side to the collector.

1.5.2. Melting and non-melting dopant evolution for pulsed nanosecond irradiation

In order to report a real case where LTA can help the development of ultrashallow junctions, we would like to present in this sub-section a possible technological application. Power devices and particularly Insulated Gate Bipolar Transistors (IGBT) are today a major part of the semiconductor market breakdown with a large range of device types in both consumer and industrial applications. Basically, IGBTs work as

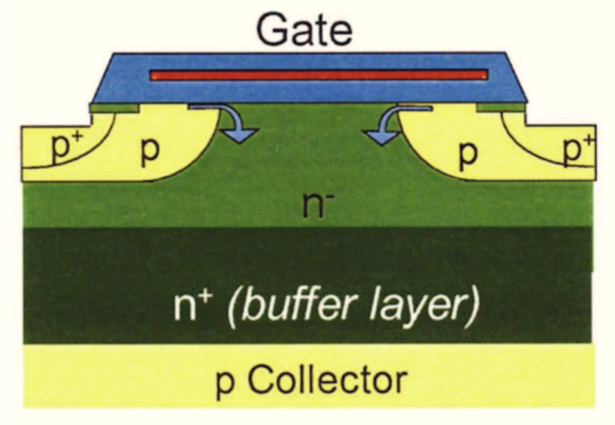

Figure 1.11.: New IGBT structure. The buffer layer is located right after the collector to prevent it from being damaged with a high electrical field.

power switches with frequencies up to few 100 of kilohertz. They are built along the vertical dimension of the wafer with a typical thickness of IGBTs in production today around 40 μm. The front side of the IGBT is composed by a Metal Oxide Semiconductor (MOS) structure (gate, source, drain, emitter and metal contacts) and the back side is composed by the collector (P-doped), as shown in Figure 1.10.

Electrons move from the front side (metallic structures) to the back side (collector side). Although today the wafer thickness is around 40 μm, there is a trend to thin down wafers and it should be divided by two in the next two years to achieve 20 μm in 2012.

A decreasing of the wafer thickness will lead to an increasing of electrical performances, since the distance covered by electrons is shorter, there will be less energy losses and concurrently the frequency can be increased. If the wafer thickness is reduced, it is necessary to implant a buffer layer (N-doped) under the collector (P-doped) on the backside (see Figure 1.11) in order to prevent the collector from being damaged from a massive electrical field when switching off the device. A high activation rate of both collector and buffer layer is then required. To achieve this, it is necessary to apply an annealing process able to reach very high temperatures while not damaging the front side metallic structures. Consequently, the heat brought by the annealing process must be localized only in the doped layers of the back side, at a depth ranging from 0,1 to 1 μm. The processes usually applied nowadays, like Rapid Thermal Annealing (RTA) or flash lamps, cannot be used in this doping process since they involve a thermal budget leading to the destruction of metallic structures (these structures are damaged at temperatures higher than 400°C at equilibrium). Using the LTA technique in the partial melting regime, the collector (P-type) can be activated due to a melting process and a subsequent liquid-solid epitaxial regrowth whilst concurrently the buffer layer (N-type) is activated on solid phase, where dopant evolution is related to implant damage evolution during the laser irradiation.

Sabatier *et al.* in their investigation used Boron for the collector and Phosphorous for the buffer layer [80], implanting the P atoms first. Samples were annealed with the Excico LTA 1502TW Equipment based on UV long pulse Laser head (200 ns pulse duration). They have obtained box-like profiles for the B distributions and no diffusion has been observed for P atoms in solid phase.

Looking the dopant activation rate varying the laser energy density, they have observed that boron distribution has a constant activation rate ($\sim 60\,\%$). The increasing of the laser fluence only redistributes the dopant atoms to deeper regions, but the percentage of activated dopants remains almost constant due to the melting regrowth mechanism. Concurrently, about phosphorous atoms, the higher is the energy density, the higher is the activation rate. Lower fluence annealing is not sufficient to drive P dopant atoms on substitutional positions, both for the low thermal budget than to the defect presence.

Although there is a good understanding of dopant activation subsequent a liquid-solid phase epitaxial regrowth (promoted by the segregation), dopant activation in solid phase in an implanted substrate is poorly investigated. In order to better understand this mechanism models of dopant-defect system evolution have to be developed and implemented.

1.6. Modeling challenges

In this chapter we have described in detail laser process techniques allowing for property modifications of the irradiated material. We have contributed to this researches developing proper theoretical models able to reproduce the real process evolution. This simulation approach supporting the process development has been naturally suggested by the intrinsic features of the laser annealing processes (evolution of bulk and surface material properties on a scale less than micro and nanosecond). Important results have been reached in the past decades on all the material science areas which involve laser-material interaction. At the same time, many open questions still remain without a complete understanding. In the following chapters, we will deal with questions poorly investigated in the past concerning the dopant kinetics and the correlated activation evolution in implanted silicon during a laser irradiation process. As explained previously, the need to follow the bulk evolution on a time scale less than micro and nanosecond, led us to develop and implement original models for the system kinetics under study. In chapter 2 and chapter 3 we will present all the model details considering the case of dopant-defect system evolution in a silicon substrate both in solid phase (Phosphorus implantation) and the liquid one (Boron implantation). chapter 4 will deal with similar issues with a different simulation approach, i.e. by means of the Kinetic Monte Carlo methodology. Finally, we will present our results concerning laser annealing of periodic patterned devices. This investigation will throw light on the effects of the real device structure on laser annealing, considering in an explicit way the interaction of the electromagnetic field with the periodic patterned sample.

2. Continuum modeling of submicrosecond defect kinetics in silicon under laser irradiation

2.1. Overview

In this chapter we present results of our theoretical investigation on defect evolution in ion implanted c-Si at the submicrosecond time scales during a laser thermal annealing process. We applied an originally developed kinetic simulation technique where nonmelting, melting, and partial melting regimes are simulated. Our modeling considers irradiation, heat diffusion, and phase transition together with defect diffusion, annihilation, and clustering. The reduction of the implantation damage and its reorganization in defect aggregates are studied as functions of the process conditions. The approach is applied to the defect system generated by a single and double implanted Si specimens and compared to experimental data, indicating a relationship between damage reduction and dopant activation.

2.2. Introduction

Since the discovery of the transient enhanced diffusion (TED) phenomena in implanted Si, the relationship between defect kinetics, impurity diffusion, and activation in Si has attracted a considerable interest [93]. Nowadays, it is well known that the evolution of the nonequilibrium density of defects generated by the impurity implantation plays a crucial role on impurity diffusion during high (quasiconstant) temperature annealing [71]. In the current understanding and modeling of TED in thermal annealed Si, the dopant activation and diffusion are tightly related concepts since at the process time scales they occur concurrently. However, the atomic mechanisms on the basis of the two phenomena are, in principle, different. Activation is related to the recovery of the crystalline order in a damaged crystal and to the consequent incorporation of impurities in (generally) substitutional equilibrium positions. Diffusion is related to defect mediated migration events of the impurities from a (generally) substitutional equilibrium position to another equivalent one.Anyhow, an accurate modeling of the damage (defects) evolution should be on the basis of both diffusion and activation understanding.

Activation without diffusion in pure crystal phase has been evidenced in ultrafast processes in Si, characterized by an extreme reduction in the annealing time (from the millisecond [88] to the nanosecond regime [80]) and a correspondent increase in the peak temperature. These processes eventually use the laser irradiation as a heat source [56, 80]. In particular, melt and nonmelt activations of implanted dopant in submicrosecond laser thermal annealing (LTA) process has been demonstrated experimentally [80]. In the molten region, activation is the consequence of impurity segregation, while in the solid region it is the consequence of damage reduction. As a consequence, the post-implant kinetics of the defect-dopant system in the extremely far-from-the-equilibrium conditions caused by the laser irradiation both in the non-melting and the melting regime is the main fundamental question.

The main task of the research work discussed in this chapter is the development of an accurate and reliable PDE based modeling of these phenomena. Most of the studies done so far deal with constant temperature processes. From this point of view new models have to be developed which consider the possibility of a space and time dependent thermal field due to the laser irradiation. In these conditions *all the physical parameters which are considered constant in a RTA process (e.g. diffusivity, nucleation rate, etc.), vary with the space and time during laser annealing in a very large range of values.* Moreover, especially for point and clustered defects on silicon, there are sets of parameters which are derived by fitting the experimental data for a constant temperature process. This *ad hoc* calibration does not work correctly for processes in a different temperature range. For the laser annealing process a unique set of parameters has to be fixed for the whole temperature range. This is one of the great challenges of our work.

2.3. Defects in silicon

Self-interstitials and vacancies are the fundamental building blocks for microdefect formation in crystalline Si. At the same time, these two defects are the mediators for impurity diffusion and clustering [23]. Point defects, by means of diffusive events, interact among them giving rise to aggregates or clusters. The relative concentrations of such clusters in the Si lattice are ruled by an Ostwald ripening process, driven by the formation energy decrease with size: larger clusters grow at the expense of smaller ones, whilst point defects freed from smaller and less stable agglomerates. The characterization of small clusters is difficult due to their critical size with respect to the resolution possibility of micrography techniques (for instance the Transmission Electron Microscopy (TEM) technique). Moreover, the theoretical investigation, applying fundamental (e.g. ab-initio) simulation techniques, is made difficult by the great variety of the possible atomic configurations. At the size of several hundred point defects these aggregates can be reliably studied with TEM; they are known as extended defects and, generally, show regular atomic structures with respect to the periodic lattice.

2.3.1. Point defects

Vacancies are the simplest intrinsic point defects in Si, consisting in missing Si atoms in an otherwise tetrahedrally coordinated lattice site. Their high mobility makes them not directly detectable at the typical processing temperature range. This fact has a direct impact on the characterization of their physical properties at such temperatures.

The experimental values of the vacancy formation energy vary between 2 to 4 eV. At the same time, similar quantities, evaluated through ab-initio calculations, range from 3 to 6 eV [73, and references therein]. Several experimental methods have been employed in order to characterize the diffusivity of vacancies: Electron Paramagnetic Resonance (EPR) for direct measurements at low temperatures, and via their effect on the diffusion of dopants and metals for indirect high temperature detections. Concerning the temperature dependence of the defect diffusivity, an Arrhenius-type expression is usually assumed:

$$D = D_0 \exp\left(\frac{-E_m}{k_B \cdot T}\right),$$

where D_0 is a constant (usually given in [cm^2/s]) and $E_m$is the migration energy (usually given in [eV]).

The experimental estimates of the migration energy range from 0.3 to 4 eV. In turn ab-initio calculations predict values at the lower boundary of the experimental range, between 0.3 and 0.4 eV [73].

The self-interstitial is formed once a substitutional Si atom leaves or is pulled away from its lattice site, reaching a non-lattice site between ordered atoms. Self-interstitials have been implicated as the origin of rodlike defects observed in Czochralsky single-crystal growth, which can ultimately have harmful effects on the Si device performances. Generally, in order to modify the bulk electronic properties of semiconductor substrate, dopant atoms are introduced by means of different techniques. Ionic implantation is the most commonly used, especially on the micro-device industrial production. In the implantation step, a large amount of point defects (interstitials and vacancies) are introduced in the crystal lattice. During the subsequent thermal treatment, their interaction with dopant atoms causes an anomalous increase of impurity diffusion, called Transient Enhanced Diffusion (TED). This effect has to be taken into account in the technological processes, because it alters the junction depth.

A great number of theoretical studies have been devoted to determine the configuration and energetics of the Si self-interstitial, as well as its diffusive behavior (i.e., ab-initio [10], Tight Binding (TB) [95], and empirical potential calculations [97]). However, different authors report different conclusions concerning the Si self-interstitial properties, even when the same calculation techniques are applied. Discrepancies can be found in the determination of the configuration with lowest formation energy and the microscopic description of the interstitial-mediated diffusion mechanism.

At least four possible configurations have been identified for the interstitial defect in Si: tetrahedral (T), dumbbell (D), hexagonal (H) and extended (E). Most authors indicate the D configuration as the one with the lowest energy (2.2-3.4 eV), although there are contrasting publications for the same issue. At the same time, there is not a clear agreement also regarding the microscopic description of interstitial diffusion, where very different diffusion mechanisms have been proposed, with migration energies ranging from 0.1 to 1.9 eV [73, and references therein].

2.3.1.1. Extended defects

The vacancy cluster stability depends on its size. From an experimental point of view, the lifetime of vacancy clusters has been evaluated around 400 ps for sizes between V_3 and V_{10}(the subscript indicates the particle number that forms the cluster) by means of positron annihilation experiments. Voids show a more stable behavior, and have been observed directly by TEM. They organize into octahedral structures aligned almost exclusively along the $\{111\}$ crystallographic planes of the Si lattice. The stability of the Si(111) surface, when compared to other orientations explains this phenomenon. Fundamental simulation techniques have allowed to estimate the thermodynamics and binding properties of these vacancy clusters [11, 33]. Concerning small vacancy clusters, it has been found that certain sizes, as V_6, V_8 and V_{12}, show greater stability. This is related to particular bond reconstructions in the crystalline Si lattice [11]. On the other hand, according to Sb diffusion and Au labeling experiments, the binding energies of clusters with larger sizes approach a value of around 3 eV [40, 100].

During ion implantation processes of semiconductor substrates, the generated point defects aggregate in small clusters. Post-implantation

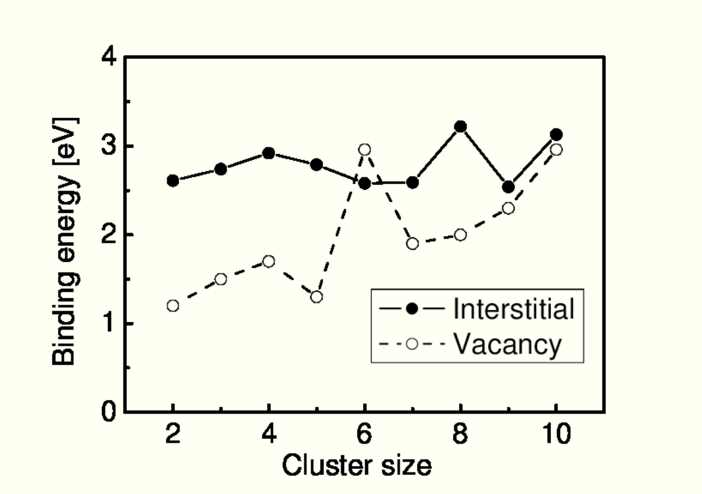

Figure 2.1.: Binding energy for vacancy (open circles) and interstitial (full circles) clusters as a function of cluster size (from Refs. [30, 37]).

annealing causes a growth of bigger size clusters at the expense of a decrease of small populations. This phenomenon is called Ostwald ripening process. Si self-interstitials are then released from this reservoir causing the TED of interstitial-diffusing dopant impurities such as B. From B diffusion experiments, Cowern *et al.* deducted the formation energy of small interstitial clusters using the concept of Ostwald ripening and the fact that the Si interstitial supersaturation, and therefore B diffusion, is related to their stability. The most important finding is that oscillations of the binding energies occur for small, discrete, “magic” sizes (likewise the vacancy case). These more stable clusters correspond to configurations where atoms remain four-fold coordinated. For larger sizes, of around one hundred atoms, {113} defects start to form. Their atomic structure was determined by Takeda using TEM [94]. {113} defects consist of large interstitial chains along the 110 direction, packed together along the {113} plane, which gives the defect name.

It has been experimentally shown that {113} defects grow in length along the 110 direction. In the process, their formation energy decreases from 0.8 to 0.65 eV [19]. If {113} defects grow up to a certain size, they can transform into dislocation loops, perfect (PDLs) and faulted (FDLs). This transformation has been proposed to be due to some unfaulting reactions, as it has been theoretically studied recently by ab initio simulation techniques [72]. The formation energy of FDLs tends to 0.027 eV with increasing size, while it tends to 0 for PDLs [19].

2.4. Continuum model

In order to understand the mechanism which lies on the basis of dopant activation under laser annealing in solid phase silicon, a reliable model for predicting the evolution of defect systems is fundamental. We will deal with this problem developing a reliable continuum model. It will account for all possible reactions between point and clustered defects, the diffusion of the mobile species as well as the Ostwald ripening process experimentally observed by several authors. The implemented model is formed by two decoupled modules: the first solves the thermal problem by means of the phase field methodology (please note that it has been widely described on subsection 1.4.3 and will be briefly reported on the next subsection); the second, rules defect evolution when the time and space dependence of the thermal field is numerically evaluated. We have implemented the PDE based continuum model developed and determined the corresponding numerical solutions in different conditions using the COMSOL solver (see webpage www.comsol.com) of differential equations (Appendix A).

2.4.1. Thermal problem

A phase-field methodology ([41, 49, 50, 104, and references therein]) was applied for the simulation of the melting. As showed in detail in subsection 1.4.3, a continuum field φ (with $-1 \leq \varphi \leq 1$, being $\varphi = -1$ and $\varphi = 1$ in the pure liquid and solid phases, respectively) is used to describe smooth phase transitions. The phase field and heat equations, modeling thermal field and phase transition evolution[41] in the laser annealing process, are:

$$\tau\frac{\partial\varphi}{\partial t}=W^2\nabla^2\varphi-\varphi\left(\varphi^2-1\right)-\lambda\frac{c_p}{L_{fus}}\left(T-T_M\right)\left(\varphi^2-1\right)^2 \quad (2.1)$$

$$\rho c_p\frac{\partial T}{\partial t}-\nabla^2\left(KT\right)=\frac{\rho L_{fus}}{2}\frac{15}{8}\left(\varphi^2-1\right)\frac{\partial\varphi}{\partial t}+S\left(x,t\right), \quad (2.2)$$

where $S(x, t)=E_{las}P(t)(1-R)a\,exp(-ax)$ is the heat source due to the absorption of laser light. $E_{las}$is the incident laser energy, $P(t)$ is the normalized laser pulse shape, and R and a are the phase and temperature dependent surface reflectivity and the material absorption at the laser wavelength, respectively. All the material properties (heat capacity c_p, heat conductivity K, and density ρ) are phase and temperature dependent. The implemented values are listed on Table C.1 of Appendix C.

2.4.2. Defect system model

In order to simulate the defect evolution, the point defects (i.e., interstitials I's and vacancies V's) and the clustered defects (clusters for I's, voids for V's) are taken into account. The defect evolution is ruled by rate equations of the following form [12]:

$$\frac{\partial C_X}{\partial t}=-\nabla J_X+R_X, \quad (2.3)$$

where C_X and J_X are the density and flux of a defect X (I or V, respectively). The flux term J_X is the sum of the diffusion term (Fick law), an electric field (E) drift term (due to charged particles), and a thermal field drift term [53],

$$J_X=-D_X\left(\nabla C_X+\frac{q}{k_BT}nE+C_X\frac{\nabla T}{T}\right), \quad (2.4)$$

where q is the electron charge and n is the density of charge. The latter quantity, calculated by means of the Poisson equation, depends on the active components). The diffusivity D_X is written in the general Arrhenius-type expression [17]

$$D_X = D_0 \exp\left(\frac{-E_m}{k_B \cdot T}\right). \tag{2.5}$$

R_X accounts for the point defect I-V and point defect-cluster interactions [30]:

$$I + V \Longleftrightarrow 0 \tag{2.6}$$

$$X + X_{n-1} \Longleftrightarrow X_n \tag{2.7}$$

$$I_n + V \Longleftrightarrow I_{n-1} \tag{2.8}$$

$$V_n + I \Longleftrightarrow V_{n-1}. \tag{2.9}$$

In particular

$$R_X = -R_{I,V} + R_C \tag{2.10}$$

$$R_{I,V} = k^f_{I,V} \cdot \left(C_I \cdot C_V - C_I^\star \cdot C_V^\star\right) \tag{2.11}$$

$$k^f_{I,V} = 4\pi \left(D_I + D_V\right) r_{capt}, \tag{2.12}$$

where r_{capt} is the capture radius of I-V annihilation.

Concerning clustered defects, in order to reduce the number of equations, a reduced model is adopted. R_C accounts for point defect-cluster interactions. Clusters with sizes up to nine are taken into account explicitly with specific dissolution energies:

$$\frac{\partial C_n}{\partial t} = k_n^f \cdot C_X \cdot C_{X_{n-1}} - k_n^b \cdot C_{X_n} + k_{n+1}^b \cdot C_{X_{n+1}} - k_{n+1}^f \cdot C_X \cdot C_{X_n} \tag{2.13}$$

$$k_n^f = \alpha \cdot 4\pi \cdot D_X \cdot r_n \tag{2.14}$$

$$k_n^b = \beta \cdot D_X \cdot C_X^\star \cdot r_{n-1} \cdot \exp\left(\frac{Q - E_{diss}^n}{k_B \cdot T}\right), \tag{2.15}$$

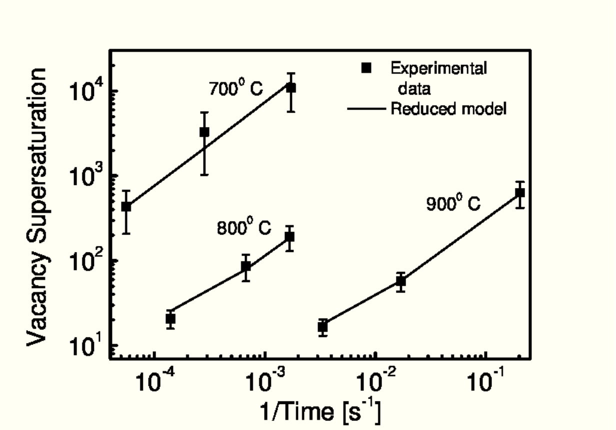

Figure 2.2.: Experimental [100] and simulated vacancy supersaturation. A reduced model is adopted where clusters with sizes up to 9 only are taken into account explicitly. Bigger clusters energetics are considered to be equivalent to that of large voids with a unique reaction rate.

$C_I^\star$	$43.0 \cdot 10^{25} \cdot \exp\left(\frac{-3.95eV}{k_B \cdot T}\right) \left[cm^{-3}\right]$
$C_V^\star$	$33.9 \cdot 10^{23} \cdot \exp\left(\frac{-3.3eV}{k_B \cdot T}\right) \left[cm^{-3}\right]$
D_I	$0.34 \cdot \exp\left(\frac{-1.00eV}{k_B \cdot T}\right) \left[\frac{cm^2}{s}\right]$
D_V	$1.23 \cdot 10^{-3} \cdot \exp\left(\frac{-0.5eV}{k_B \cdot T}\right) \left[\frac{cm^2}{s}\right]$
r_{capt}	$2.725 \cdot 10^{-8} \left[cm\right]$

Table 2.1.: Free defect parameters implemented in the PDE model and KMC code for the dopant-defect system evolution [13].

where r_n and E^n_{diss} are the capture radius and the dissolution energy of X_n cluster, Q the activation energy of the product $D_X \cdot C_X^\star$, a and β are calibration parameters. We assume that the bigger clusters X_{Cl} are ruled by the same energetics of the extended defects. As a consequence, defects with size $n \geq 10$ are ruled by a unique reaction equation

$$\frac{\partial C_{Cl}}{\partial t} = k_9^f \cdot C_X \cdot C_{X_9} + 0.1 \cdot k_{Cl}^f \cdot C_X \cdot C_{X_{Cl}} - 0.1 \cdot k_{Cl}^b \cdot C_{X_{Cl}}. \quad (2.16)$$

In any case, as in Ref. [53], the cluster diffusion is neglected. The defect density dependent expressions for the reaction rates and the formation/dissolution coefficient formulations are taken from Ref. [30]. Free defect parameters (see Table 2.1) were taken from Ref. [13]. Interstitial cluster parameters (dissociation energies and capture radius) are taken from Ref. [30].

Concerning the vacancy cluster parameters, their literature consists of a smaller amount of works. This is also related to the experimental issues about their characterization. As a consequence, a clear and wide convergence about their binding energy does not exist. We have chosen to extract them, fitting our reduced model on a real vacancy supersaturation experiment conducted by Venezia *et al.* [100]. Figure 2.1 shows the obtained binding energy for vacancy (open circles) and interstitial (full circles) smaller clusters. Their explicit values

	$I_nE^n_{diss}$ [eV]	$V_nE^n_{diss}$ [eV]	$r_n[\AA]$
X_2	3.61	1.70	1.92
X_3	3.74	2.00	3.84
X_4	3.92	2.20	5.76
X_5	3.79	1.80	7.68
X_6	3.58	3.46	9.60
X_7	3.59	2.40	11.52
X_8	4.22	2.50	13.44
X_9	3.54	2.80	15.36
Sub_i_{cl}	-	-	17.28
X_{Cl}	4.13	3.46	15.60

Table 2.2.: Cluster parameters implemented in the PDE model and KMC code (see chapter 4) for the dopant-defect system evolution [30, 37].

are also listed on Table 2.2. We adopted these extracted values in all the simulations performed with the continuum approach in this thesis. Results of the fitting procedure are reported on Figure 2.2, which shows the comparison between experimental [100] and simulated vacancy supersaturation. The good agreement validates our binding energy calibration.

Defects are not present in the liquid state. However, in order to allow the continuity of the field equations in the solid and liquid regions, free defects were forced at their equilibrium concentration at melting temperature, while clusters are assumed to be entirely dissolved.

2.5. Experiment

Two different experimental configurations have been analyzed and simulated. We implanted three N-type wafers with a crystalline orientation <001> and a resistivity of 12 Ω/cm. Firstly, dopant and defect evolution in a single implanted substrate (P 200 keV energy, 10^{14} cm^{-2}

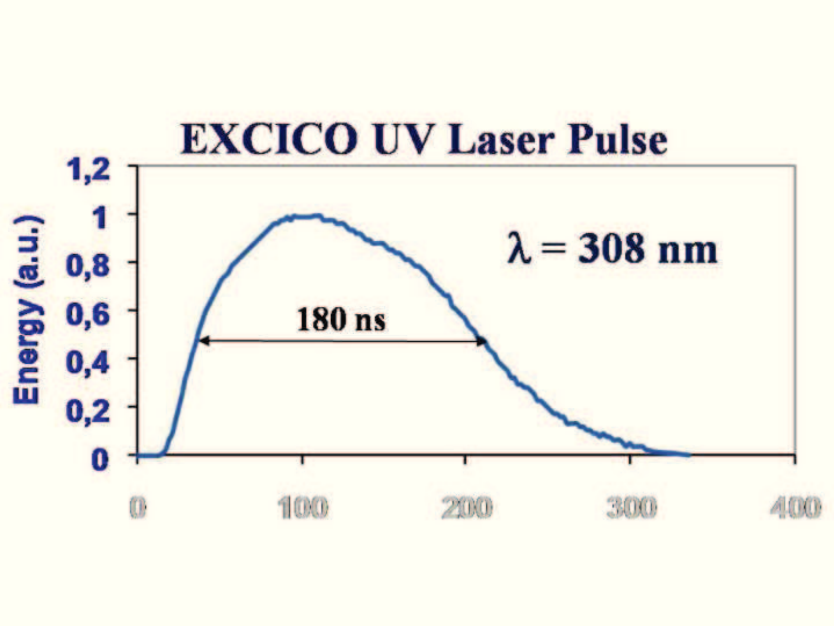

Figure 2.3.: Laser pulse shape as a function of the time for the EXCICO LTA15 laser (wave length λ = 308 nm, pulse duration 180 ns).

dose) under LTA has been studied. The experimental samples have been annealed using the EXCICO LTA15 laser (λ = 308 nm) at room temperature, with a pulse duration of 180 ns and 1 Hz frequency in the multiple pulse case[80]. A square processed area of 15 × 15 mm^2 is considered. Figure 2.3 shows the laser pulse shape as a function of the time. As an example, we reported on Figure 2.4 the corresponding time evolution of the temperature at three different position for the 2.6 $\mathrm{J/cm}^2$ laser process: solid, dash and dot lines refer, respectively, to the thermal field at 0.0, 0.5 and 1.0 μm deeper from the irradiated surface (0.0 μm).

The study of defect evolution and dopant activation in solid phase silicon is the central point of our investigation. Hence, the laser fluence has been set in order to obtain non-melting, partial melting and full melting processes with respect to the dopant implant projected range. From this point of view, considering the discussion in the following of this thesis, the points at distance 0.5 and 1.0 μm from the surface (Figure 2.4) are particularly representative, showing the temperature variations near the maximum melt depth and on the bulk region, respectively.

Laser energy densities of 1.6, 2.0, 2.6, 3.0, and 3.6 J/cm^2 have been considered in single or multi-shot configurations (up to 5 pulses). The regrowth yields single crystalline material for all the samples as verified by TEM analyses. Figure 2.5 reports a TEM image of the single P implanted substrate after a laser irradiation process with 3.6 J/cm^2 density energy. Three distinct regions can be identified from the surface (right) to the bulk (left): one bright region which corresponds to the molten and regrowth crystalline silicon ($\sim$ 0.35 μm, also verified by SIMS and simulation data); one darkest region where dopant and end-of-range defects reside; the third (less dark) region which corresponds to bulk silicon. The color contrast is due to the presence of the implanted phosphorus atoms.

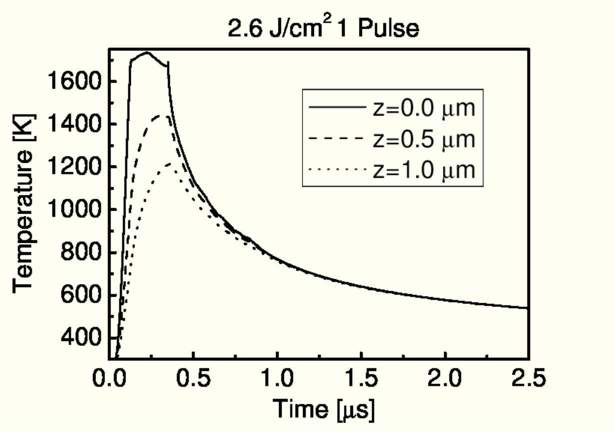

Figure 2.4.: Time evolution of the temperature at three different position for the 2.6 J/cm^2 laser process: solid, dash and dot lines refer, respectively, to the thermal field at 0.0, 0.5 and 1.0 μm deeper from the irradiated surface (0.0 μm).

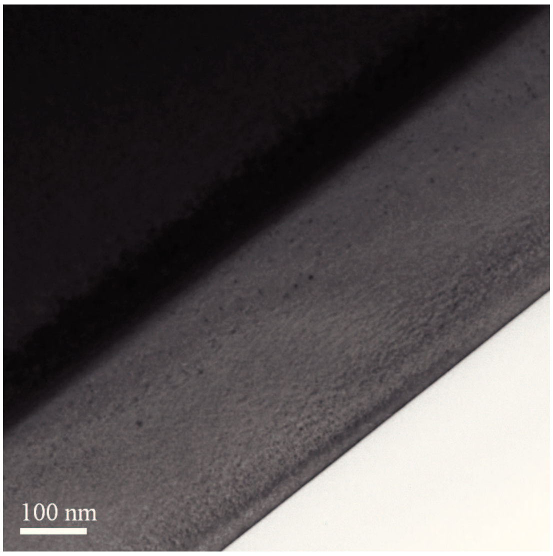

Figure 2.5.: Transmission electron microscopy of a section of the single implanted substrate (P 200 keV energy, 10^{14} cm^{-2} dose) after a laser irradiation process with 3.6 J/cm^2.

Figure 2.6 shows the simulated melt depth (solid line) as a function of laser energy density, in excellent agreement with those extracted from secondary ion mass spectroscopy (SIMS) measurements of diffused B profiles (full squares). The latter profiles show the typical boxlike shape in the molten region (fluences: 2.6, 3.0, and 3.6 J /cm^2), which allows the melt depth determination. The transient evolution of the melt depth, simulated for these three different fluences, is shown in Figure 2.7.

LTA processes have been performed also in a double implanted silicon structure (B 40 keV, 3×10^{14}cm^{-2} and P 350 keV, 1×10^{14} cm^{-2}). The samples have been annealed using the same laser equipment. Laser energy densities of 3.5, 4.5, and 5.0 J/cm^2 have been considered. Chemical and electrical P profiles have been analyzed by means of Secondary Ion Mass Spectroscopy (SIMS) and Spreading Resistance Probe (SRP), respectively.

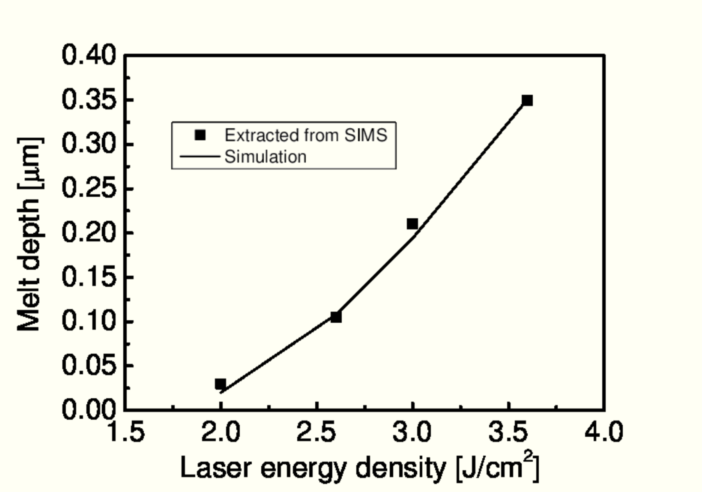

Figure 2.6.: Melt depth as a function of laser energy densities (2.0, 2.6, 3.0, and 3.6 J/cm2). Simulation estimates are shown as solid line while rectangles indicate SIMS measurements.

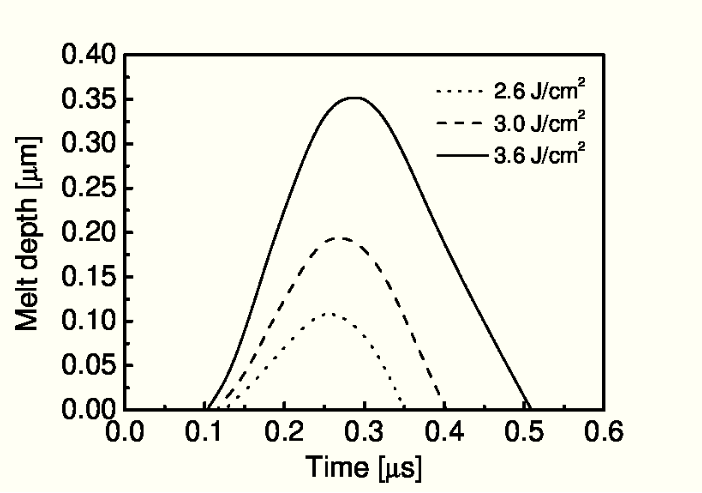

Figure 2.7.: Time evolution of the melt depth during the melting laser processes for 2.6 (dot), 3.0 (dash) and 3.6 (solid) J/cm^2 laser fluences.

2.6. Results and discussion

2.6.1. The initialization problem

Defect initialization is a notable point of our investigation due to the highly non-equilibrium character of the LTA processes. In particular, during the development of the final model, various initializations have been implemented in order to quantify their impact on the final defect distribution after the laser irradiation processes. During a dopant implant process, damage cascades are created by the penetrating ions. The cascades are formed by interstitial silicon atoms which leave their substitutional sites creating vacancy defects.

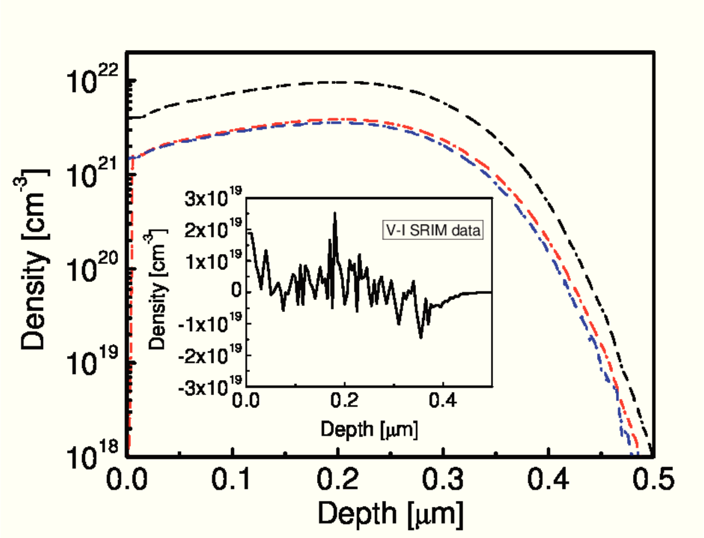

Figure 2.8.: Total interstitial (dash) and vacancy (dot) defect density: dark lines refer to the as implanted defects obtained by SRIM simulation; red and blue lines refer, respectively, to the residual defect density after room temperature evolution obtained from the PDE model and from the KMC simulation. The inset shows the difference between total I- and V-type defects as obtained after SRIM simulation.

At the same time, due to their evolution at the implantation temperature, a re-organization of the point defects in small cluster aggregates and a reduction due to interstitial-vacancy annihilation occurs. An implant simulation code generally give the exact amount of the damage cascade in terms of point defect distributions (interstitial, vacancy and dopant) ignoring their thermal evolution. As a consequence, assumptions have to be done for the damage reduction and its reorganization in clusters.

Simulations of standard constant temperature processes adopt the $+1$ or $+n$ assumption for the defect initialization, which considers only 1 or n interstitials for implantation (with the same space distribution of the implanted dopant, all stored in I_2 defects and without vacancy defects). Consistently with the $+n$, the interstitial-vacancy annihilation process is neglected, since the simulation starts effectively after its end. This initialization can not be used for submicrosecond laser annealing simulations where we are in a stage of the kinetics strongly affected by the interstitial-vacancy annihilation. In principle, since we aim to simulate defect evolution in ion implanted c-Si at the submicrosecond time scales, different initializations can lead to different results and a reliable defect scenario after the implantation process which takes into account the evolution of the collisional cascades is fundamental.

The reference defect profile generated by the implantation has been determined with the aid of SRIM simulations based on the Binary Collision Approximation (BCA). The total amount of interstitial defects is equal to those of vacancies (unless of the sputtered atoms from the implanted surface) with different shifts in space distributions. The defect evolution at the implant temperature during and after the process leads to a reduction in the total defect dose and the resulting post-implantation damage is stored in small defect aggregates [38]. Figure 2.8 shows the total interstitial (dash) and vacancy (dot) defect density: dark lines refer to the as implanted defects obtained by SRIM simulation; the red line refers to the residual defect density after room temperature evolution obtained by means of the PDE model of subsection 2.4.2. In this case we have also simulated the room temperature evolution with a Kinetic Monte Carlo (KMC) simulation (blue

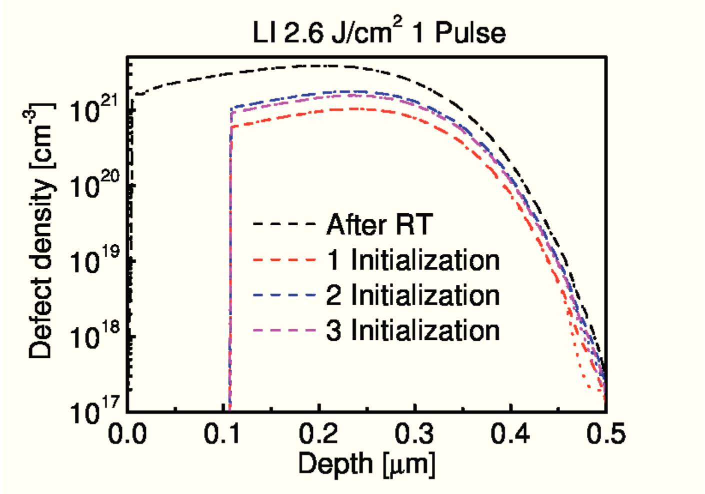

Figure 2.9.: Post anneal total interstitial (dash line) and vacancy (dot line) defect density after one pulse laser irradiation (2.6 J/cm^2). Red, blue and magenta lines refer to simulations based on defect initialization 1, 2, and 3 as described in the text (Sec. 2.6.1). Dark lines refer to the simulated total interstitial and vacancy defects after room temperature evolution (case 3).

line) described in detail on chapter 4. A perfect agreement can be found in terms of the damage reduction with both simulation methods leading to an overall decrease of 40 % of the total implantation damage.

In order to test the effect of different initializations, the damage cascade was implemented (after room temperature evolution) in three different ways:

1. assuming that all the initial implant defects are in size N=2 clusters [30];
2. considering an initial cluster size distribution, equal for I and V defects, obtained for a system formed by only vacancy defects;
3. directly simulating the evolution of the implantation defect (SRIM data) with the continuum model of subsection 2.4.2, as previ-

ously described.

Figure 2.9 and Figure 2.10 resume the results of this investigation. In particular, Figure 2.9 shows the post anneal total interstitial (dash line) and vacancy (dot line) density after one pulse laser irradiation (2.6 J/cm^2) for simulations based on the three defect initializations. Note that I and V distributions are always superimposed due to fast rates of the point defect-point defect or point defect-cluster interactions with respect to the particle diffusion. Results indicate that the largest damage reduction occurs for the (1) initialization. This fact is due to the incorporation of initial defects only in clusters with size 2, which have the lower binding energy. The choices (2) and (3) with an initial cluster distribution result in less frequent dissolution events.

The post anneal total interstitial cluster density after one pulse laser irradiation (2.6 J/cm^2) is shown on Figure 2.10. Red, blue and magenta lines refer to simulations based on defect initialization 1, 2, and 3 as described in the text (Sec. 2.6.1). Empty and full symbols indi-

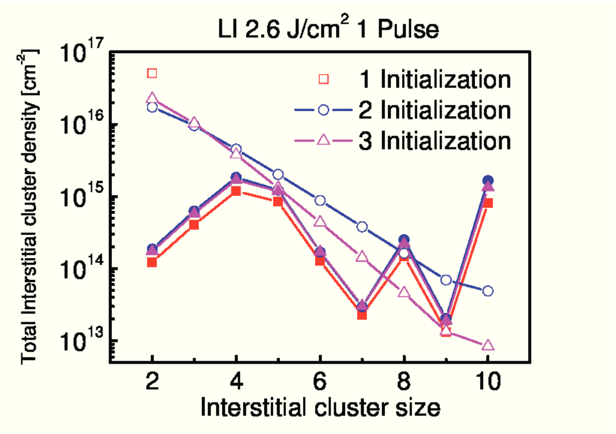

Figure 2.10.: Post anneal total interstitial cluster density after one pulse laser irradiation (2.6 J/cm^2). Red, blue and magenta lines refer to simulations based on defect initialization 1, 2, and 3 as described in the text (Sec. 2.6.1). Empty and full symbols indicate the value at the start and the end of the laser process.

cate the value at the start and the end of the laser process. The choice 2 has been implemented in order to investigate the effects of cluster size distribution on defect annihilation. As we can see in Figure 2.10, the final cluster size distributions after one pulse laser annealing do not depend on the particular choice of initial defect distribution.

Our preferred final choice was the third initialization, i.e. the coupling of Binary Collision Approximation (BCA) and continuum simulations for the defect evolution at the implant temperature. The simulated initialization is free from arbitrary assumptions and reflects properly the real process conditions.

2.6.2. Single implanted silicon structure

The evolution of the dopant-defects system under LTA for the experimental configurations described before (P single implant on Si) was simulated. Laser energy densities in the range of 1.6-3.6 J/cm^2 have been considered. In Figure 2.11 the post anneal total interstitial and vacancy defect density for three laser processes is shown. On the other hand, the post anneal total defects after the two different partial melting processes (2.6 and 3.0 J/cm^2) are similar near the maximum melt depth. Figure 2.12 and Figure 2.13 report some results for Interstitial and Vacancy type defects, respectively. In particular, defect (free and clustered) spatial distributions after multi-pulse LTA for the 2.6 J/cm^2 (top panels), 3.0 J/cm^2 (central panels) and, 3.6 J/cm^2 (low panels) fluences are compared (2.5 μs after the end of each laser pulse). Note that due to the fast quenching no evolution is observed after this time and before the subsequent pulse [37]. Three particular contributions are shown in the figures: i.e. free interstitial/vacancy (dot lines), defects in clusters with sizes less or equal to 9 particles (dashed line) and clusters with dimensions greater than 10 defects (solid line only for the I's since for V's the density of large defects is negligible). The dark, red and blue lines refer respectively to 1, 3 and 5 laser pulse processes.

In the non-melting process (1.6 J/cm^2 laser fluence, not shown), the extended defect density is negligible, compared to the other contributions (free I and small clusters). Due to the short timescale of the

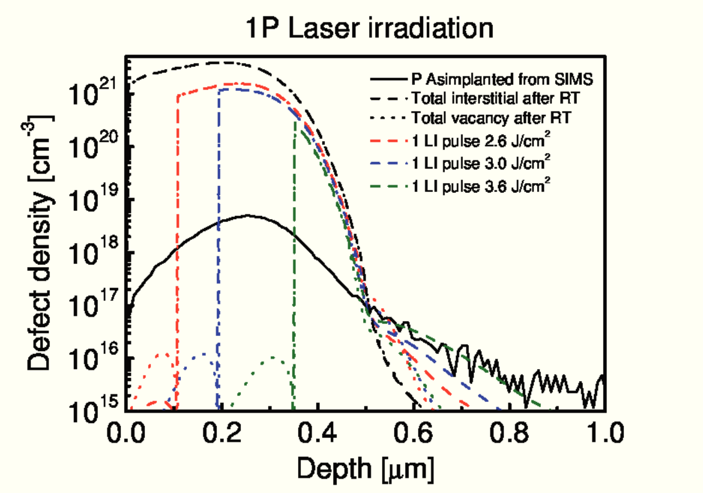

Figure 2.11.: Post laser anneal total interstitial (dash) and vacancy (dot) defect density for 2.6 (red), 3.0 (blue) and 3.6 (green) J/cm2 laser fluences. Dark dashed and dotted lines refer, respectively, to the simulated total interstitial and vacancy defects after the implantation (choice 3 of Sec. 2.6.1). The dark solid line shows to chemical P as-implanted profile.

process and the low fluence, the overall thermal budget supplied to the system in the pure sub-melt regime is not sufficient to drive consistently the Ostwald ripening phenomenon. At higher fluences, two regions can be observed: the melted region, where the defects are fully annealed (concentration at equilibrium value) and the sub-melt region, where the defects are partially annealed. In turn, Ostwald ripening occurs only for larger fluences. This is shown for the 2.6, 3.0 and 3.6 J/cm^2 case in Figure 2.12.

The process evolution leads to the formation of bigger clusters in the non-molten region in the proximity of the melt depth and, at the same time, an annihilation of the total damage system. As a consequence, for this large energy density case, although the total I cluster density decreases, I's tend to form bigger aggregates. In any case the smaller cluster profile follows the free defect profile. Concerning multi-shot

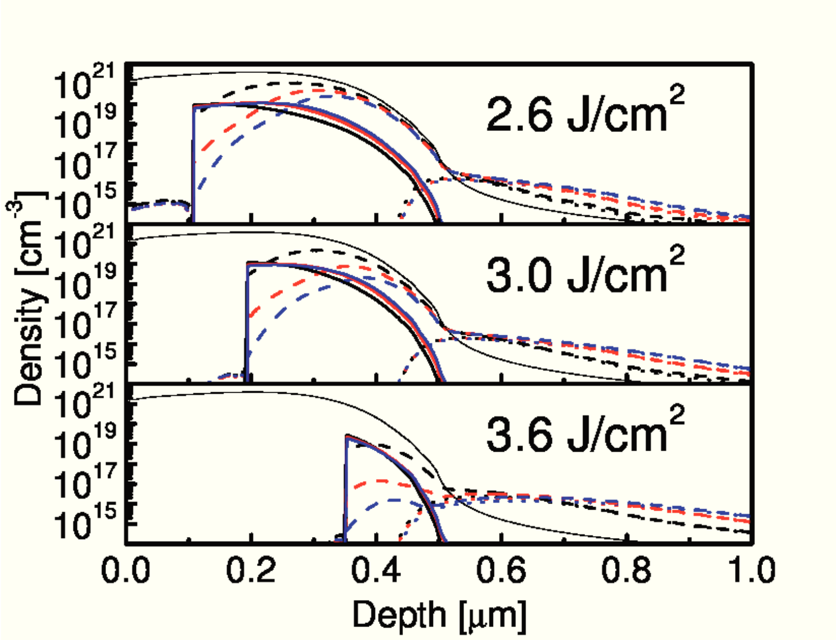

Figure 2.12.: Interstitial (free and clustered) spatial distributions after multi-pulse LI for the 2.6, 3.0 and, 3.6 J/cm^2 fluences. Three particular contributions are shown: i.e. free interstitial (dot line), interstitials in clusters with dimensions less or equal to 9 particles (dash line) and clusters with dimensions greater than 10 interstitials (solid line). The dark, red and blue lines refer respectively to one, three and five laser pulse processes.

processes, a similar trend can be found for the I defect distributions with the increase of the number of pulses.

The scenario is slightly different for vacancy-type defects. As found for interstitial-type defects, we have a reduction of free and small clustered vacancies with the fluence and the pulse number. No ripening phenomenon occurs for all the conditions simulated as can be observed in Figure 2.13. The residual V eventually form only small V clusters after the LTA process. Anyhow, *large V clusters should not be observed in these experimental conditions.* In summary, for the LI

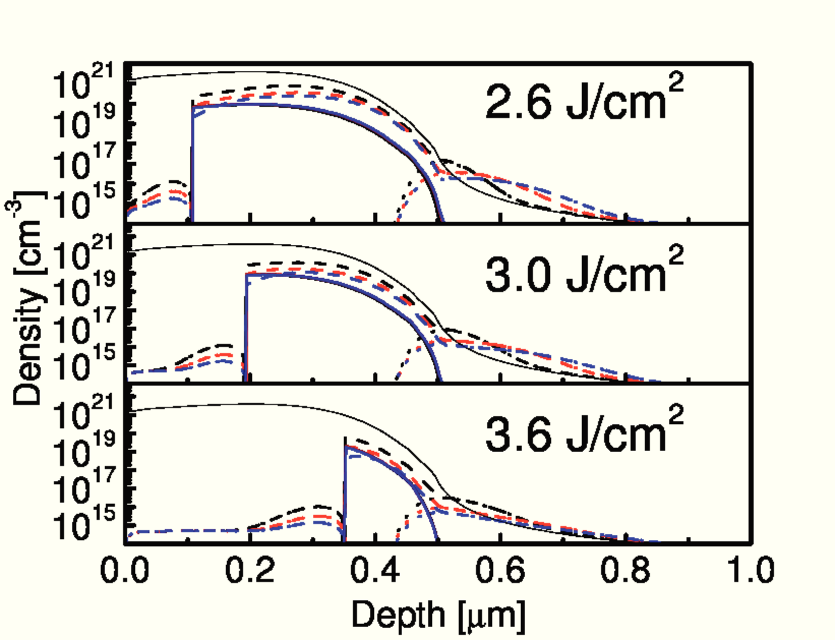

Figure 2.13.: Vacancy (free and clustered) spatial distributions after multi-pulse LI for the 2.6, 3.0 and, 3.6 J/cm^2 fluences. Three particular contributions are shown: i.e. free vacancy (dot line), vacancies in clusters with dimensions less or equal to 9 particles (dash line) and clusters with dimensions greater than 10 interstitials (solid line). The dark, red and blue lines refer respectively to one, three and five laser pulse processes.

process with a 180 ns pulse, defects are fully annealed in the melted region. In the submelt regions only I type clusters undergo to a ripening phenomenon while vacancies are stored to small size defects.

2.6.3. Double implanted silicon structure

The kinetics of the defect system have been simulated for the double implanted samples [37]. As widely described on subsection 1.5.2, the investigation of this substrate can have a direct impact on future IGBT power device performances. Laser fluences of 1.3, 2.5, 3.5, and 4.5 J /cm^2, respectively, have been investigated. Similar results have been found like in subsection 2.6.2 for the defect evolution in the single implanted substrate. In particular, a reduction in the I and V concentrations as the energy density increases has been found. In the pure nonmelt case (1.3 J /cm^2), the total defect density is only slightly reduced due to the relatively small thermal budget supplied to the system. At higher fluences, two explicitly separated regions can be seen: the melted region, where the defects are fully annealed (concentration at equilibrium value) and the sub-melt region, where the defects are partially annealed. Overall residual damage after melting processes is thus shown to be considerably reduced. However, a significant reduction in the damage occurs in the submelt region.

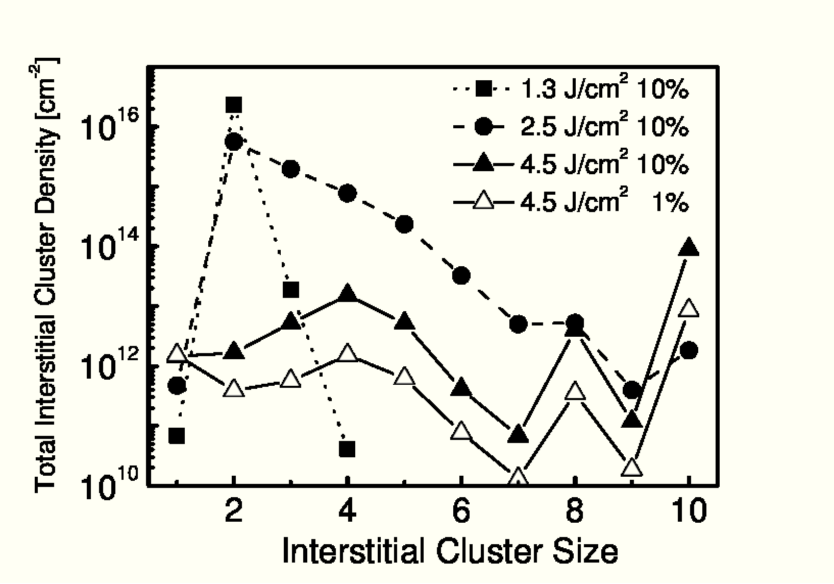

Figure 2.14.: Interstitial clusters size distribution after LTA for 1.3 J /cm^2 (squares), 2.5 J /cm^2 (circles), and 4.5 J /cm^2 (triangles) fluences. Results obtained for the 4.5 J /cm^2 fluence but with a different initialization (1% reduction in I-V pair due to dynamic annealing during the implant) are also shown as open triangles.

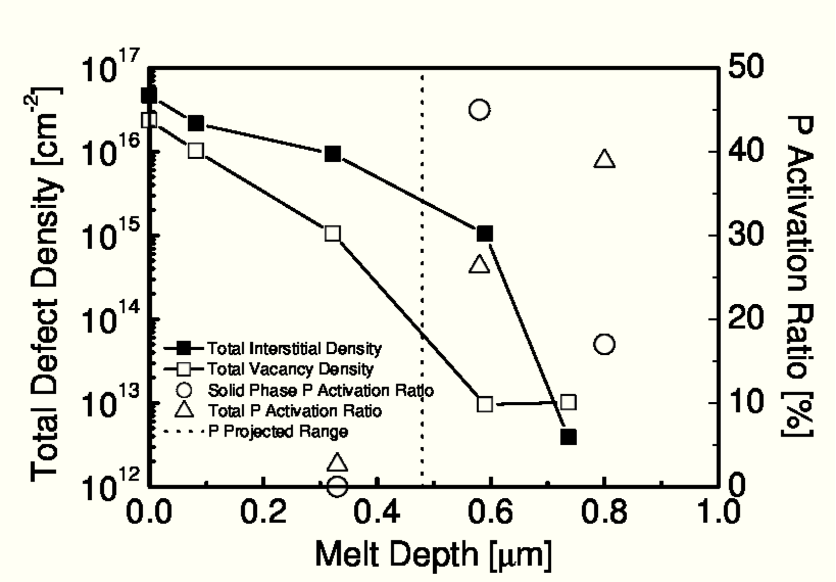

Figure 2.15.: Simulated total I (full squares) and V (open squares) defect density and experimental P activation ratio as a function of melt depth. Total activation ratio (triangle) and solid phase activation ratio (circles) are shown. The P projected range (dashed line) is also indicated.

As the fluence is increased, a progressive enhancement of the defect annihilation efficiency in the solid region can be observed. In Figure 2.14, the total interstitial cluster densities after LTA, essentially left in the nonmelted regions, are plotted for 1.3, 2.5, and 4.5 J /cm^2 laser energy densities. In the 4.5 J /cm^2 case the same quantity is also shown for a different initialization (1% reduction). As it can be seen, in the submelt regions, a relevant fraction of the residual I type defects resides in clusters (small and large). Due to the short time scale of the process, the thermal budget supplied to the system in the pure nonmelt regime is not sufficient to drive consistently the Ostwald ripening phenomenon. In turn, the Ostwald ripening occurs for larger fluences. Indeed, although the total I cluster density decreases, interstitials tend to form larger aggregates. Concerning V type defects, on the contrary, clustering is less pronounced in all the cases considered.

Thanks to spreading resistance probe (SRP) measurements, our experimental analysis has shown that dopant activation takes place in double implanted (B and P) silicon samples after the LTA. In the solid regions near the melt depth position, signatures of partial defect anneal, absence of dopant diffusion, and partial P activation have been highlighted. The molten region is characterized by full defect annealing and high dopant activation. Indeed, the activation ratio of B remains almost constant ($\sim 60\,\%$) for all the laser energies considered [80]. Concerning P, its total activation ratio (Fig. Figure 2.15 triangles) was shown to increase with the laser energy density. Since the full P implant is not melted, part of it is annealed in the solid phase. The solid phase activation ratio (Figure 2.15 circles) was obtained integrating SIMS and SRP profiles below the melt depth. Therefore, the results show that the P activation is also driven by the thermal budget received in the solid phase.

As it can be seen in Figure 2.15, where $C^{\mathrm{tot}}_{\mathrm{I,V}} = \sum_n nC^n_{\mathrm{I,V}}$ (where n is the cluster size and C_n is the corresponding density) are also shown, there is a strong correlation between defect annealing and P activation. Therefore, partial P activation in the submelt region and high activation in the melt region are due to two different mechanisms. In the melted region it is due to dopant relocation in substitutional sites during recrystallization from the melt, while in the submelt region it is mainly due to defect annealing. It can be noted that for the largest fluence case only the tail of the P profile is activated by means of the solid phase mechanism. A detailed understanding of the atomic mechanism of the activation will be discussed in the next chapter. However, it is significant to note that a relevant activation occurs only when the residual damage is dominated by I type defects only (namely when the $+n$ conditions occur).

2.7. Conclusion

In this chapter a detailed model has been presented for the defect evolution in implanted silicon during an excimer laser irradiation. The continuous field approach allows a direct and rapid implementation of the whole particle interaction set. However, these advantages cost in terms of the *ad hoc* calibration of the introduced equation parameters. We will investigate the same issues with a different simulation methodology, i.e. Kinetic Monte Carlo simulations, on chapter 4. One of its advantages lies on the nature of its approach, where parameters can be directly estimated came mainly from fundamental theoretical calculations. However, continuum modeling results predict similar trend to the KMC ones.

Concerning the results obtained with the investigation reported in the present chapter, our simulations of the damage evolution during a submicrosecond LTA process suggest that a relevant fraction of the residual I type defects in the submelt region resides in clusters, whereas V type clustering is less pronounced. Besides, a strong correlation between the total defect annealing and the activation ratio increase was highlighted, thus underlining that point defects have a significant role on dopant activation. Our analysis shows that significant activation occurs only when damage evolution leads to a significant unbalance between the V and I type defects and that the residual damage is characterized by large I clusters.

In the next chapter we will introduce in the theoretical method the kinetics of dopant atoms and all the related defect-dopant interactions. An analysis of the different components evolution (interstitial, substitutional, and trapped on clustered defects) and comparison with experimental activation profiles (obtained by means of SPR measurements), will allow us to predict and understand how implant dopant atoms can be activated using laser irradiation as heat source.

3. Continuum modeling of dopant-defects system evolution in silicon

3.1. Overview

The following chapter will deal with the implanted dopant evolution in silicon under laser irradiation in sub-melting, partial melting and full melting regimes. Two main issues will be discussed.

The first issue is the investigation of the activation mechanism in phosphorous implanted silicon under excimer laser irradiation. For this purpose, the activation efficiency in the solid phase has been measured in a wide range of irradiation conditions, varying the laser fluence and the number of shots. The total active fraction varies in a range spanning several orders of magnitude and shows a complex trend depending on the process conditions. Our continuum model is able to explain the whole scenario.

In the last part of the chapter, we will report our investigation on the dopant evolution mechanism in the melting phase of boron implanted silicon under laser irradiation. In particular, laser processes where the maximum melt depth is much larger than the implanted B ions projected range are considered (i.e. the implantation defects are fully annihilated by the melting). Experimental analysis suggests that the dopant evolution and its re-distribution in the molten regions can be divided in three different regimes as a function of laser fluence (or the maximum melt depth): against-gradient, pile-up and no-pile-up regimes. We elucidate the dopant evolution mechanism in the melting phase considering the possibility of two different states governing the dopant diffusion in a tight temperature range around the melting temperature.

3.2. Introduction

Laser Thermal Annealing receives a great interest in the formation of ultra-shallow junctions essential in nanoscale metal-oxide-semiconductor technology [2, 35, 70, and references therein]. A sequence of ion implantation and thermal processing is commonly used to modify the electronic properties of semiconductors.

The solid phase diffusion triggers the evolution of the material from a state that is far from equilibrium (after the implantation) to a stationary state. The fabrication of ultra-shallow junctions in Si device technology has stimulated the detailed study of this evolution. In spite of the deep understanding achieved nowadays of the non-equilibrium phenomena ruled by defect-defect coupling [38, 47, 48] and the interactions between defects and impurities in Si [71, 87, 93], diffusion and activation are not usually considered as two independent observables to be simulated concurrently in the framework of evolution models for impurities-damage systems.

At the time scale of the conventional thermal processes, diffusion and activation are strongly correlated, since diffusion is due to the mass transport of the impurity active fraction. In this conditions the activation kinetics is usually neglected. However, the two phenomena are intrinsically different: activation follows the rearrangement of the crystal from the post-implant damaged state, allowing the incorporation of the impurities in substitutional equilibrium positions; diffusion is a sequence of random migration events between two substitutional equilibrium positions also triggered by the formation of defect-dopant highly mobile species. As a consequence, the activation observation could precede the evidence of diffusion, if the rate of the activation mechanism is larger with respect to that of the diffusion one, as often occurs in ultrarapid annealing processes. Indeed, *diffusion-less activation* is observed in post-implanted crystal Si annealed at very high temperatures ($T > 1100$ °C) and with short annealing times (from the ms [88] to the ns regime [80]). Diffusion-less activation is, therefore, the signature of very fast dynamics inside the impurity-damage system without a net mass transport.

Laser irradiation is the principal method used to achieve the annealing conditions that lead to the diffusion-less activation phenomenon [56, 80]. In particular, the melt and non-melt activation of implanted dopants in the sub-microsecond laser irradiation (LI) process has been demonstrated experimentally [80]. Some preliminary investigations on this subject have been reported, indicating that the interaction between defect and dopant in the solid region plays a crucial role [25, 37]. However, a comprehensive set of experimental data and satisfying theoretical predictions of the diffusion-less activation are still lacking. Note that LI is a unique tool for studying this issue, but the peculiar thermodynamic conditions induced by this process (fast varying nonuniform thermal field, phase transition) make combined experimental and theoretical research necessary in order to correctly explore the singularities of the laser process related to the dopant activation.

As many unsolved issues arise on dopant-defect evolution and dopant activation in solid phase Si under laser annealing, similarly open questions make not complete the understanding of dopant evolution in the melting phase. A laser melting process should produce a boxlike profile after a liquid-phase epitaxial recrystallization of the melted region. This is possible due to the high dopant diffusivity in liquid Si, which is about eight orders higher than that in solid Si [45]. The near unity segregation coefficient of common dopants such as boron, phosphorus, and arsenic during the highly nonequilibrium recrystallization process also contributes to the boxlike profile [75, 107]. This highly non-equilibrium recrystallization process also results in a high concentration of dopant incorporation that exceeds the solid solubility due to a solute trapping mechanism [5, 107]. One point still not understood, which is object of discussion still today, is the dopant pile-up commonly observed at the melt depth region. Indeed, many experimental works have revealed a dopant (boron or arsenic) pileup near the maximum melt depth in bulk Si after a laser irradiation process with a deep melting [61]. We try to investigate and elucidate the mechanism which is at the basis of this phenomena.

The idea of the proposal mechanism comes from the silicon properties in liquid phase just above the melting temperature. In particular, anomalous temperature dependence of the physical properties of l-Si have been observed in that temperature range by Kimura and coworkers, such as the density [82, 83], the surface tension [84], the viscosity [86], and the electrical resistivity [85]. For temperatures lower than about 1430 °C, the density and the viscosity show a steep increase. Above 1425 °C, the surface tension increases with decreasing temperature with the temperature coefficient being negative, however, the temperature coefficient of the surface tension becomes positive at about 1425 °C and returns to a negative value just above the melting point. The temperature coefficient of the resistivity is negative near the melting point of Si and positive for higher temperature, the resistivity of molten Si shows a local minimum in the range from 1450–1500 °C. They suggest that changes in the melted structure, such as interatomic distance, coordination number, and local ordering, lead to this anomalous behavior [55]. On the other hand, due to their similar short range order, the dopant evolution mechanism in liquid phase could be closer to that of dopant in amorphous phase than on crystalline silicon [59].

Starting from these observations we have developed a model for the dopant evolution in the liquid phase. In particular, for the case of boron pile-up, we have assumed that B atoms can be in two different states, one at higher diffusivity than the other, where the temperature in the molten region rules the corresponding concentrations. In particular, dopant atoms in the lower diffusion state reside in regions with a temperature range just above the melting point of Si ($\sim$ 9 K higher that the silicon melting point, i.e. neighbor to the maximum melt depth), whilst atoms in the higher diffusion state are in the remaining liquid regions.

3.3. Dopant evolution in solid phase

As outlined at the end of chapter 2 (subsection 2.6.3), dopant activation efficiency by laser annealing in implanted silicon solid phase is strongly related to the defect system introduced with the dopant implantation process. Consequently, a reliable understanding of the activation mechanism has to take into account the defect system evolution and dopant-defect interactions during a laser irradiation process. We will try to extend the continuum defect model widely described in subsection 2.4.2, introducing impurity atoms. All the relevant interactions between dopant atoms and free or clustered defects will be considered in the model. A comparison between experimental measurements and simulation results for the case of implanted phosphorus on silicon, will allow us to test the continuum model and increase the current understanding on these attractive issues.

3.3.1. Dopant-defect interaction in silicon: the case of phosphorus

During the microelectronic device fabrication, dopant atoms are introduced on the processed substrate by means of ion implantation. The process, more advantageous from an economic and implementation point of view, introduces undesired defects in the region where ions have been implanted. Dopant atoms, placed in random interstitial position, will become electrically active only if they migrate in a substitutional position. Impurity atoms may occupy either substitutional or interstitial positions in the Si lattice (see Figure 3.1). Impurity atoms utilized in the doping such as boron (B), phosphorus (P), and arsenic (As) occupy substitutional positions where the dopant atoms supply free electrons or holes to the silicon substrate. The activation step is promoted by an high temperature processing, where, consequently, impurity profiles undergo a redistribution through diffusion phenomenon. Activation in this process is a consequence of the diffusion. The redistribution of impurities may be intentional as in a “drive-in” step or unintentional as a result of high temperature oxidation, deposition or annealing process.

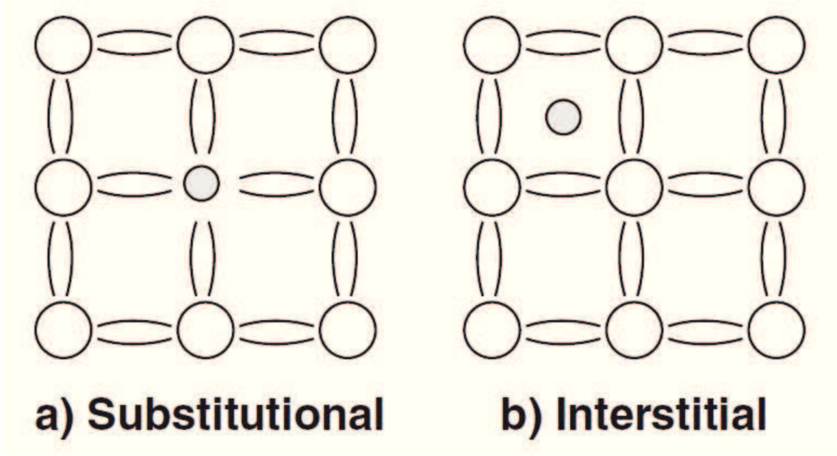

Figure 3.1.: Substitutional and interstitial impurities in silicon.

Therefore dopant diffusion is a fundamental physical phenomenon in microelectronic device fabrications. It is now well accepted that impurity diffusion is mainly mediated by native defects created in the substrate.

The movement of a substance due to diffusion is driven by the slope of the concentration profile. Impurity atom diffusion may be driven by vacancy (XV), by interstitial (XI) or by interstitialcy (X_i) - see Figure 3.2 for details. Here X, I and V denote, respectively, a dopant atom, an interstitial and a vacancy. Vacancy-driven diffusion occurs when a substitutional atom exchanges lattice positions with a vacancy (it requires the presence of a vacancy). Interstitial-driven diffusion occurs when an interstitial atom jumps to another interstitial position. Interstitialcy-driven diffusion results from silicon self-interstitials displacing substitutional impurities to an interstitial position (requires the presence of silicon self-interstitials, the impurity interstitial may then knock a silicon lattice atom into a self-interstitial position).

It is important to observe here that since dopant atoms (such as phosphorus, arsenic and boron) occupy substitutional positions once activated, dopant diffusion is closely linked to and controlled by the presence of vacancy and interstitial point defects. Whether an im-

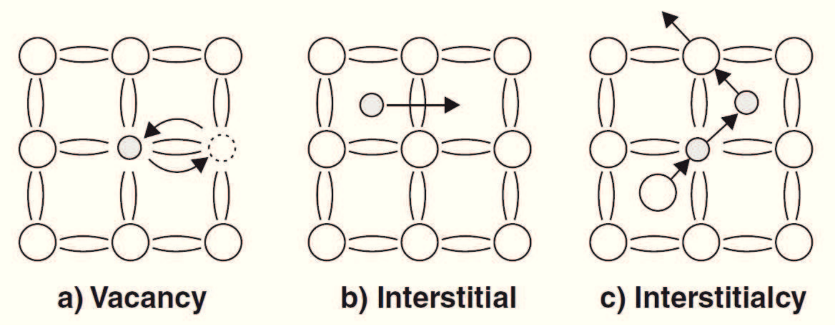

Figure 3.2.: Vacancy, interstitial and interstitialcy diffusion mechanisms of dopant atoms in silicon.

purity atom occupies a substitutional or interstitial position in single crystal silicon, the atom is trapped in a periodic potential defined by the lattice (see Figure 3.3). The probability of an atom jumping from one position to the next-neighbor increases exponentially with increasing temperature.

Concerning the phosphorus case in silicon, almost all of the early models were based on the assumption that P diffusion was dominated by a vacancy mechanism, an assumption that is now thought to be incorrect [24]. Intrinsic diffusion of P in Si has been demonstrated to be retarded under nitridation [22, 60]. Nitridation of a bare Si surface causes an injection of vacancies leading to a V supersaturation. From the degree of the retardation it was concluded that the intrinsic diffusion of P is mainly mediated by PI pairs or interstitial phosphorus P_i.

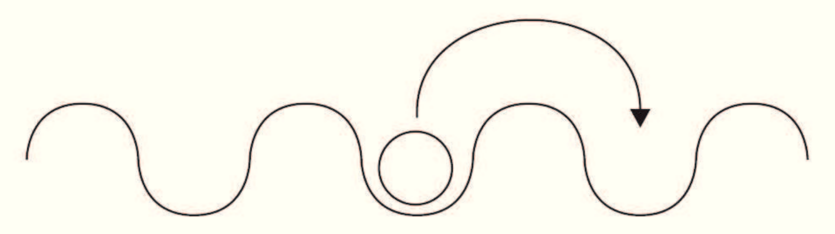

Figure 3.3.: Impurity atom diffusing along a periodic potential.

Accordingly, the fractional interstitialcy or interstitial component of intrinsic P diffusion is close to unity. For extrinsic P doping, the retardation of P diffusion under nitridation decreases [22], which indicates an increased contribution of vacancies to P diffusion. Other more recent experimental work using the point defect injection method has suggested that the fractional contribution of the I mechanism is in the range of 86%–100% [98].

While diffusion experiments are able to find the overall diffusion coefficients as well as point defect influences, they generally cannot determine the microscopic physical processes involved in the diffusion, or identify formation and migration energies separately. Recently, a combination of I and V mechanisms for P diffusion in Si has been used in continuum level simulations.

For the manufacturing of advanced devices, an essential step is the formation of highly doped ultrashallow junctions by means of ion implantation, where a complex system of diffusing and reacting defects in the silicon wafer is involved. In these conditions, the interaction of impurity atoms with defect clusters during a subsequent thermal treatment plays a key role. The formation of dopant-defects aggregates can hinder the activation process. Furthermore, in highly doped substrate, the dopant-dopant interaction can lead to inactive complexes. Several studies have investigated the clustering of As, P, and Sb in Si with *ab initio* calculations based on density-functional theory (DFT) [64, 81]. Many studies considered only defects with dopant-vacancy or dopant-interstitial pairs or other small clusters. On the other hand, the knowledge of all the defect-dopant configurations and their related binding energy is still poor. This leads to the introduction of simplified model, as well as indirect assumptions for the energetics involved in the kinetics: part of the model parameters are determined by means of fitting procedure.

In view of this considerations, our model will consider the following point defect-dopant interactions:

$$P_S + I \Longleftrightarrow PI \text{ or } P_S + I \Longleftrightarrow P_i \tag{3.1}$$

$$P_S + V \Longleftrightarrow PV \tag{3.2}$$

$$PV + I \Longleftrightarrow P_S \tag{3.3}$$

$$PI + V \Longleftrightarrow P_S \tag{3.4}$$

$$PX + X_n \Longleftrightarrow PX_n, \tag{3.5}$$

where P_S, PI and PV are, respectively, dopant atoms in the substitutional, interstitial (or interstitialcy), and vacancy configuration. X_n and PX_nindicate a cluster of n defects (I or V) and the dopant atom-cluster complex where the impurity is trapped in a defect agglomerate.

3.3.2. Experimental approach

LI processes have been performed in an implanted silicon substrate. The experimental scenario is described in detail in section 2.5 for the single implant case (P 200 keV energy, 10^{14} cm^{-2} dose). In addition to the chemical SIMS analysis, electrical P profiles have been measured by means of a spreading resistance probe (SRP). SIMS analysis, used to analyze dopant distribution after LI, shows that 1.6 and 2.0 J/cm^2 are nonmelting processes, 2.6 and 3.0 J/cm^2 are partial melting processes (melt depth lower than the P projected range), and 3.6 J/cm^2 is a total melting process (melt depth larger than the P projected range). Some examples of experimental chemical and electrical P profiles are shown in Figure 3.4 and Figure 3.5 for the case of a one pulse laser process with energy densities of 3.0 and 3.6 J/cm^2. In particular, the SIMS profile (open circles) and the SRP measurements (open triangles) are shown. Note that due to the carrier spreading, the SRP

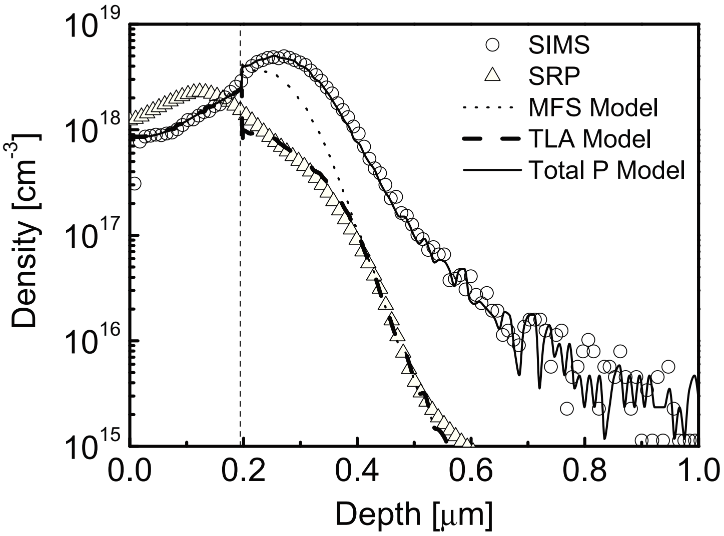

Figure 3.4.: Experimental results from SRP measurements (open triangles) and the simulated (thick dashes) P active profile as a function of depth after single pulse LI (3.0 J/cm^2) of an implanted Si substrate (P 200 keV energy, 10^{14} cm^{-2} dose). Thin dashes: the simulated P active profile with the simplified model. Solid line: the simulated total P redistribution after one pulse LI. Open circles and the vertical line refer, respectively, to SIMS analysis and the experimental melt depth after one pulse LI.

profile does not coincide exactly with the ionized impurity profiles. However, it gives a reliable characterization of the local activation efficiency and an accurate estimate of the global one (i.e., integrated over the profile). The vertical line denotes the experimental melt depth, extracted by the SIMS profile, considering the relevant profile modification in the molten region. No diffusion is observed in the non-molten region where the chemical profile coincides with the as implanted one (not shown).

Figure 3.6 shows a complete analysis of the activation in the non-

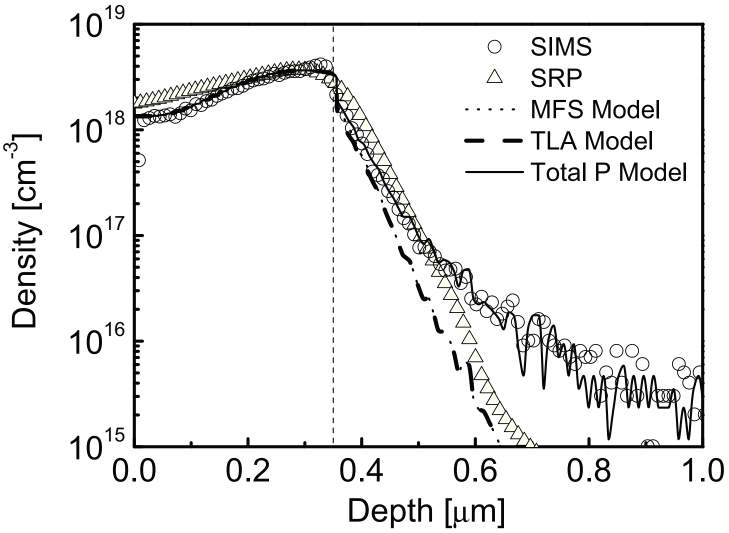

Figure 3.5.: Experimental results from SRP measurements (open triangles) and the simulated (thick dashes) P active profile as a function of depth after single pulse LI (3.6 J/cm^2) of an implanted Si substrate (P 200 keV energy, 10^{14} cm^{-2} dose). Thin dashes: the simulated P active profile with the simplified model. Solid line: the simulated total P redistribution after one pulse LI. Open circles and the vertical line refer, respectively, to SIMS analysis and the experimental melt depth after one pulse LI.

molten region (note that an almost full activation is measured in the molten zone). The solid lines refer to the solid phase dopant active ratio (i.e., the ratio between the total active dose and the chemical dose integrated in the non-molten region; see, e.g., Figure 3.4 or Figure 3.5) obtained by the SRP measurements as a function of the number of pulses for three different laser fluences (2.6 J/cm^2, 3.0 J/cm^2, and 3.6 J/cm^2). A good activation efficiency in the non-molten region can be observed when the samples are irradiated at the highest fluence, 3.6 J/cm^2 (Figure 3.5): in spite of the negligible net diffusion of the P atoms, relevant solid phase activation occurs even in the single pulse cases. In this case, the melt depth $R_{melt} \sim 0.35\ \mu m$ is significantly larger as compared to the average implantation range R_{ion}, and only the profile tail remains solid during the irradiation.

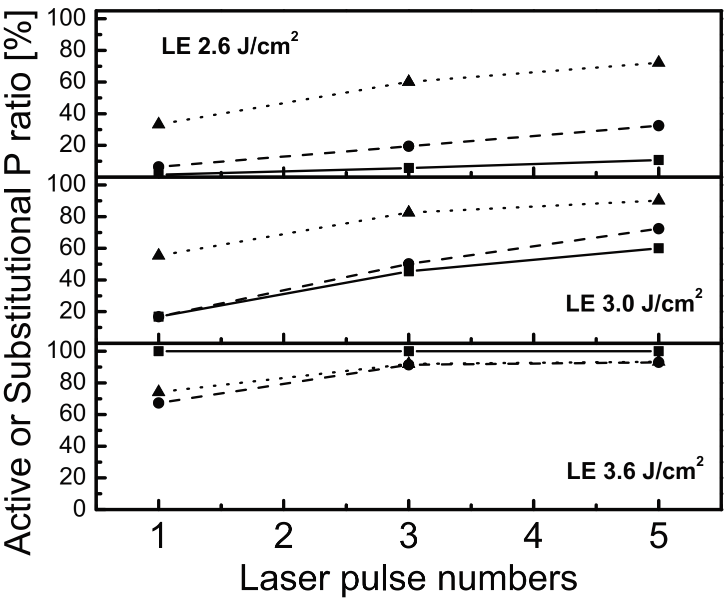

Figure 3.6.: The simulated substitutional P dopant fraction after 1, 3, and 5 laser pulses with the full model (dashed line) and the simplified model (dotted line) for three different laser processes (2.6 J/cm^2, 3.0 J/cm^2, and 3.6 J/cm^2). Solid line: experimental results from the SRP measurements solid phase active ratio (solid line).

On the other side, the solid phase activation efficiency is strongly degraded in the partial melting cases at lower fluence when $R_{melt} < R_{ion}$ ($R_{melt} \sim 0.2\ \mu m$ for the 3.0 J/cm^2 case). Moreover, when the fluence is fixed, the activation increases considerably with the pulse number. For the nonmelting processes, the activation (not shown) is very low (1%). The activation efficiency decrease for lower fluence annealing, has led us to assume that the damage cascade, which is mainly located close the P as-implanted peak, plays a crucial role.

Therefore defect-dopant interactions have to be considered in order to fully understand and correctly predict the activation evolution. Here we try to achieve a suitable theoretical description that is valid for all of the process conditions studied.

3.3.3. Simulation modeling

Our model considers the possibility of trapping limited activation (TLA) and is formed by two modules. The first accounts for the melting simulation and consists of Equation 2.1 and Equation 2.2 of subsection 2.4.1. Phase-field methodology [41, 49, 50, 104, and references therein] was applied for the simulation of the melting. A continuum field φ (with $1 \leq \varphi \leq 1$, and $\varphi = -1$ and $\varphi = 1$ in the pure liquid and solid phases, respectively) is used to describe smooth phase transitions [37]. The second module accounts for the defects-dopant system evolution. A kinetic model is used to simulate the evolution of the coupled defects-dopant system in low and medium dopant density regimes [12]. In particular, the equation system adopted for the defect evolution (free and clustered defects) and described in subsection 2.4.2 was coupled with rate equations of the following form

$$\frac{\partial C_X}{\partial t} = -\nabla J_X + R_X, \tag{3.6}$$

for the C_X density of substitutional dopant atoms P_S and dopant mobile components, where the mobile species considered are the PI and PV couples (because P diffuses only by interacting with defects) as described in detail in subsection 3.3.1. J_X is the flux of mobile defects and have the same form as Equation 2.4 of subsection 2.4.2. Parameters used to model the evolution of PI and PV couples, were taken from Ref. [25, 81] and are listed in Table 3.1. As in subsection 2.4.2, in the liquid state, free defects were forced at their equilibrium concentration at the melting temperature, and clusters are assumed to be entirely dissolved.

All of the possible reactions between mobile species, immobile active substitutional P_S, and defect clusters are taken into account. Inter-

D_{PI}	$0.453\exp\left(\frac{-3.482eV}{k_B\cdot T}\right)+\left(\frac{n}{n_i}\right)\times 1.61\exp\left(\frac{-3.647eV}{k_B\cdot T}\right)$	$\left[\frac{cm^2}{s}\right]$
D_{PV}	$8.0\times 10^{-5}\exp\left(\frac{-3.408eV}{k_B\cdot T}\right)+\left(\frac{n}{n_i}\right)\times 8.0\times 10^{-5}\exp\left(\frac{-3.128eV}{k_B\cdot T}\right)$	$\left[\frac{cm^2}{s}\right]$
E^b_{PI}	0.85	$[eV]$
E^b_{PV}	1.21	$[eV]$

Table 3.1.: Parameters implemented in the PDE model and KMC code for PI and PV couples [25, 81].

actions between I or V type defects and substitutional (P_S) or mobile (PI and PV) dopant atoms (see Ref. [30] for details), have been considered by the following reaction terms:

$$R_{Int}=k^f_{Int}\times\left[C_{P_S}\times C_I-k^b_{Int}\times C_{PI}\right], \tag{3.7}$$

$$R_{Vac}=k^f_{Vac}\times\left[C_{P_S}\times C_V-k^b_{Vac}\times C_{PV}\right], \tag{3.8}$$

$$R_{Itrap}=k^f_{Itrap}\times\left[C_{PI}\times C^{tot}_I-k^b_{Itrap}\times C_{PI\_Itrap}\right], \tag{3.9}$$

$$R_{Vtrap}=k^f_{Vtrap}\times\left[C_{PI}\times C^{tot}_V-k^b_{Vtrap}\times C_{PV\_Vtrap}\right]. \tag{3.10}$$

These equations reflect the interaction listed in subsection 3.3.1. Here k^f and k^b are the forward and backward reaction rates, respectively. The first is bound to the mobile species diffusivity, and the second to the trapping binding energy. C_I , C_V, and $C^{tot}_{I,V}$ are, respectively, the free interstitial/vacancy density and the total interstitial/vacancy cluster density ($C^{tot}_{I,V}=\sum_{n>2}C^n_{I,V}$, where n is the cluster size and C^n is the corresponding density). C_{P_S} , C_{PI}, C_{PV}, and $C_{PI\_(I/V)trap}$ are concentrations relative to substitutional dopant atoms, point defect-dopant couples, and trapped dopant in I or V

clusters. Note that in Equation 3.9 and Equation 3.10 we are assuming an equivalent trapping efficiency for defect clusters with different sizes. The backward reaction rates of Equation 3.9 and Equation 3.10 have an Arrhenius-like form, and their exponential energetic is the binding energy$E_{b_trap} = E^f_{PI} + E^f_{Cluster} - E^f_{PI+Cluster}$, which is the difference between the sum of the formation energies of the mobile defect and defect cluster and the trap complex *PI + cluster* formation energy. As we demonstrate in the following paragraphs, the dopant-cluster interaction is crucial for the explanation of the experimental trend.

The defect system has been initialized as done in the subsection 2.6.1, coupling the binary collision approximation with continuum simulations of the defect evolution at room temperature after the implant (Figure 2.8). The post-implantation damage has been stored in small defect aggregates. The as implanted P profile is used to initialize the impurity concentration. All of the P ions are considered as nonactivated P (i.e., the initial *PI* profile coincides with the SIMS profiles while the initial P_S profile is initially set to zero).

3.3.4. Results and discussion

In subsection 2.6.2 the evolution of the defect system for the same experimental configuration (P single implant on Si) has been deeply investigated. Our simulations of the damage evolution during submicrosecond LTA process suggest that a relevant fraction of the residual I type defects in the submelt region resides in clusters, whereas V type clustering is less pronounced. Besides, a strong correlation between the total defect annealing and the activation ratio increase was highlighted, thus underlining that point defects have a significant role on dopant activation. Our analysis of subsection 2.6.3 for the double implanted case, was a preliminary study of dopant activation under laser irradiation. It has been shown that significant activation occurs only when damage evolution leads to a reduction of the implant damage. In the following, with the aid of the impurity-defect model, we will quantitatively link defect evolution, investigated in the past chapter, with dopant activation.

The evolution of the defects-dopant system under LI was simulated for the experimental configurations previously described (subsection 3.3.2). A remarkable feature of our experimental activation study is the poor activation for the partial melting case, in both the peak and the tail regions of the profile (see Figure 3.7). Note that due to the strongly varying thermal field induced by the laser annealing and the consequent significant thermal budget decrease moving from the melt depth to the bulk, we could expect a lower activation efficiency in the tail region of the profile in the partial melting case with respect to the sample irradiated at a larger fluence. In order to quantify this aspect, we compare in Figure 3.7 the maximum temperature as a function of the position simulated in the solid region for the 3.0 and 3.6 J/cm^2 cases. The maximum temperature in the tail region is $\sim$ 100 °C larger in the higher fluence case. Moreover, we show in Figure 3.8 and Figure 3.9, for the 3.0 and 3.6 J/cm^2 cases, respectively, the time evolution of the thermal field at three different points: 0.10, 0.25, and 0.40 μm beneath the maximum melting depth. In the same position (0.45 and 0.60 μm

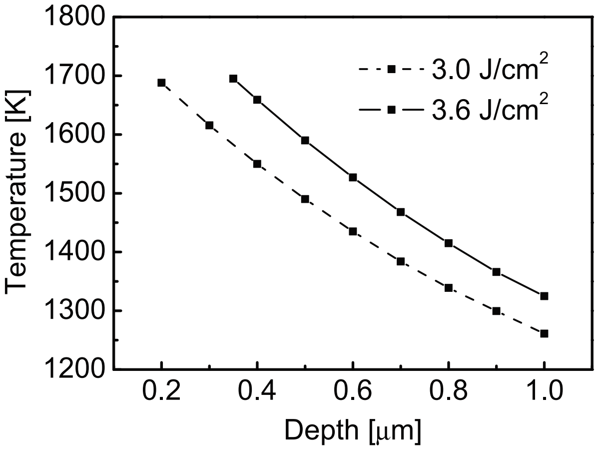

Figure 3.7.: The maximum temperature as a function of the position simulated in the solid region for the 3.0 J/cm^2 (dashed line) and 3.6 J/cm^2 (solid line) processes.

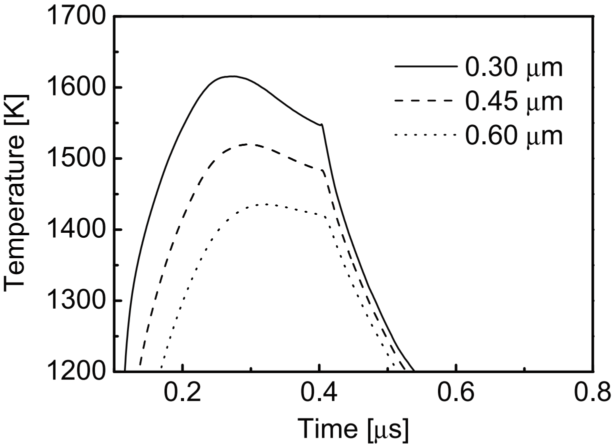

Figure 3.8.: Time evolution of the temperature at three different positions for the 3.0 J/cm^2 laser process: solid, dashed, and dotted lines refer, respectively, to the thermal field at 0.10, 0.25, and 0.40 μm beneath the maximum melt depth (0.194 μm).

beneath the irradiated surface), higher temperatures are maintained for longer intervals for the larger fluences.

We could naively conclude that the reduced thermal budget with depth causes the lower activation efficiency for the partial melting conditions. The thermal budget could explain only the activation trend in the tail region of the profile in terms of an Arrhenius type process [29]. However, a relatively low activation efficiency also can be observed in the peak region of the 3.0 J/cm^2 case. This cannot be explained by the thermal budget argument only, because this region is near the melt depth, and dopant atoms became active in regions near the melt depth for the 3.6 J/cm^2 process (see Figure 3.5). As a consequence, all of this evidence indicates that residual damage and its evolution have a crucial role in the dopant activation. On the other hand, the dopant regime analyzed, i.e., with a relatively low dose and large energy of the implantation, ensures that P-P interactions can be neglected without any significant accuracy loss (i.e.,

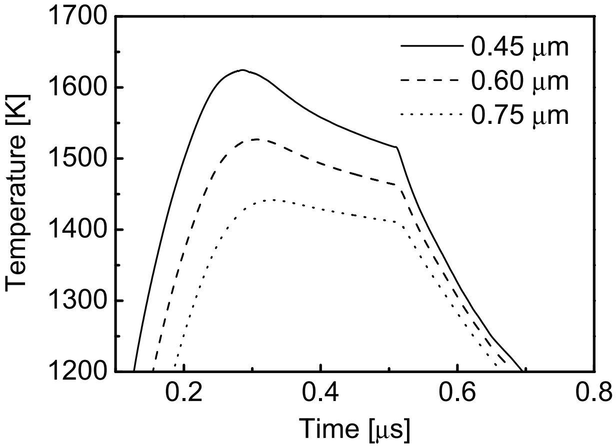

Figure 3.9.: Time evolution of the temperature at three different positions for the 3.6 J/cm^2 laser process: solid, dashed, and dotted lines refer, respectively, to the thermal field at 0.10, 0.25, and 0.40 μm beneath the maximum melt depth (0.351 μm).

activation/deactivation does not depend on P aggregates). This interaction comes into play for higher P concentrations, where it leads to inactive P clustering, and additional equations have to be coupled to the model [96].

In principle all the possible reactions between residual damage and dopant atoms (described in detail in subsection 3.3.1) can play a role in the solid phase dopant evolution. Firstly, we investigated the role of point defects on dopant activation and their interaction with impurity atoms, neglecting Equation 3.5, i.e. any trapping effect with small and bigger defect aggregates. Therefore, dopant evolution has been simulated with a modified five stream (MFS) model for the defect-dopant interaction (which consts of the first four reactions described by Equation 3.1 to Equation 3.4 of subsection 3.3.1). A modeling analysis [25] of the single shot case succeeds in the prediction of the activation for the full melting case, but it fails completely to describe the partial melting cases. Figure 3.10 clarifies the scenario caused by point defect-dopant interactions. In particular, free interstitials (dash) and vacancies (dot) for the 2.6 J/cm^2 (upper panels) and 3.6 J/cm^2(lower panels) laser processes are shown. Their time evolutions near the maximum melt depth (0.2 and 0.4 μm from the irradiated surface) indicate that a maximum value of $\sim 10^{18}$ cm^{-3} is reached by the interstitial density and $\sim 10^{19}$ cm^{-3} for the vacancy one after 0.12 μs from the start of laser irradiation. Their space distributions indicate that the free defect densities for the two defect classes are similar for the 2.6 J/cm^{2}and 3.6 J/cm^{2}laser processes. These observations are consistent with simulation results of dopant evolution, which consider only free defect-dopant interaction (Modified Five Stream model). Point defects (I or V) can not interact with dopant atoms which have reached a substitutional position for the laser processes considered here.

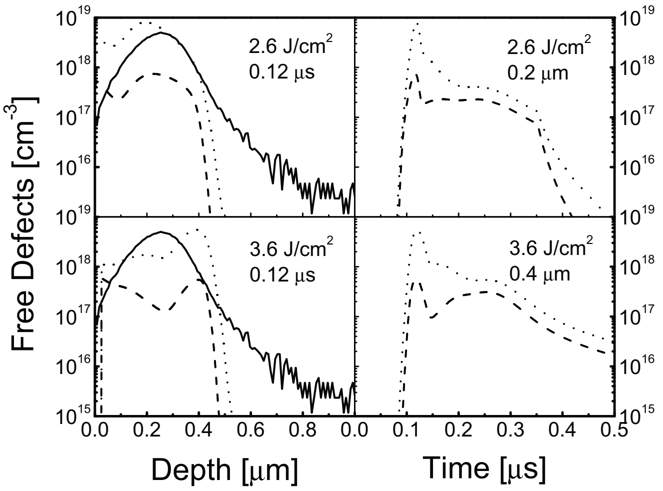

Figure 3.10.: Free interstitilals (dash) and vacancies (dot) for the 2.6 J/cm^2 (upper panels) and 3.6 J/cm^2(lower panels) laser processes. In particular, their space distributions at 0.12 μs from the laser irradiation start (left side) and time evolutions at 0.2 and 0.4 μm from the irradiated surface (right side) are shown. The solid line refers to the P as-implanted profile extracted by SIMS analysis.

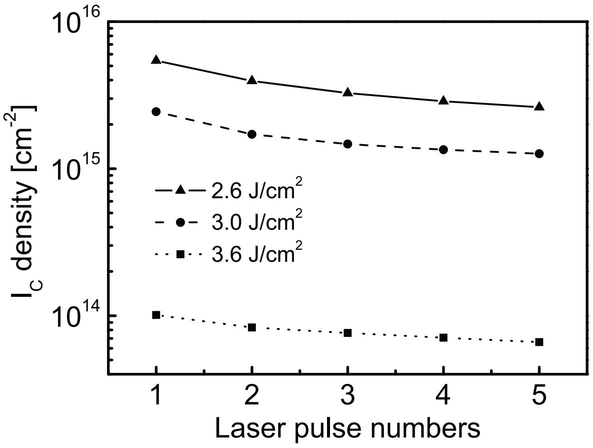

Figure 3.11.: Postanneal total interstitial cluster density as a function of the number of pulses. Solid line: 2.6 J/cm^2; dashed line: 3.0 J/cm^2; dotted line: 3.6 J/ cm^2.

These results indicate that clustered defects must play a fundamental role. In Figure 3.11 and Figure 3.12, the postanneal total interstitial/vacancy cluster density $C^{tot}_{I,V}$ as a function of the laser pulse number is shown. Note that cluster densities and cluster size distributions are only weakly affected by the trapping reactions in Equation 3.7 and Equation 3.10, because the defect density is much larger with respect to the impurity density. Solid, dashed, and dotted lines refer, respectively, to 2.6 J/cm^2, 3.0 J/cm^2 , and 3.6 J/cm^2 laser fluences. Values are extracted after the end of each multi-pulse LI. The simulation results suggest a decrease in the defect cluster density with the increase of the laser fluence and the number of pulses. Although the total I cluster density decreases, I's tend to form bigger aggregates (Ostwald ripening process). Concerning multi-shot processes, a similar trend can be found for the I defect distributions (not shown) with an increase in the number of pulses. The scenario is different for vacancy-type defects. As found for interstitial-type defects, we have a reduction of both free and small clustered vacancy concentrations with the fluence and number of pulses. However, in this case whereas V type clustering is less pronounced. These results suggest that the trapping of impurities by the defect clusters must be taken into account in order to correctly model the activation trend: clustered defects affect the dopant evolution, leading to a lower activation efficiency for the partial melting processes in the region where a high P density is present, because high concentrations of clustered defects reside in this region. In the case of the total melting process (3.6 J/cm^2), trapping should have a limited role in the activation efficiency due to the lower concentration of clustered defects.

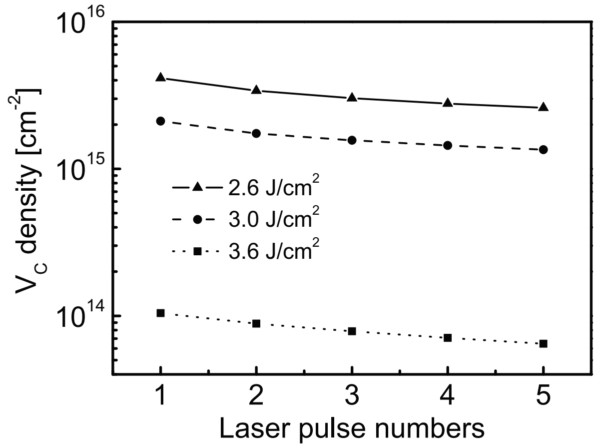

Figure 3.12.: Postanneal total vacancy cluster density as a function of the number of pulses. Solid line: 2.6 J/cm^2; dashed line: 3.0 J/cm^2; dotted line: 3.6 J/cm^2.

The comparison between the SIMS profile and the simulated chemical P profiles demonstrates that the model correctly predicts the dopant redistribution in a partial melting process. Moreover, considering carrier spilling in the SRP measurements, a reasonable agreement emerges from the comparison between the SRP profiles and the simulated P_S profile for the 3.0 J/cm^2 case (thick dashes in Figure 3.4). Note that if we neglect cluster trapping (MFS model), a strong discrepancy between the P_S (thin dashes in Figure 3.4) and SRP profiles can be observed, with the former being one order of magnitude larger than the latter near the peak of the total P density. However, this discrepancy correctly does not emerge in the 3.6 J/cm^2 case (see Figure 3.5), where the simulated P_S profiles from the MFS and TLA models are almost overlapping due to the weak effect of the trapping (differences cannot be appreciated in the logarithm scale-only in the linear one, as in Figure 3.6). Thus, the TLA model captures the general trend of the diffusion-less activation phenomenon in the total and partial melting LI processes.

The prediction of the P_S for the 2.6 J/cm^2, 3.0 J/cm^2, and 3.6 J/cm^2 fluences is in good agreement with the experimental SRP measurements. Figure 3.6 shows the complete simulation results obtained with the TLA model (dashed lines), which predicts a correct trend for the active dopant fraction, confirming that residual damage evolution rules dopant activation in the defect-rich regions. Also for the non-melting processes, 1.6 and 2.0 J/cm^2, the simulated active dopant fractions (not shown) are very low ($\sim 1\,\%$), in agreement with the experimental data. Note that the dotted line in Figure 3.6 shows substitutional P dopant fractions obtained with the MFS model [25]. It predicts, in most cases, a higher dopant fraction in the P peak region than in the experimental one for partial melting laser conditions. This discrepancy and the corresponding reliable prediction of the TLA model can be better understood by analyzing the free and clustered defect kinetics. In particular, in the MFS model, activation is limited by the defect supersaturation only, which is similar for both partial melting and full melting processes - see Figure 3.10[25]. This results in similar activation rates in all cases (Figure 3.6). In contrast, the TLA model correctly relates the activation efficiency to the reduction of I's and V's clusters with an increase of the laser energy and the number of pulses. The calibration suggests a value of $\sim$ 0.5 eV for the difference$E^f_{PI} - E_{b_trap}$. This value approaches a similar energy, but for I's and V's clusters, fitted to experimental data and used in the adopted reduced model that rules the bigger defect clusters' evolution (0.82 [30] and 0.34 [37] eV, respectively, for I and V type defects).

In conclusion, our investigations of the evolution of the dopant-damage systems, during a sub-μs LI in the partial melting case, demonstrate that the defects' role in the dopant activation is essential. Upon increasing the laser fluence and the pulse numbers, comparable point defect supersaturations were found in the solid regions, despite a reduction in the number of clustered defects. This scenario suggests that only clustered defects limit the activation in the low and medium dopant density regimes, trapping the dopant atoms and preventing them from reaching a substitutional position. The main result of the present work is that we have obtained a reliable model and, at the same time, a deeper understanding of dopant activation in implanted silicon under laser annealing. The *inclusion of full defect-dopant interactions in the simulation code proves that post-implantation defect clusters rule the dopant evolution, thus limiting the activation in the dopant peak region.* The experimental setting of our research (in particular the relatively low dose and large energy of the implantation) has been conveniently tuned in order to avoid possible amorphization due to the implant and P clustering, which leads to an inactive dopant, and to allow the study of both partial melting and total melting conditions in the same samples.

The results presented in this paragraph deal with dopant evolution in solid phase. Similarly, the understanding of dopant evolution in the melting phase has many open questions. In the following section we will deal with one of the most intriguing cases, which does not have a clear explanation until now. A new model will be proposed and a comparison of the obtained results with experimental data will be shown.

3.4. Dopant evolution in melting phase

In the present section, the evolution of implanted dopant atoms in silicon at the melting phase will be investigated. In particular we will try to elucidate the dopant pile-up phenomenon. Many experimental works have revealed a dopant (boron or arsenic) pile-up near the maximum melt depth in bulk Si after a laser irradiation process with a deep melting [61]. Our modeling idea comes from the anomalous silicon properties in liquid phase just above the melting temperature. A model for the dopant evolution in the liquid phase has been developed. In subsection 3.4.1, the experimental approach is described, which allows us to follow the dopant evolution in different melting conditions, from shallower to deeper melting processes with respect to the dopant implant projected range, for the case of boron pileup. Afterwards the details of the developed continuum model will be presented. At the end of the section, we will present simulation results and their comparison with the experimental ones. A deep explanation of the boron evolution during the laser process and the B profile pile-up near the maximum melt depth will conclude the chapter.

3.4.1. Experimental approach

LI processes have been performed in an implanted silicon substrate (B 2 keV energy, 3×10^{13} cm^{-2} dose). The samples have been annealed using an EXCICO LTA15 laser ($\lambda = 308$ nm) at room temperature, with a pulse duration of 170 ns. Laser energy densities of 2.0, 2.37, 2.46, 2.64 J/cm^2 have been considered in single pulse configuration. After implantation and/or LI, all of the samples remain mono-crystalline, as verified by transmission electron microscopy. Chemical B profiles have been analyzed by means of secondary ion mass spectroscopy (SIMS). Figure 3.13 shows dopant re-distribution after a laser irradiation process for all the processed samples. The SIMS analysis demonstrates that dopant evolution and its re-distribution in the molten regions can be divided in three different regimes as a function of laser fluence (or the maximum melt depth): an against-gradient regime (green line), where the final dopant distribution appears to be inverted with respect to the as-implanted one with an opposite gradient; a pile-up regime (blue and magenta lines) with a flat distribution except two regions (with a width of $\sim 10-20$ nm) neighboring to the surface and the maximum melt depth, which show a depletion and an increase, respectively, of dopant density with respect to the flat constant value; a no-pile-up regime (red line) characterized by an almost flat distribution and a sharp decrease at the maximum melt depth.

Here we try to achieve a suitable theoretical description that is valid

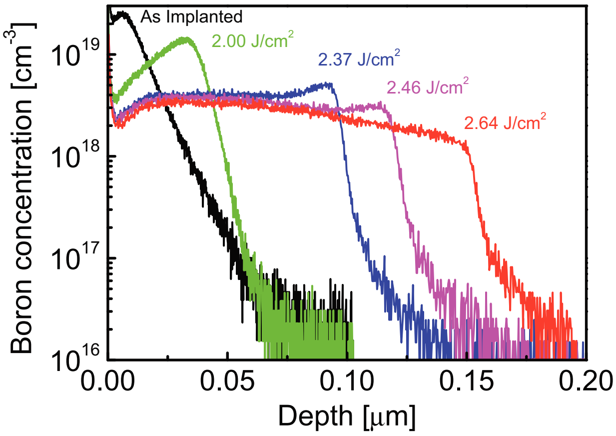

Figure 3.13.: Experimental chemical P profile of an implanted silicon substrate (B 2 keV energy, $3{\times}10^{13}$ cm^{-2} dose) from SIMS Analysis as a depth function after one laser irradiation pulse. The data shown refer to LI with laser fluences 2.00 (green), 2.37 (blue), 2.46 (magenta) and 2.64 (red) J/cm^2. The dark line refers to chemical P as-implanted profile.

for all of the process conditions evidenced.

3.4.2. Continuum model

Heat diffusion and melting in an irradiated Si sample is simulated by means of a phase-field approach. In the present investigation, differently from the Karma formulation employed in subsection 2.4.1, we chose to implement the Wheeler phase-field approach [104], which allows us to account for solute trapping effects during solidification in melting process (see Appendix C for a detailed description). In the numerical simulations phase Φ ($0 \leq \Phi \leq 1$ with $\Phi = 1$ and $\Phi = 0$ for the pure solid and liquid phases, respectively) and temperature T, evolve according to the following coupled differential equations [49, 50]:

$$\frac{\partial \Phi}{\partial t} = D_{\Phi}\nabla^{2}\Phi - \frac{2D_{\Phi}}{l^{2}}\left\{\Phi\left[1-\Phi\right]\left[0.5+\beta-\Phi\right]\right\} \tag{3.11}$$

$$\rho c_{s}\frac{\partial T}{\partial t} + 6L\Phi\left(1-\Phi\right)\frac{\partial \Phi}{\partial t} = \nabla k \nabla T + S\left(\mathbf{r},t\right). \tag{3.12}$$

In these equations, l is the interface thickness, L is the latent heat, ρ the density, c_s the specific heat, D_{Φ} the phase field diffusivity and k the thermal conductivity. $\beta = \beta(T)$ is related to the liquid-solid interface speed as a function of T [49, 50]. The phase field diffusivity depends on the interface thickness and the characteristic time of attachment of atoms at the interface t_c (i.e. $D_{\Phi} = l^{2}/\ t_c$) [41]. All the parameters, except l, are local and can depend on the other field according to suitable interpolation laws (e.g. k depends on phase and T). Parameter calibration of the phase-field methodology is discussed in Ref. [49]. The absorbed heat source is $S(x,\ t){=}E_{\mathrm{las}}P(t)(1\ {-}R)a\exp({-}ax)$, where E_{las} is the incident laser energy, $P(t)$ is the normalized laser pulse shape, and R and a are the phase and temperature dependent surface reflectivity and the material absorption at the laser wavelength, respectively.

The phase-field methodology is especially suited for studying this problem since it deals consistently with the non-equilibrium segregation and curved melting front evolution. In order to simulate the dopant evolution in the liquid phase, we have assumed that B atoms can coexist in two different states, one highly mobile (diffused) than the other, where the temperature in the molten region rules the corresponding concentrations by means of a balance equation. In particular, dopant atoms in the lower diffusion state reside in regions with a temperature range just above the melting point of Si ($\sim$ 9 K higher that the silicon melting point, i.e. neighbor to the maximum melt depth), whilst atoms in the higher diffusion state are in the remaining liquid regions (in this case they move with the known dopant diffusivity in liquid phase $\sim 2.4 \cdot 10^{-4}$ [cm^2/S] [45]). The dopant evolution is ruled by rate equations of the following form:

$$\frac{\partial C_B^{HD}}{\partial t} = \nabla D_{\mathrm{B}}^{HD} \nabla C_B^{HD} - \ln\left(K_0^B\right) \nabla \left[D_B^{HD} C_B^{HD} \left(1 - C_B^{HD}\right) \Phi \left(1 - \Phi\right) \nabla \Phi\right] + R \tag{3.13}$$

$$\frac{\partial C_B^{LD}}{\partial t} = \nabla D_{\mathrm{B}}^{LD} \nabla C_B^{LD} - \ln\left(K_0^B\right) \nabla \left[D_B^{LD} C_B^{LD} \left(1 - C_B^{LD}\right) \Phi \left(1 - \Phi\right) \nabla \Phi\right] - R \tag{3.14}$$

$$R = -k^f \left(C_B^{LD} - k^b \cdot C_B^{HD}\right). \tag{3.15}$$

where D_{B}^{HD} and D_{B}^{LD} are the diffusivity of boron atoms in the higher and lower diffusion state in liquid phase, taking the same value in solid phase. C_B^{HD} and C_B^{LD} are the corresponding concentrations. K_0^B is the equilibrium segregation coefficients. k^f and k^b are the forward and backward reaction rates. The first is a fixed constant (not null only in the melting phase) whilst the second follows a gaussian law as function of T (centered on the silicon melting temperature T_M) in liquid phase:

$$k^b = k_{T_M}^b \exp\left(\frac{-\left(T - T_M\right)^2}{\sigma^2}\right), \tag{3.16}$$

k_b takes the constant value $k_{T_M}^b$ in the solid phase.

3.4.3. Results and discussion

In this section we will discuss our simulation results and their comparison with the experimental data. The designed experiment allows us to

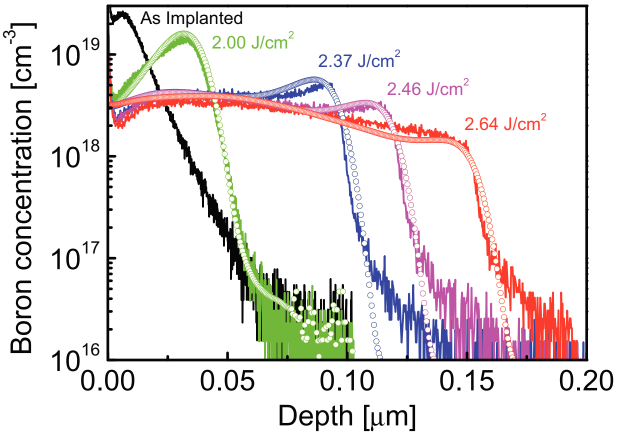

Figure 3.14.: Chemical B profile of an implanted silicon substrate (B 2 keV energy, 3×10^{13} cm^{-2}dose) from SIMS Analysis (solid line) and simulated (open circles) as a depth function after one laser irradiation pulse. The data shown refer to LI with laser fluences 2.00 (green), 2.37 (blue), 2.46 (magenta) and 2.64 (red) J/cm^2. The dark line refers to chemical P as-implanted profile.

follow the dopant evolution in different melting conditions varying the laser density energy, from shallower melting processes to deeper ones with respect to the dopant implant projected range. Figure 3.14 shows our simulation results. Open circles represent the simulated B dopant re-distribution after one pulse laser irradiations for all the processed samples. A satisfying agreement can be found for the against-gradient, pile-up and no-pile-up regime. The calibration work gives the value of $k^f = 10^9$[s^{-1}] for the forward reaction rate, and 200.0 and 9 [K] for the constant exponential prefactor $k^b_{T_M}$ and the variance σ of the gaussian backward reaction rate k^b. The boron diffusion in the high diffusion state in liquid phase is found to be 2.4×10^{-4}[cm^2/s], according the work of Kodera [45]. In order to clarify the boron pileup mechanism in the silicon melting phase during a laser irradiation process, snapshots of the dopant evolution have been reported in Figure 3.15 for the case of 2.37 J/cm^{2}laser fluence.

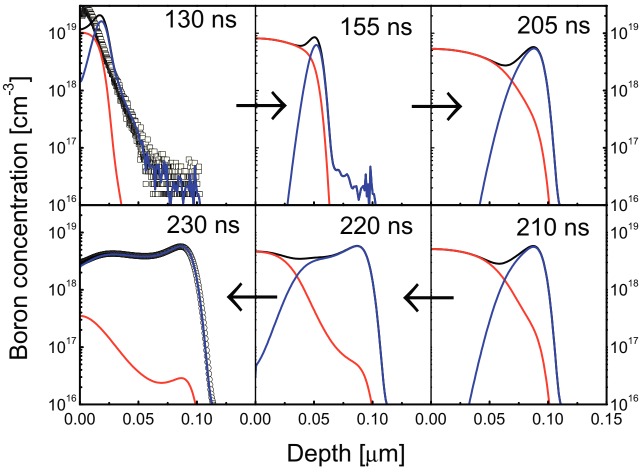

Figure 3.15.: Snapshots of the dopant evolution in the silicon melting phase during the laser irradiation process (2.37 J/cm^2). The upper panels refer to the melting process whilst the lower to the crystalline silicon re-growth. Dark, red and blue lines refer, respectively, to the total boron concentration and its two components (with higher and lower mobility). The as-implanted (empty squares) and the final (empty circles) SIMS distributions are also shown. The laser process reaches a maximum melt depth of 0.13 μm at 205 ns.

Upper panels refer to the melting process whilst the lower to the crystalline silicon re-growth. Dark, red and blue lines refer, respectively, to the total boron concentration and its two components (with higher and lower mobility). The as-implanted (empty squares) and the final (empty circles) SIMS distributions are also shown for completeness. The laser process reaches a maximum melt depth of 0.13 μm at 205 ns. During a melting irradiation, boron atoms can be in two different states with different mobilities. In particular, dopant atoms in the lower diffusion state reside in regions with a temperature range just above the melting point of Si ($\sim$ 9 K higher than the silicon melting point, i.e. neighbor to the maximum melt depth), whilst atoms in the higher diffusion state characterize the impurity kinetics in the remaining liquid regions (in this case they move with the known dopant diffusivity in liquid phase $\sim 2.4 \cdot 10^{-4}$ [cm^2/S] [45]).

This twofold possibility has different effects depending on the initial dopant distribution and the maximum melt depth of the process with respect to the implant dopant projected range. For a laser irradiation with a maximum melt depth greater than the dopant region, the initial distribution is shifted during the melting process towards the bulk region (upper panels of Figure 3.15, blue lines) due to the gradient of the distribution of the higher diffusivity impurities (red lines). As a consequence impurity atoms can move from left to left, being in a *trapped lower-diffusivity region* near the moving melt depth. During the silicon re-growth (lower panels of Figure 3.15), a re-distribution follows in the flat region due to the movement of high diffusivity atoms near the surface (red lines).

Depending on the laser fluence, i.e. on the maximum melt depth of the process, tree different final distributions can be achieved as shown in Figure 3.14: an against-gradient regime (green line), where the final dopant distribution appears to be specular to the as-implanted one with an opposite gradient; a pile-up regime (blue and magenta lines) with a flat distribution except two regions (with a width of ˜ 10-20 nm) neighboring to the surface and the maximum melt depth, which shows a depletion and an increase, respectively, of dopant density with respect to the flat constant value; a no-pile-up regime (red line) characterized by an almost flat distribution and a sharp decrease at the maximum melt depth. The two state diffusivity model reproduces carefully all the regimes. It has to be stressed that a model which considers only one diffusion state (with the known dopant diffusivity in liquid silicon) cannot reproduce the experimental scenario. In fact, due to the high dopant diffusivity in liquid Si, which is about eight orders higher than that in solid Si [45] and the near unity segregation coefficient [75, 107], a laser melting process produces a boxlike profile after a liquid-phase epitaxial recrystallization of the melted region. After reaching a zero gradient distribution during the melting, dopant atoms cannot evolve towards pile-up configurations. With the two state model, it is possible to invert the gradient of an initial dopant distribution.

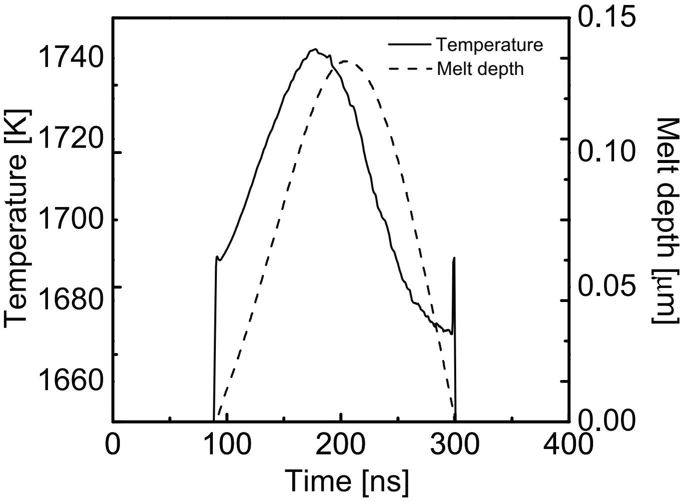

Figure 3.16.: Time evolution of the temperature at the irradiated surface (solid line) and the melt depth (dash line) during the laser irradiation with an energy density of 2.37 J/cm^2.

An evolution of dopant profile is observed only from 130 ns to 230 ns, whilst the melting process starts at 90 ns finishing at 300 ns. It can be explained looking at Figure 3.16. It shows the time evolution of the temperature at the irradiated surface (solid line) and the melt depth (dash line) during the laser irradiation (2.37 J/cm^2). We can see that temperature above 1700 K lies in the time range from 130 ns to 230 ns. On the other side, according to our model, dopant atoms reach the high diffusivity state only in regions which have a temperature of 9 K degrees higher than the silicon melting point (1690 K).

When the laser fluence is fixed and the sample is processed with multi pulse irradiation, a dopant accumulation near the maximum melt depth is experimentally observed [62]. Our model reproduces also this phenomenon. Figure 3.17 shows simulation results about dopant re-distribution in the melting phase in an implanted silicon substrate (B 2 keV energy, 3×10^{13} cm^{-2}dose) after multi pulse laser irradiation. The data refer to LI with laser fluences of 3.00 J/cm^{2}and after a number of pulses indicated (from 1 to 3). The dark line refers to chemical P as-implanted profile obtained by SIMS analysis.

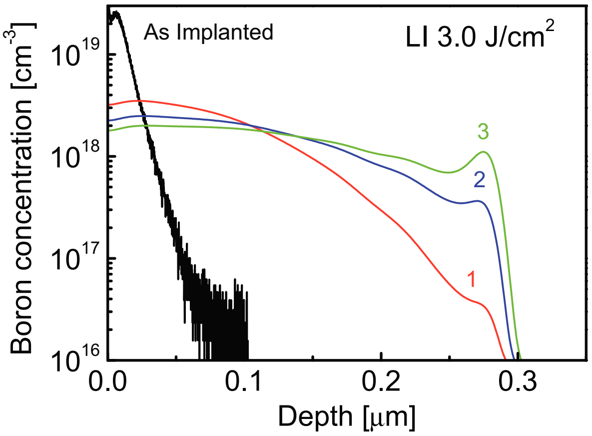

Figure 3.17.: Simulated dopant re-distribution in the melting phase in an implanted silicon substrate (B 2 keV energy, 3×10^{13} cm^{-2}dose) after multi pulse laser irradiation. The data shown refer to LI with laser fluences of 3.00 J/cm^{2}and after the number of pulses indicated (from 1 to 3). The dark line refers to chemical P as-implanted profile obtained by SIMS analysis.

In conclusion, in this section the evolution of implant dopant atoms in silicon melting phase have been investigated. We elucidate the mechanism which is at the basis of the dopant pile-up phenomenon for the case of boron on silicon. The developed idea come from the anomalous silicon properties in liquid phase just above the melting temperature. The experimental approach allowed us to follow the dopant evolution in different melting conditions, from shallower to deeper melting processes with respect to the dopant implant projected range, for the case of boron pileup. The two state diffusivity model for the dopant evolution in the liquid phase reproduces the experimental data for all regimes obtained by varying the laser fluence. Also the multi pulse trend, experimentally observed in other works, can be reproduced.

3.5. Future prospects

Concerning the dopant solid activation study, our investigations of the evolution of the dopant-damage systems, during a sub-μs LI in the partial melting case, demonstrate that the defects' role in the dopant activation is essential. Studies with a much higher dopant concentration (higher implant dose) and a shallower implant can extend and confirm the described physical scenario. However, the modeling (and the related understanding) must be further extended in order to simulate the role of the amorphous phase [49, 50], dopant-dopant coupling [96], and small clusters' effective migration [47, 48].

Continuum models have the advantage to be easily implemented in commercial simulation tools. This allows a quick setting of the problem. Part of introduced parameters come from fundamental ab-initio calculations, other from experimental measurements and other from fitting works. As a consequence their advantages have a cost in terms of "customized" parameter calibration. Another disadvantage arises from the maximum number of coupled equations which can be implemented due to computational memory and time cost. Part of there limitations can be overcome tackling the problem with a Kinetic Monte Carlo (KMC) approach. In this way, there are no limitations in the number of interactions between dopant atoms and defects. A detailed dopant clustering can be considered as well as a dopant-defect cluster complex (in an explicit way than the one used until now). At the same time, a great part of the parameter can directly derived from fundamental simulation works. A more realistic defect-dopant system evolution can be obtained, from the implantation process to the laser annealing one, passing from the room temperature within the same code. All these issues will be dealt in the next chapter, where KMC results will be compared to the continuum ones shown below.

Focusing on the dopant liquid phase evolution, we have to test the model on multi pulse laser irradiation processes. It can provide an additional confirmation, which will put our findings in a central position for future research on this interesting area. New atomistic investigation, along the direction we proposed, can furthermore support the presented model and, concurrently, suggest new point of view.

4. Kinetic Monte Carlo simulations of laser irradiation processes

4.1. Overview

In the present chapter we will describe in detail our approach to simulate laser irradiation processes of dopant implanted semiconductors with Kinetic Monte Carlo (KMC) techniques.

Preliminarily, the state-of-the-art of Monte Carlo approaches for constant temperature annealing will be presented. Afterwards, the motivations for the development of a KMC code, coupled to the phase-field model, and the advancements achieved in the model features with respect to the conventional constant temperature code will be discussed.

In particular, we will provide a detailed description of the thermal problem, related to the space and time dependent temperature field in a laser irradiated substrate, and the issues that this brings to the KMC code development. A entire section will be devoted to the code special features, the particular link with continuum simulation of the thermal evolution (temperature and phase fields) and parameter calibration. Finally, results and discussion, with remarks on the innovation of the methods (regarding laser irradiation process simulation), will conclude the chapter.

4.2. Introduction

Simulations of laser processes are crucial in order to understand the effects of irradiation on material modification both in melting and solid phase. Indeed, many issues are nowadays poorly understood also for the widely investigated case of LTA of implanted silicon. For instance, the behavior of common dopant atoms (arsenic and boron) and their evolution in the melting phase or the dopant activation promoted by laser irradiation process. These issues can be studied by means of various simulation approaches.

Continuum models, formed by a set of coupled Partial Differential Equations (PDE model), allow for an accurate determination of thermal fields and melting evolution by means of the phase-field methodology [41, 49, 50]. Moreover, a set of coupled diffusion-reaction equations can simulate the evolution of the dopant-defects system during the annealing process [25, 26, 37, 53]. The entire physics of the system is formulated as a set of differential equations ruling the density field kinetics of each particle considered to be relevant in the process. This technique has the advantages to be easily implemented in commercial simulation tool with a quick setting of the problem. Moreover, in general, the simulation time is short and large systems can be studied by adjusting the grid used for the spatial discretization of the equations. At the same time, in comparison to more fundamental approaches, a large number of model parameters have to be calibrated and, due to the intrinsic approximations, some of these parameters have not a clear physical counterpart (ad hoc calibration). Part of these parameters can be derived by ab-initio calculations, other by experimental measurements and other by fitting procedures. As a consequence, the cost of fast execution is paid in terms of parameter calibration. Other disadvantages arise from the maximum number of coupled equations that can be implemented due to computational memory and time cost.

Most of these limitations can be overcome tackling the problem with a Kinetic Monte Carlo (KMC) approach. In this way, there are no limitations in the number of interactions between dopant atoms and defects. A detailed dopant clustering can be considered as well as dopant-defect cluster complexes (in a explicit way than done until now). The kinetics is simulated by a sequence of “virtual” events associated one to one to “real” events. At the same time, consistently, great part of the parameters can be directly extracted from atomistic calculations.

We have developed an innovative KMC code, which rules the post-implant kinetics of the defects-dopant system in the extremely far-from-the equilibrium conditions caused by the laser irradiation both in the non-melting, melting and partial melting regimes. It considers defect diffusion, annihilation and clustering.

The reduction of the implantation damage and its reorganization in defect aggregates are studied as a function of the process conditions. As a first test, a PDE model (as described on subsection 2.4.2) and a KMC code have been implemented for the same laser annealing processes in an implanted silicon substrate (200 keV and a dose of 10^{14} cm^{-2}, subsection 2.6.2). Results predict similar damage reduction after room temperature evolution. Discrepancies can be found at the nanosecond scale, during laser irradiation, where the intrinsic difference between the two simulation techniques play a crucial role in the time evolution.

In the following the KMC approach will be described in detail. The code reflects the second module of the continuum model (see subsection 2.4.2 for details) and, as it has been done for that, it is coupled with the first module PDE results for the thermal field and melt depth evolution.

4.3. Kinetic Monte Carlo approach

A Kinetic Monte Carlo code simulates the dynamics of the system using a particle-like description. Therefore, this method allows to simulate the material modification in the device structures at a macroscopic scale with a microscopic resolution, computing the phenomenon evolution in a nearly natural way. From this side, a KMC simulation appears like a virtual reproduction of the real physical evolution events. Our code belongs to the class of the non-lattice KMC models, where atoms present in the perfect lattice are not explicitly simulated. Consequently, system sizes of hundreds of nanometers can be treated using computers with average performances.

Generally, in a KMC simulator, the program computes a sequential selection of randomly picked events. The event probabilities act as a weight in the random selection procedure. At the same time, the inverse of the total sum of event probabilities updates the simulation time. The generic reactions, such as A + B $\leftrightarrow$ C , are modeled by performing interactions (forward reaction) and dissociation events (reverse reaction). When particles A and B are within the capture volume of each other they interact leading to the formation of C. On the other hand, the probability of particle C breaking-up is controlled by its own event rate. Other type of events are, for example, the diffusive hops of mobile species (diffusion is simulated by a sequence of random jumps), or the emissions of point defects from clusters.

Both interactions and dissociation events are determined by several parameters (capture volumes, activation and migration energies, etc.) whose values must be defined a-priori. Usually, all events simulated in KMC are thermally activated processes. Their probabilities are always related to an activation energy barrier E^{act}, and follow a Boltzmann distribution. Therefore, the frequency (or probability per unit time) at which a particular event i takes place can be expressed as,

$$v_i = \frac{1}{\tau_i} = v_i^0 \exp\left(\frac{-E_i^{act}}{k_B \cdot T}\right), \tag{4.1}$$

where v_i^0 is the pre-factor, k_B the Boltzmann constant and T the temperature. In a system with N_i particles, which can undergo the event i, the total event rate is

$$R = \sum N_i v_i. \tag{4.2}$$

After a random selection process, the selected atom performs a jump in a random direction in order to simulate diffusion or emission of mobile species from clusters. If the moved particle has neighbor ones to interact with in its new position, an interaction is performed. Event rates must be updated and the simulation time is increased by an amount $t = 1/R$. Since the event probabilities usually follow an Arrhenius-type law, large variations between the rates associated to different events may occurs. In a simulation run, the most likely event sets the time update. Generally the fast events tend to disappear quickly leaving slower events that allow raising the time-step. For simulation of defect evolution, diffusive events are more likely than the dissolution of a stable cluster emitting the point defect component. An advantage of KMC methods is the possibility to introduce new reactions without increasing of the computational efforts, since it only requires new event rates to be added to the total event rate. The main difficulty arises from the determination of the new parameters (binding energies, diffusivities, capture radius) that describe the interactions. These parameters are also necessary in continuum methods, but in the latter case new interactions imply in addition a larger number of coupled equations which complicates their numerical resolution.

Many kinds of KMC codes have been developed in the past years to study the evolution of a dopant-defect system in implanted semiconductors during a constant temperature annealing. The process features allow to fix all the event frequencies. Hence standard selection algorithms can be implement. These algorithms cannot be applied for a Kinetic Monte Carlo simulation of the laser annealing process. In this case, differently from constant temperature process, the space and time dependent temperature implies also the space and time dependence of all the frequencies involved. An evolution and a change of the thermal field requires an update of all the frequencies associated at all the possible events. This particularity requires the introduction of a different and more efficient sampling method.

The use of a *tree* algorithm can overcome these difficulties. In each simulation run, a particle is picked and the time is updated by the total event rate R. In this way there are not any vain loops. In our case, we are looking for a data storage tool which can easily store elements and select quickly them by means of an efficient stochastic procedure. An array or a linked list (a data structure which allows us to store lists of arbitrary length and to quickly insert o delete elements respect to the array) are efficient for certain types of task. However, these simplified storage methods are not suitable to compute the random selection in our code. The array cannot add or remove elements efficiently, and the linked list cannot read quickly a specified value without having to

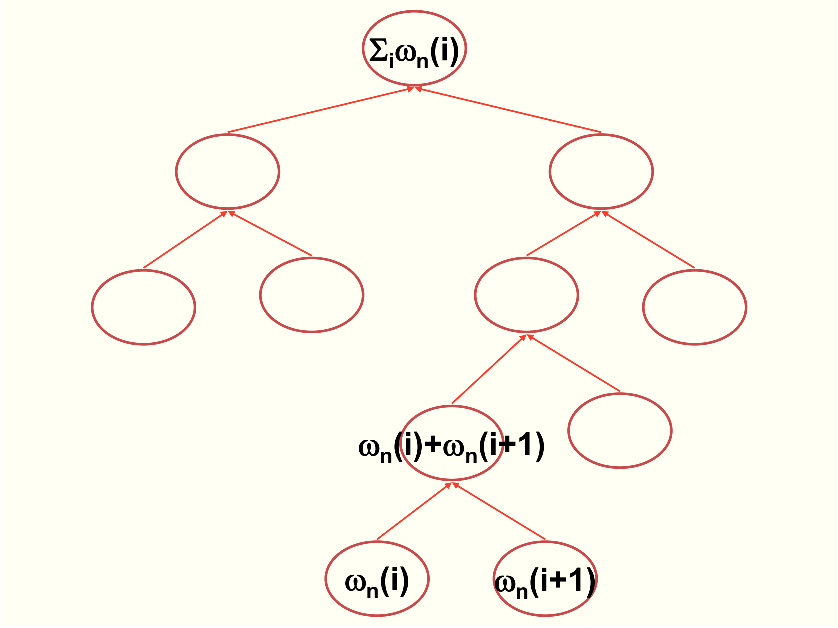

Figure 4.1.: The tree binary structure.

run through all the preceding elements. A tree can partially overcome both this drawbacks. A tree is similar to a linked list in being made up of element and pointers, but each element or node can be accompanied by more than one pointer. The most common type of tree is the *binary tree* in which each node has two pointers to other children nodes. Figure 4.1 shows the tree structure for this binary case. The *root* node $\Sigma_i\omega_n$ (i) is that at the very beginning of the tree and the nodes at the very end are called *leaves*. During a random selection process, a random number between 0 and 1 allows us to choose one of the two children of a parent node. Hence starting from the tree root, a loop allows us to reach a leave at the end of the tree. This random selection process picks events weighing them by means of their own probability. The number of steps needed to complete this selection is proportional to the logarithm (base 2 in the case of a binary three) of the number of events stored in the tree. Therefore, it is more efficient with respect to the simple array structure. The tree root, being the sum of all the event probability, i.e. the total event rate R of Equation 4.2, is used to update the time interval between two successive KMC steps.

4.3.1. KMC code for the defect system in silicon

The non-lattice KMC code extends the capabilities of the second module of the PDE model for the defect evolution discussed in subsection 2.4.2. Particles are free to move inside the simulation box ($X_b \times Y_b \times Z_b$ nm) without lattice restrictions. I and V point defects are the unique mobile species and defect clusters X_n can only absorb/emit point defects. Therefore, in order to reproduce the defect system evolution as a function of the time, diffusion events for point defects and dissolution events for clusters has been considered with Arrhenius-like probabilities. In order to select an event and update the simulation time, a Monte Carlo selection tree was constructed, where all the probabilities associated to all the possible events have been stored in the tree leaves. Within this approach, the generation of random numbers sequence picks random events and the tree root, which represent the sum of all the possible event probabilities, allows for the time update. The following point defect I-V and point defect-cluster interactions (described in detail on section 2.3) have been implemented:

$$I + V \Longleftrightarrow 0 \tag{4.3}$$

$$X + X_{n-1} \Longleftrightarrow X_n \tag{4.4}$$

$$I_n + V \Longleftrightarrow I_{n-1} \tag{4.5}$$

$$V_n + I \Longleftrightarrow V_{n-1}, \tag{4.6}$$

where an I or V annihilation has been considered when a mobile defect falls inside the capture radius of another point or clustered defect.

Since our experimental results refer to blanket (i. e. one dimensional) samples, periodic conditions for the diffusion events and particle interactions have been set in directions orthogonal to the depth. Annihilation conditions have been fixed at the irradiated surface to introduce the physical effect of mobile point defect dissolution at the sample surface. Reflective conditions have been set on the opposite side (to the surface) in order to reproduce with a good approximation the real bulk behavior. This assumption is as correct as large is the simulation box Z_b length with respect to the dimension of the defect evolution region. The latter region is fixed by the initial conditions as well as the annealing process (temperature and duration) conditions.

In order to compare KMC and continuum model results, point defect and cluster parameters both for I-type and V-type defects were taken equal (see Table 2.1 and Table 2.2). In particular, for diffusive events, the same migration energy has been fixed whilst the D_0 exponential pre-factor was switched to the event frequency by means of the relation

$$f = \frac{6D_0}{\lambda^2}, \tag{4.7}$$

where λ is the jump distance to second nearest-neighbor (fixed equal to r_{capt}).

Concerning the cluster dissolution events, the same dissolution energies have been implemented (Table 2.2) and a probability pre-factor equal to diffusive one (distinguishing for I or V defect) multiplied by the cluster size has been chosen. As a consequence cluster dissolution probability increases linearly with the cluster size, but decreases as a function of the dissolution energy. No restriction has been made for the cluster sizes, but clusters formed by more than 10 particles have the same dissociation energy and capture radius (fixed equal to bigger cluster values in the PDE model). This choice is taken in order to match as close as possible the cluster reduced model implemented in the continuum approach.

The defect system has been initialized with the same SRIM BCA data as done for the continuum room temperature model. Blue dashed (I-type defects) and dotted (V-type defects) lines of Figure 2.8 refer to the residual defect density after room temperature evolution obtained by the KMC code, showing a reduction of 40 % of the total implant damage, as it was found with the continuum PDE model (red lines). Therefore, post-implantation damage is stored in small defect aggregates [38] corresponding to a space dependent cluster size distribution of I and V type aggregates. This is shown in Figure 4.4, where lines from green (top) to blue (bottom) refer to cluster density with increasing size formed by 2 to 10 particles.

4.3.2. Coupling between KMC and continuum field

In the last two decades, simulation codes have been developed by different research teams to study the evolution of a dopant-defect system in implanted semiconductors during a constant temperature annealing. These process conditions allow to assume that all the event frequencies v_i are fixed. During a laser irradiation the temperature dependent frequencies $v_i\left[T\left(x,t\right)\right]$ vary with time and space in all the simulated samples. As a consequence, we have to develop a code which considers the possibility of field-like event probabilities expressed by suitable local functions of $T\left(x,t\right)$. In addition, we have to implement the laser source in order to reproduce the thermal and phase fields during the annealing. We have chosen to couple the simulation results obtained with the continuum model for the thermal evolution of subsection 2.4.1 with the KMC code. The technical innovation of our code lies in the extension of the KMC method to face the evolution problem of the dopant-defect system in silicon in a space and time-dependent thermal field on the sub-microsecond scale. In the following, details of the coupled process will be discussed.

Once a particular laser process has been simulated with the phase field model, the maximum melt depth evolution (Figure 2.7) for the whole process and the temperature field as a function of the time (Figure 2.4) in the processed region are extracted and stored at constant intervals with a given time resolution. This choice of δt is a fundamental point and is related with the time variation of the event frequencies by the temperature gradient

$$\frac{\delta R}{R} \backsimeq \frac{E^{act}_{Max}}{k_B \cdot T^2} \cdot \delta T, \tag{4.8}$$

where E^{act}_{Max} is the largest activation energy involved in the event frequencies of the process. Equation 4.8 has been derived from Equation 4.2 and Equation 4.1. For instance, for our defect parameter setting $E^{act}_{Max} = E^{8}_{diss} = 4.22$ eV, i.e. the dissociation energy of I_8 (see Table 2.2). Therefore a temperature variations of $\sim$ 10 K at room temperature leads to a total R variation of $\sim 5.4\,\%$, whilst at higher temperature, e. g. $T = 1600$ K, the total R variation is $\sim 2.0\,\%$.

After the extraction of temperature fields as a function of time at different points (equally spaced), a linear interpolation allows to calculate the temperature for the particles occupying a given position and the related frequency can be properly updated. During a KMC simulation, the time evolves according to $1/R$, so we have to fix the time interval δt after the update of all the frequencies (i.e. the tree leaves) which are considered constant until another time interval δt passes. Concurrently, by means of the maximum melt depth curve, all the particles that during their evolution fall inside the melted layer are fully annihilated. Considering the laser pulse shape (Figure 2.3) and analyzing the simulation output (Figure 2.4 for instance), for all the laser process considered in the following, a value of $\delta t = 0.5$ ns ensures temperature variations lower than 10 K with a consequent acceptable variation of the total R.

4.4. Comparison and links between PDE and KMC approaches

In the present section we will compare results obtained with the two totally different simulation approaches for systems which are equivalent to the one investigated in chapter 2. In particular, we will show

how of a defect system evolves in an implanted silicon substrate under a standard constant temperature field, and subsequently, under a laser irradiation process. All the tests are performed for equivalent processes. Moreover, the same defect parameter calibration has been chosen considering the two different problem formulations corresponding to the PDE and KMC approaches (see subsection 4.3.1 for the parameter details).

4.4.1. Constant temperature process

In order to better understand how the method switching from PDE to KMC affects simulation results, a constant temperature process has been considered. We note that a first check of these issues has been done in subsection 2.6.1 with the study of room temperature evolution of a P implant in silicon with an energy of 200 keV and a dose of 10^{14} cm^{-2}(initial distribution obtained from SRIM). Figure 2.8 shows the results with a good agreement between approaches.

This fact confirms that when the kinetics is dominated only by diffusion and trapping, both methodologies converge towards equivalent predictions. In fact at room temperature, cluster dissolution events do not take place due to their very low probabilities. As a consequence, a more complete analysis has to involve simulations of higher temperature processes where cluster dissolution can occur in reasonable time. A comparison of cluster dissolution time can provide a reliable test for the backward reaction rate in the cluster master equations. In particular, the evolution of two different systems at the temperature of 1000 K has been investigated: a) I and V due to a P implant in silicon with an energy of 200 keV and a dose of 10^{14} cm^{-2} (initial distribution obtained from SRIM); b) only the I part of the previous implant without vacancy defects. In both simulations a computational box of 1 μm length has been considered and a null flux has been set for the domain boundaries.

Figure 4.2 shows the comparison between simulation results obtained with the PDE (dark) and KMC (red) simulations for the first I-V system. Total interstitial (dash) and vacancy (dot) evolution is reported. A good agreement can be seen for the defect dissolution

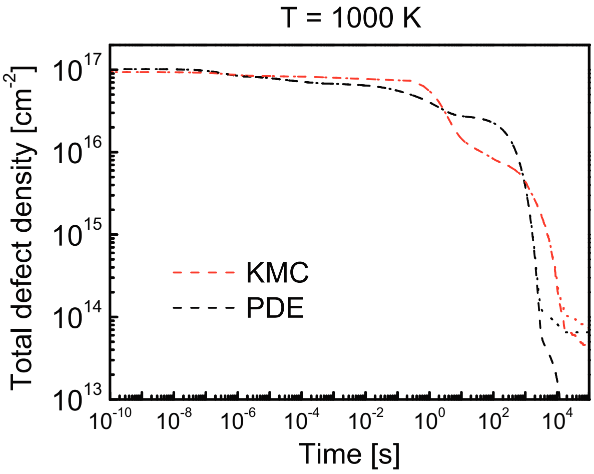

Figure 4.2.: Total interstitial (dash) and vacancy (dot) evolution in a single implanted silicon substrate (P 200 keV and a dose of 10^{14} cm^{-2}) at T = 1000 K as obtained with the KMC (red) and PDE (dark) approaches.

times ($\sim 10^3 - 10^4$ s). Note that, for both approaches, the I and V distributions are always superimposed due to the fast rates of the (point)defect-defect or defect-cluster interactions with respect to the particle diffusion at 1000 K. Looking in detail the evolution of clusters for a fixed size, interstitial clusters disappear at the same time in both approaches whilst the dissolution of small vacancy clusters occurs faster in the KMC simulation with respect to the PDE results; moreover, only bigger clusters ($n > 9$) are present in KMC simulated kinetics for long times.

The pure-I system gives similar results. In this case we have compared results for I cluster evolution in a silicon substrate where the initial I distribution has been similar to the initial I distribution due to a P 200 keV implant with a dose of 10^{14} cm^{-2}. No vacancies have been considered. We have performed this ideal simulation in order to decouple the cluster dissolution effects from those due to the I-V interaction, analyzing the kinetics ruled only by the backward reaction

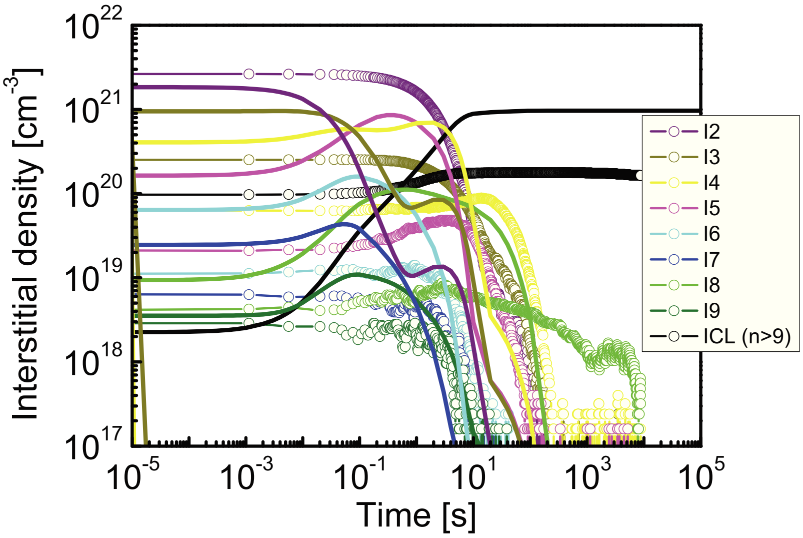

Figure 4.3.: Interstitial cluster evolution in a silicon substrate with only I (initial I distribution takes similar to the initial I distribution due to a P 200 keV implant with a dose of 10^{14} cm^{-2}) at T = 1000 K as obtained with the KMC (open circles) and PDE (solid line) approaches.

rates of the cluster equations.

Similar cluster dissolution times can be seen during the 1000 K evolution as reported in Figure 4.3. In the graph, open circles refer to KMC data and solid lines to the PDE ones. Each colored curve corresponds to the evolution of the total clusters with the reported size.

The reliability of the results here reported demonstrates that the KMC code works properly and that the switching choice of the parameters from PDE to KMC is correct. Once the reliability is demonstrated we can extend the implementation of the KMC code to the more interesting case of the defect evolution under laser irradiation processes.

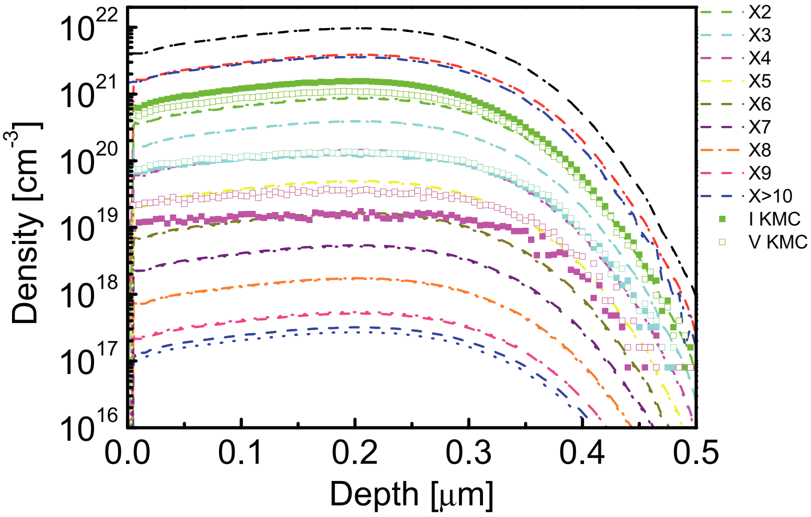

Figure 4.4.: Total interstitial (dash) and vacancy (dot) defect density: dark lines refer to the as implanted defects obtained by the SRIM simulation; red and blue lines refer, respectively, to the residual defect density after room temperature evolution obtained from the PDE model and from the KMC simulation. Lines from green (top) to blue (botton) refer to cluster density with increasing size formed by 2 to 10 particles. Filled (*I*) and empty (*V*) squares refer to KMC simulation results.

4.4.2. Laser annealing process

In order to reproduce a realistic experimental scenario, damage evolution in implanted silicon for three different laser irradiations has been simulated.

We consider the same P single implanted samples described in the section 2.5. As previously reported, it consists of a phosphorus implant in silicon with an energy of 200 keV and a dose of 10^{14} cm^{-2}. Similarly, laser was set having a 308 nm wave length and a profile in the time taken from a real laser irradiation (Figure 2.3). Three laser irradiation processes have been simulated: 2.6 and 3.0 J/cm^2, (partial melting processes: i.e. melt depth lower than the P projected range); 3.6 J/cm^2 (a total melting process i.e. melt depth greater than the P projected range).

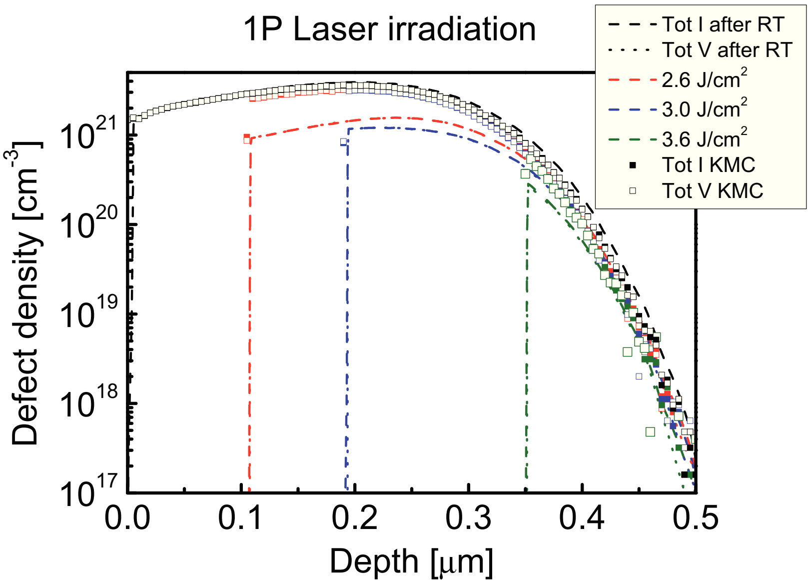

Figure 4.5.: Post anneal total interstitial and vacancy defect density for 2.6 (red), 3.0 (blue) and 3.6 (green) J/cm^2 laser fluences. Dark lines and squares refer to the simulated total interstitial and vacancy defects after room temperature evolution. Dashed (I) and dotted (V) lines refer to the PDE simulation. Filled (I) and empty (V) squares to the KMC data.

In order to simulate laser irradiation processes with the KMC code, as described previously (see subsection 4.3.2 for implementation details), we coupled it with the phase field model for melting and recrystallization. In the coupling strategy applied, phase field PDE results for the thermal field and melt depth evolution have been mapped in the KMC simulation box. In particular, the temperature as a function of the time has been extracted at different positions (every 0.1 μm starting from the irradiated surface) until 1 μm of depth, being

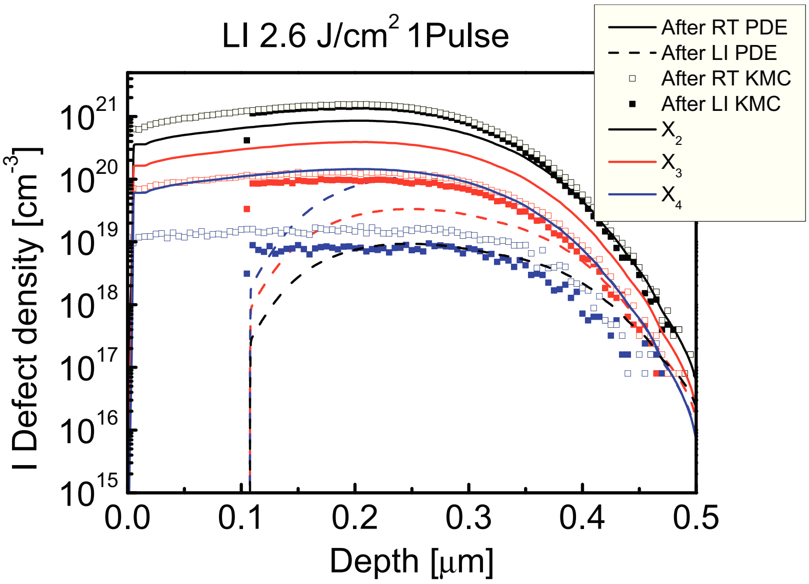

Figure 4.6.: Post anneal interstitial concentrations after room temperature (empty squares) and one pulse laser irradiation (filled squares) for 2.6 J/cm^2 laser fluence. Solid (RT) and dashed lines (LI) refer to the PDE simulation for the same processes. Dark, red and blue lines refer, respectively, to cluster distributions formed by two, three and four defects.

this the Z_b length of KMC simulation box. Figure 2.4 and Figure 2.7 are typical temperature and phase evolution during a melting laser process. During a KMC simulation, an update of melt depth and temperature field at each point takes place, and a linear interpolation allows for the temperature calculation as a depth function.

As discussed in subsection 4.3.2, an update time of 0.5 ns was set, within which the temperature increase is even smaller than 10 K in all the irradiated substrate. This choice prevents changes in the total probability (tree root) smaller than 5%.

Figure 4.5 shows total interstitial and vacancy defect distributions after a laser irradiation process. A substantial difference can be found

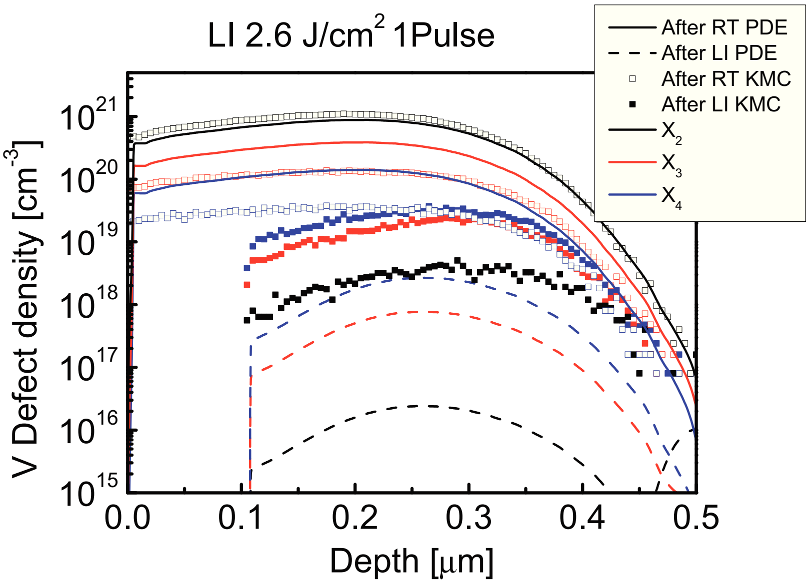

Figure 4.7.: Post anneal vacancy concentrations after room temperature (empty squares) and one pulse laser irradiation (filled squares) for 2.6 J/cm^2 laser fluence. Solid (RT) and dashed lines (LI) refer to the PDE simulation for the same processes. Dark, red and blue lines refer, respectively, to cluster distributions formed by two, three and four defects.

between the continuum model (dash and dot lines) and the KMC results (filled and empty squares). In spite of an excellent agreement about damage decreases after the implant process at room temperature (Figure 4.4) and the dissolution time of defect clusters for constant temperature processes (T = 1000 K), KMC simulations of laser irradiation predict a lower damage reduction with respect to the PDE model. This strong difference can be understood by means of an accurate analysis of the results. Note that, as found for room temperature simulation, I and V distributions, both for PDE and KMC simulations, are always superimposed due to fast rates of the point defect-point defect or point defect-cluster interactions with respect to the particle diffusion. From Figure 4.6 to Figure 4.11 the comparison between interstitial and vacancy small clusters densities after one pulse laser irradiation for three different laser fluences are reported. In particular, clusters formed by 2, 3 and 4 particles have been analyzed. In these cases, the dissolution of V-type defects is faster then I-type one. These results are related to the dissolution energy differences for interstitials and vacancies (Table 2.2).

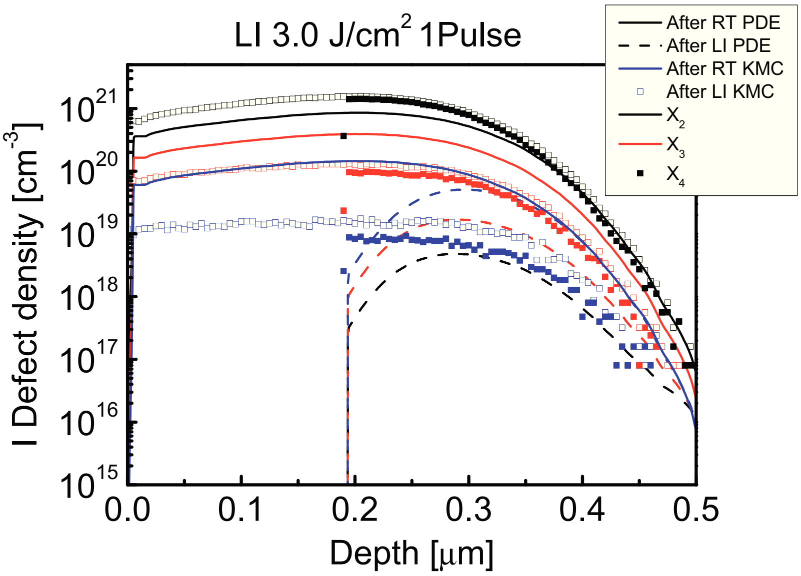

Figure 4.8.: Post anneal interstitial concentrations after room temperature (empty squares) and one pulse laser irradiation (filled squares) for 3.0 J/cm^2 laser fluence. Solid (RT) and dashed lines (LI) refer to the PDE simulation for the same processes. Dark, red and blue lines refer, respectively, to cluster distributions formed by two, three and four defects.

During the KMC simulation of a laser irradiation process, cluster dissolution events dominate the kinetics due to the low number of mobile defects. On the other hand, vacancy clusters will be mainly picked by the random number sequences due to their lower dissolution energy with respect to interstitial clusters. This unbalanced dissolution rate has a double effect: is decreases the population of smaller V-type clusters and increases the population of I-type ones due to the V-I_n interactions. This effect is not evidenced in continuum simulations for the same laser process (dash and dot lines of Figure 4.6 to Figure 4.11). This discrepancy should be related to the adopted form of the backward reaction rate for the cluster dissolution (see Equation 2.15 of subsection 2.4.2) on the cluster reduced model. This formulation correctly predicts the point defect supersaturation evolution for constant temperature processes. It has been shown by Giles and co-workers [30], where point defect supersaturation was indirectly related to the anomalous dopant diffusion. At the same time, we obtained comparable results between KMC and continuum model for constant temperature processes (subsection 4.4.1). Hence the discrepancy found can be related to the nanosecond time scale involved during a laser irradiation process. Nevertheless, the investigation of different formulations for the cluster dissolution backward reaction rate can improve the convergence of the two approaches.

4.5. Conclusion

We would like to summarize the results of this chapter for the different conditions explored: constant room temperature, constant high-temperature and laser induced thermal pulse.

A good agreement has been found between PDE and KMC results for room temperature evolution. In this case only defect aggregation in clusters takes place, due to point defect diffusion, while no cluster dissolution occurs due to the very low dissolution probability.

For constant high temperature process ($T = 1000$ K), both for pure-I and I-V systems, total defect dissolution occurs at comparable times between PDE and KMC. In the system which considers both I and V defects, the dissolution of small vacancy clusters occurs at earlier stages in the KMC simulation with respect to the continuum one.

Laser annealing simulations with PDE and KMC show a substantial discrepancy. It is due to the great difference between I and V dissolution energies (2 eV for the smaller cluster). Therefore during a KMC

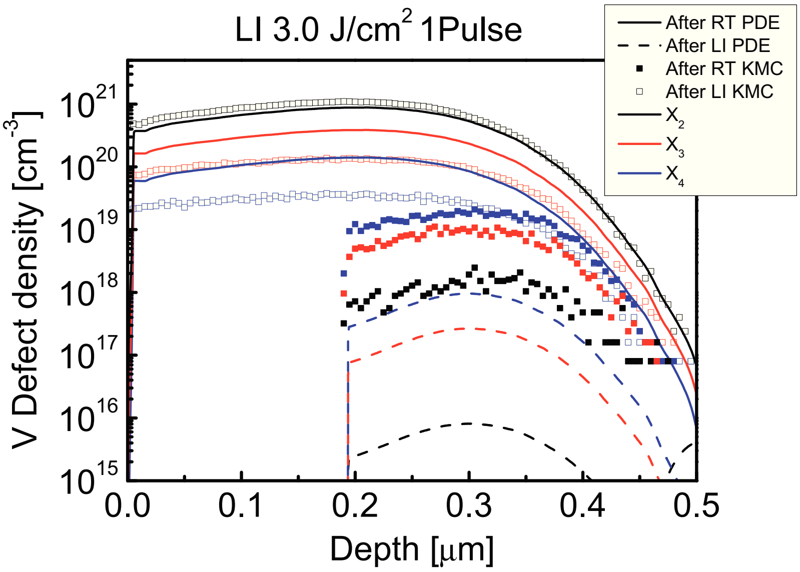

Figure 4.9.: Post anneal vacancy concentrations after room temperature (empty squares) and one pulse laser irradiation (filled squares) for 3.0 J/cm^2 laser fluence. Solid (RT) and dashed lines (LI) refer to the PDE simulation for the same processes. Dark, red and blue lines refer, respectively, to cluster distributions formed by two, three and four defects.

simulation most of the times V-type defects will be picked, increasing V cluster size and decreasing those of I defects. The discrepancy found can be related to the nanosecond time scale kinetics involved in a laser irradiation process. Nevertheless, the investigation of different formulations for the cluster dissolution backward reaction rate can improve the convergence of the two approaches.

We would also like to to emphasize the importance and the innovativeness of the code developed. Past KMC codes of dopant-defect systems in silicon try to investigate constant temperature processes. Hence the involved event frequencies can be considered fixed in time and space. This makes easier the code development. On the other side, laser

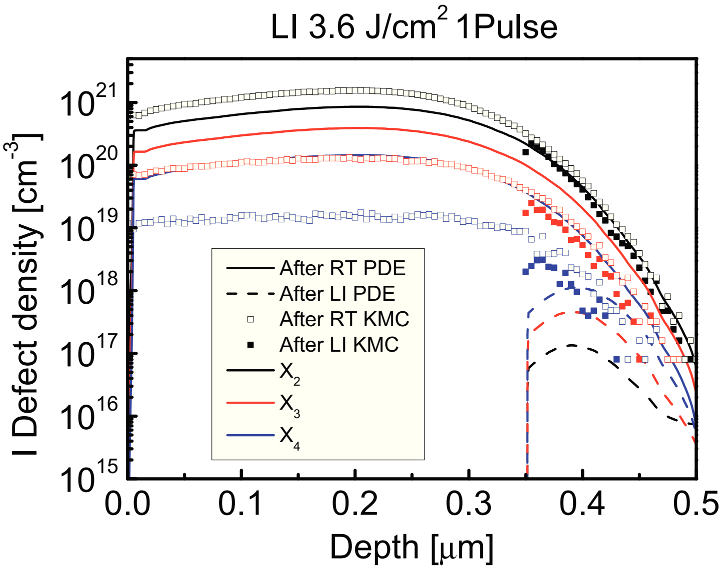

Figure 4.10.: Post anneal interstitial concentrations after room temperature (empty squares) and one pulse laser irradiation (filled squares) for 3.6 J/cm^2 laser fluence. Solid (RT) and dashed lines (LI) refer to the PDE simulation for the same processes. Dark, red and blue lines refer, respectively, to cluster distributions formed by two, three and four defects.

irradiation produces a space and time dependent thermal field. The evolution of the melt depth has to also be taken into account in order to annihilate damage in the molten regions. The main improvements brought by the KMC approach with respect to the continuum model are:

- the introduction without any restrictions of all the dopant-defect reactions governing the kinetics;
- possibility of a direct physical calibration of the parameters which can also be derived by fundamental calculations (ab-initio, molecolar dynamics);
- KMC follows the system evolution from room temperature to

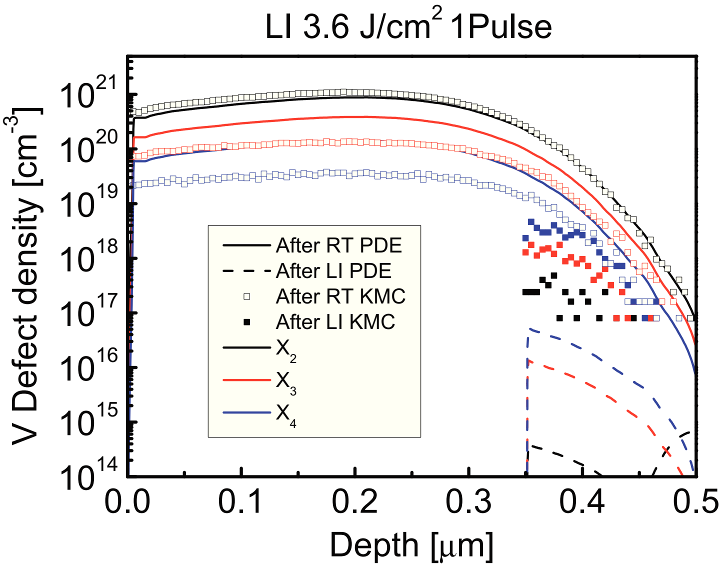

Figure 4.11.: Post anneal interstitial vacancy after room temperature (empty squares) and one pulse pulse laser irradiation (filled squares) for 3.6 J/cm^2 laser fluence. Solid (RT) and dashd lines (LI) refer to PDE simulation for the same processes. Dark, red and blue lines refer, respectively, to cluster distributions formed by two, three and four defects.

the laser annealing process in a more realistic way;

- KMC simulates particle evolution from an atomistic point of view.

Future challenges will consider the study of dopant activation in implanted silicon, as well as in other common semiconductors. Also the investigation of the dopant in the melting phase due to a laser irradiation process will be tackled with this very advanced methodology for the process simulation.

5. Laser annealing of SiGe and Ge based devices

5.1. Overview

In the previous chapters we dealt with dopant redistribution both in liquid and solid phase in implanted substrates under laser thermal annealing. We have investigated these issues from a fundamental point of view in non-patterned structures. However, for application purposes, due to the comparable dimensions of the nano-device periodic structure and the laser wave length, an accurate study of the feasibility of laser irradiation as a heat source for real patterned substrates is needed.

In the present chapter, we will discuss our simulation results concerning the integration of laser annealing in SiGe and Ge based MOS devices. Our implemented simulation code is based on two modules: the former simulates the interaction between the laser light and the transistor structure in order to estimate the heat source. The latter simulates heat diffusion, phase changes and material redistribution under irradiation and it corresponds to the two dimensional case of the approach described in the first chapter. The model is calibrated in the case of different atomic species (namely Si, Ge and common dopant impurities), considering the thermal properties of the materials and the impurity-dependent diffusivity in the solid, liquid and interface region. We present several simulation results obtained by varying materials, implanted impurity profiles and geometry of the Complementary Metal Oxide Semiconductor (CMOS)-like structures. With the support of the simulation results we discuss the possible perspectives of excimer laser annealing applications for the fabrication of post-Si CMOS devices. In particular, we show that by using Ge and SiGe materials the process window for a melting activation process is larger with respect to the case of traditional Si based devices.

5.2. Introduction

Laser Thermal Annealing (LTA) of implanted semiconductor (e.g. Si) samples in the full melting regime has been used to obtain free of defects material with a high electrical activation efficiency and step like junctions [2, 35, 70, and references therein]. The necessary condition for the application of melting LTA in the Metal Oxide Semiconductor Field Effect Transistor (MOSFET) fabrication is the localized melting of the implanted regions only. Of course, the melt depth must overcome the zone where the end-of-range defects reside in order to recover a free-of-defect crystalline material after the epitaxial regrowth. This condition can be easily achieved in non-patterned samples where LTA shows exceptional potentiality. The great limits of LTA emerge when passing from demo one-dimensional specimens to proper MOSFET patterned samples. Indeed, this limits has been evidenced in a series of recent experimental and theoretical works devoted to investigate the LTA integration issue in the fabrication of Si based MOSFETs [49, 50, 77]. In particular, melting of the gate material of the transistor cannot be avoided due to the modality of heat absorption and diffusion during irradiation. As a consequence design modifications, which can be hardly applied to ultra scaled CMOS devices, are required to overcome these difficulties [77].

Due to some superior electrical properties, current and next generations MOSFET devices are (will be) built using Si-Ge [32] and (possibly) Ge [66] semiconductor materials. The use of LTA in combination with the use of the Si-Ge material has been suggested recently in order to obtain at once highly active dopant profiles and graded $Si_{1-x}Ge_x$layers [68, 69]. Again non-patterned samples have been used in these investigation. Anyhow, the different optical and thermal properties of Ge and Si-Ge (e.g. lower melting point and latent heat) could open, in principle, new perspectives for the use LTA in CMOS device fabrication process flow. In the following we explore this possibility by means of numerical simulations based on a phase field model for the estimate of the material modifications. In this model the heat source distribution is calculated by solving the Maxwell equations for the laser light interacting with the transistor structure in study.

5.3. LTA simulation approach for Si-Ge structures

Heat diffusion, melting, Si-Ge alloy redistribution and impurity evolution in an irradiated CMOS structure is simulated by means of a phase-field approach, as done likewise on the previous chapters. The phase-field methodology is especially suited for studying this problem since it deals consistently with the non-equilibrium segregation and curved melting front evolution [49, 50]. In the present investigation, as done on subsection 3.4.2, we chose to implement the Wheeler phase-field approach [104] which allows to account for solute trapping effects during solidification in melting process (see Appendix C for a detailed description). In the numerical simulations phase $\varPhi$ ($0 \leq \varPhi \leq 1$ with $\varPhi = 1$ and $\varPhi = 0$ for the pure solid and liquid phases, respectively), the temperature T, Ge volume fraction c_{Ge} and impurity (boron) volume fraction c_X evolve according to the following coupled differential equations:

$$\frac{\partial \varPhi}{\partial t} = D_{\varPhi} \nabla^2 \varPhi - \frac{2D_{\varPhi}}{l^2} \left\{ \varPhi \left[1 - \varPhi\right] \left[0.5 + \beta - \varPhi\right] \right\} \tag{5.1}$$

$$\frac{\partial c_{\mathrm{Ge}}}{\partial t} = \nabla D_{\mathrm{Ge}} \nabla c_{\mathrm{Ge}} - \ln\left(K_0^{\mathrm{Ge}}\right) \nabla \left[D_{\mathrm{Ge}} c_{\mathrm{Ge}} \left(1 - c_{\mathrm{Ge}}\right) \varPhi \left(1 - \varPhi\right) \nabla \varPhi\right] \tag{5.2}$$

$$\frac{\partial c_{\mathrm{X}}}{\partial t} = \nabla D_{\mathrm{X}} \nabla c - \ln\left(K_0^{\mathrm{X}}\right) \nabla \left[D_{\mathrm{X}} c_{\mathrm{X}} \left(1 - c_{\mathrm{X}}\right) \varPhi \left(1 - \varPhi\right) \nabla \varPhi\right] \tag{5.3}$$

$$\rho c_s \frac{\partial T}{\partial t} + 6L\Phi\left(1-\Phi\right)\frac{\partial \Phi}{\partial t} = \nabla k \nabla T + S\left(\mathbf{r}, t\right). \tag{5.4}$$

In these equations, l is the interface thickness, L is the latent heat, ρ the density, c_s the specific heat, D_Φ the phase field diffusivity, K_0 the equilibrium segregation coefficients, D_{Ge} the Ge (alloy) diffusivity, D_X the impurity diffusivity and k the thermal conductivity. $\beta = \beta(c,T)$ is related to the liquid-solid interface speed as a function of T and the local composition [49, 50]. About the phase field diffusivity, it depends on the interface thickness and the characteristic time of attachment of atoms at the interface t_c (i.e. $D_\Phi = l^2/\,t_c$) [41]. All the parameters except K_0 and l are local and can depend on the other field according to suitable interpolation laws (e.g. k depends on phase, local composition and T). Apart from the modifications due to the inclusion of Ge, the parameter calibration of the phase-field methodology is discussed in Ref. [49]. The Ge related parameters are derived from the literature (see Refs. [31, 39, 63, 69]). The absorbed heat source $S(\boldsymbol{r},t)$ is evaluated by simulating self-consistently the interaction between the laser electromagnetic wave and the transistor structures [51].

We have simulated non-patterned and patterned systems. The results obtained for non-patterned structures are useful to test the simulation reliability as they can be easily compared with experimental results. We considered a 50 nm thick Ge containing film deposited on a c-Si substrate. When specified, we have also simulated samples implanted with B (chemical profiles for the 500 eV 10^{15} cm^{-2} implant have been interpolated in the simulation box). 2D patterned periodic structures (see e.g. Figure 5.3) are designed with gate stacks of L_{gate} length made by t_{ox} thick SiO$_2$ and t_{poly} thick (poly)crystalline Si. A 40 nm wide, 185 nm deep trench insulator (SiO$_2$) is also considered, positioned at half of the distance L_{period} between two adjacent gates. The initial temperature of the system is 300 K, the laser wavelength is 308 nm and the pulse is $\sim$ 30 ns wide [49].

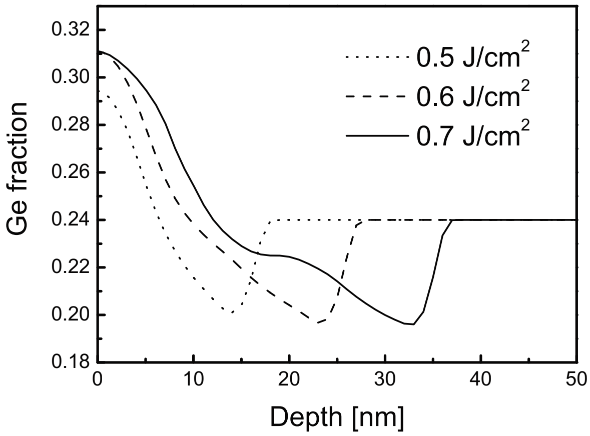

Figure 5.1.: Simulated final Ge profile as a function of laser energy for different LTA processes. The initial uniform Ge fraction in the 50 nm thick deposited film is 0.24.

5.4. Simulation results in non-patterned and patterned samples

In Figure 5.1 the simulated Ge volume fraction x of the Si$_{1\text{-}x}$Ge$_x$ film as a function of the position in a non-patterned and non-implanted sample after LTA processes at different energy densities is shown. The constant composition before the LTA is $x = 0.24$. The melt depth is $\sim$ 17, 27, 37 nm for the 0.5, 0.6, 0.7 J/cm^2 cases respectively. The alloy redistribution is due to Ge non equilibrium segregation K_0^{Ge}= 0.33 which causes a depletion of the Ge content near the melt depth region and an accumulation of Ge near the surface. A graded Ge profile, with a maximum density ($x \sim 0.31$) at the surface, is formed after the LTA process which can be useful for strain engineering in SiGe devices [68]. We note that these results, also considering the small differences in the irradiation conditions, are in a good agreement with the experimental ones (see Ref. [68]). This fact demonstrates the reliability of the method and the used calibration.

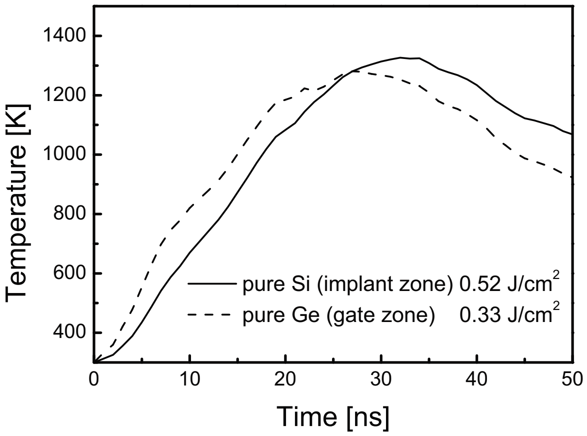

Figure 5.2.: Temperature as a function of the time from the start of the LTA process. Temperature profiles are extracted in two different points of the simulation box and for two different processes and structures: (a) point in the implant region (square in Fig. 3 upper panel) and 0.52 J/cm^2 fluence process with pure Si in the implant region (solid line); (b) point in the gate region (large dot in Fig. 3 upper panel) and 0.33 J/cm^2 fluence process with a pure Ge film in the implant region (dashed line).

These intriguing results in terms of application potentiality have to be re-addressed in patterned and implanted structures. Firstly, we will show the result relative to a particular geometry choice characterized by the following scale parameters L_{gate}= 50 nm, t_{ox}= 5 nm, t_{poly} = 60 nm, L_{period} = 300 nm. As will be clear in the following, these dimensions are rather critical for the application of the LTA process in a pure Si device. In Figure 5.2 the solid line shows the temperature in a point of the implanted region (in the point indicated by the square in Figure 5.3) as a function of time during the irradiation (0.52 J/cm^2 fluence) for the case of the pure Si (solid line) active device zone.

We assume the same melting point for Si and poly Si (1690 K). Melting LTA cannot be used for the pure Si material, since the fluence 0.52

J/cm^2 corresponds to the melting threshold for the gate material while the maximum temperature $\sim$ 1300 K reached in the implanted zone is well below the melting point (of course no benefit can be achieved by means of an eventual pre-amorphisation process). We note that the different melting threshold (in fluence) for the poly region and the substrate region in the case of a pure Si device is typical of a patterned sample due to the non uniform LTA heat source and 2D heat diffusion (see e.g. Ref. [50, 51]). The scenario completely changes if the film material is formed by pure Ge (i.e. the best case).

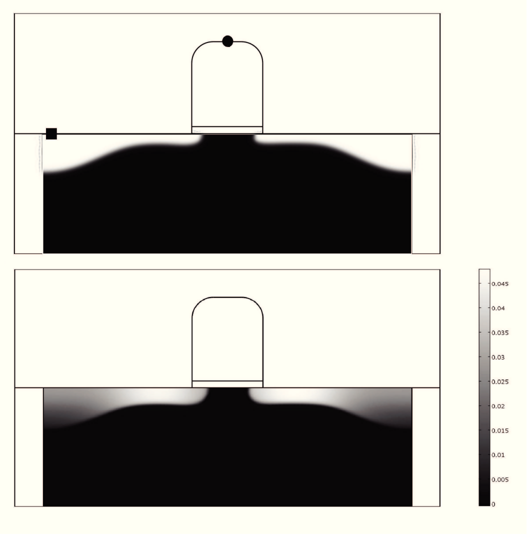

Figure 5.3.: (upper Panel) Snapshot of the phase field function (plotted in the film and substrate regions only) in gray scale, liquid $\Phi = 0$ (white) and solid $\Phi = 1$ (black), obtained after 33 ns of simulated evolution during a LTA process at 0.33 J/cm^2 in the case of pure Ge film. (lower panel) Final B dopant distribution after the end of the same process, which diffuse in the Ge film only (in volume fraction and gray scale, where white and black correspond respectively to 0.05 and 0.00 boron fraction). SiO_2 and poly-Si regions do not melt and we have included them in the figure just as a reference of the box geometry.

Figure 5.3 (upper panel) shows the phase field function (plotted in the film and substrate regions only) in gray scale, the liquid $\Phi = 0$ (white) and solid $\Phi = 1$ (black), at the instant of maximal extension of the melt front (i.e the Φ function after ~ 33 ns the irradiation start). SiO_2 and PolySi regions are not-melted (i.e. phase variable is 1). Box like B dopant profiles in the Ge film with step like shape at the melt depth are the result of dopant redistribution due to the melting LTA.

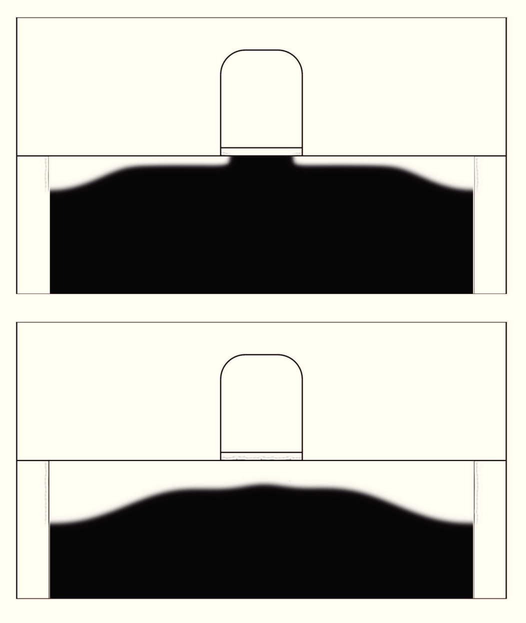

Figure 5.4.: (upper Panel) Snapshot of the phase field function in gray scale liquid $\Phi = 0$ (white) and solid $\Phi = 1$ (black) obtained after 36 ns of simulated evolution during a LTA process at 0.32 J/cm^2 in the case of pure Ge film. (lower panel) Snapshot of the phase field function in gray scale liquid $\Phi = 0$ (white) and solid $\Phi = 1$ (black) obtained after 35 ns of simulated evolution during a LTA process at 0.35 J/cm^2 in the case of pure Ge film. SiO_2 and poly-Si regions do not melt.

In the lower panel, the final B dopant two dimensional distribution which diffuses in the Ge film only after the end of the LTA (0.33 J/cm^2 fluence) is shown in volume fraction and gray scale (white and black correspond respectively to 0.05 and 0.00 boron volume fraction). A large density value of B can be obtained due the redistribution process. The temporal variation of the temperature in the poly-Si gate (i.e. in the point indicated by the circular dot in Figure 5.3) corresponding to this case is shown in Figure 5.2 (dashed line). This simulation analysis clearly demonstrates that LTA could be applied to fabricate an abrupt junction in this scaled Ge-MOSFET like structure: a localized melting is predicted in the implanted region, while the temperature in the gate stays well beyond the crystal Si melting point in the gate region. The melting threshold of the implanted region is $\sim$ 0.29 J/cm^2, whereas the melting threshold of the gate region is $\sim$ 0.45 J/cm^2. However, the process window is not limited by the gate melting only. Indeed, as it can be observed in Figure 5.4 for a LTA process at 0.35 J/cm^2 (lower panel), the melt depth extends horizontally in the whole region below the gate, and of course this melting overlap completely hinders the transistor operation. Moreover, a lower fluence of 0.32 J/cm^2 (see again Figure 5.4 upper panel) could not be sufficient for the complete recover of the implanted damage.

5.5. Discussion

The results here reported demonstrate the LTA could be integrated without any further design modification in scaled Ge-MOSFET device. Anyhow, a brief discussion on the possibility to extend this results to the SiGe alloy and on the dependence of the process window on the geometrical constraint must be added. For the geometry here analyzed in details, a useful process window for $\mathrm{Si}_{\mathit{1-x}}\mathrm{Ge}_x$ films can be obtained only for a Ge rich alloy (i.e. $x > 0.5$). For instance the interesting results obtained for $x = 0.24$ in a non-patterned sample cannot be reproduced in the MOSFET like geometry (the poly Si gate melts). The geometry modifications alter substantially the simulation results. In particular, the possibility of LTA integration, fixing the gate length, is hindered by a decrease of L_{period} or an increase of

t_{poly}+ t_{ox}. For example the simulations do not show any useful process window when L_{period} shrinks from 300 nm to 150 nm, neither for the pure Ge case. This observation also indicates the importance of future detailed atomistic studies of the liquid phase nucleation in this few tens of nanometers thick structures, aimed to improve the reliability of the simulation predictions.

A. Finite element method and Comsol code

We have implemented all the PDE based continuum models developed and determined the corresponding numerical solutions in different conditions using the COMSOL solver (see webpage www.comsol.com) of differential equations. These models account both for the solid phase evolution of systems of point defects-impurities subjected to thermal processes (section 2.4 and section 3.3), and for the dopant evolution in liquid phase of a laser irradiated silicon substrate (section 3.4), as well as the 2-D simulations of laser irradiation of SiGe based patterned structures (section 5.3).

COMSOL solver is based on the Finite Element Method (FEM). This method has been known since the '50s, but it found a wide diffusion only much later. Today, thanks to the availability of high-performance computers, has become one of the most user methods of calculation in many branches of physics and engineering. In numerical analysis the finite element method is used to solve in an approximate way problems described by partial differential equations, reducing them to a system of algebraic equations. The main feature of the finite element method is the discretization of the initial continuum domain in a discrete one (mesh) through the use of simple shape finite elements (triangles and quadrilaterals for 2D domains, hexahedral and tetrahedral for 3D ones). Figure A.1 gives an example of 2D FEM solution (right side) for a magnetostatic configuration. The corresponding mesh (left side) is also reported, which shows a denser number of points around the object of interest. On each element characterized by this basic form, the solution of the problem is assumed to be expressed by linear combination of functions called *shape functions*. Note that the function is approximated, and not necessarily the exact values of the function will be calculated in those points, but the number that will give the least error on the global solution.

The finite element method is part of Galerkin method class, whose starting point is the so-called weak formulation of a differential problem. This formulation, based on the concept of derivative in the distributional sense, integration in the sense of Lebesgue and weighted average (by means of suitable functions called test functions), has the great advantage of requiring to the solution regular realistic characteristics and is therefore a very useful descriptive tool.

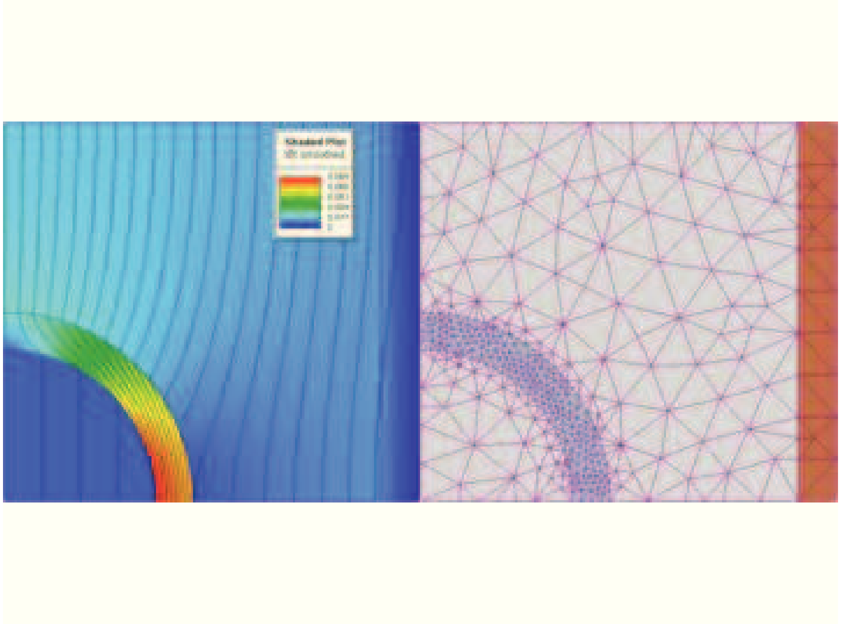

Figure A.1.: 2D FEM solution (right side) for a magnetostatic configuration (lines denote the direction of calculated flux density and color its magnitude; 2D mesh (left side) for the image above (mesh is denser around the object of interest).

The Galerkin-type methods are based on the idea of approximating the solution of a problem written in weak form by means of a linear combination of elementary functions (the shape functions). The coefficients of this linear combination (also called freedom degrees) become the unknowns of the algebraic problem obtained by the discretization. The finite elements are distinguished by the choice of the polynomial basic functions. Other Galerkin-type methods as spectral methods, use different basic functions.

In the COMSOL solver, continuum models based on partial differential equations can be implemented through a simple graphical interface (see Figure A.2).

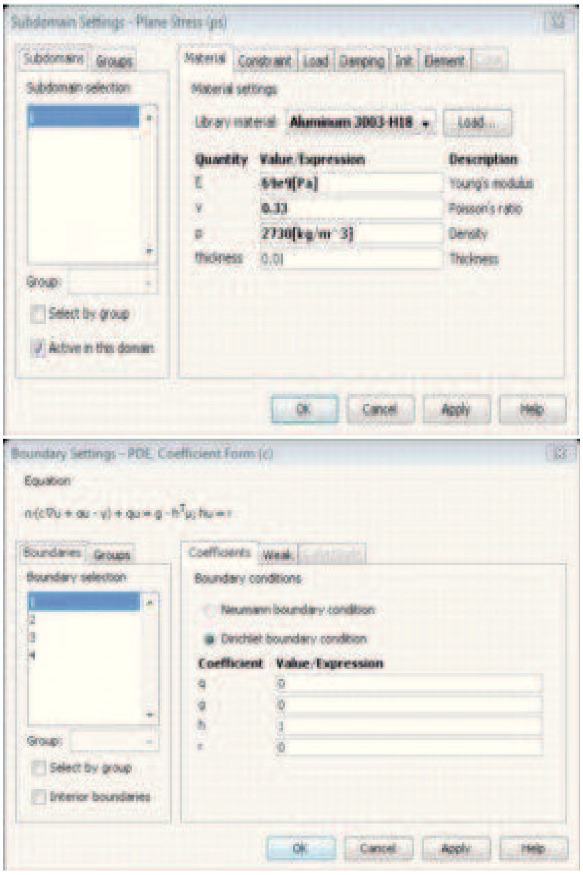

Library material: Aluminum 3003-H18

Quantity	Value/Expression	Description
E	69e9[Pa]	Young's modulus
ν	0.33	Poisson's ratio
ρ	2730[kg/m^3]	Density
thickness	0.01	Thickness

☐ Select by group

☑ Active in this domain

$n\cdot(c\nabla u + \alpha u - \gamma) + qu = g - h^T\mu$; $hu = r$

○ Neumann boundary condition

● Dirichlet boundary condition

Coefficient	Value/Expression
q	0
g	0
h	1
r	0

☐ Select by group

☐ Interior boundaries

Figure A.2.: Examples of the COMSOL solver GUI.

In particular, it is possible:

- Define the key variables of the problem, the geometry where to solve the partial differential equations (which may be one, two or three-dimensional) and the associated computational grid (mesh);
- Setting the partial differential equations and parameters which model a particular physical system;
- Impose initial and boundary conditions in a immediate and intuitive fashion;
- Visualize the setted geometry and the results obtained in one, two or three dimensions (with the aid of colors) with great graphics that make the implemented problem very realistic;
- Define, in a simple and direct way, domains over which to observe the numerical solution obtained.

The computation time for the determination of numerical solutions using the COMSOL solver is related to various factors:

- Speed of the used computer;
- Size of the domain on which the partial differential equations have to be solved (times grow with domain size);
- Number of equations to implement and degree of coupling between them;
- Convergence of the solution.

B. Binar Collision Approximation (BCA)

The Binary Collision Approximation (BCA) [1, 79] was born as an alternative to molecular dynamics models, in order to simulate radiation effects in solids and to study the energy loss of the atoms in the bulk matter, evaluating collisions between ions of the incident beam and atoms of the irradiated crystal. The main assumption of the binary collision approximation lies in considering the interactions of incident energetic particles through a succession of binary collisions with target atoms of the material in which they are introduced. In order to introduce this approximation, the projectile deflection must occur locally, at distances smaller than the crystal interatomic ones, and therefore changes in energy between the particles incident and target atoms must be close to the these latter, in order that atoms which reside on neighboring lattice positions are not involved.

The generic collision between the projectile ion and the target atom can be described as follows Figure B.1: the ion projectile with mass m_1 and kinetic energy $E_0$and the motionless target atom with mass m_2, are initially located, respectively, in P_0 and T_0. The initial distance L between them is sufficiently large that we can neglect any interaction between the two particles. This interaction becomes relevant when the ion projectile reaches a minimum distance (distance of closest approach) respect to the target atom, which by means of such collisional process receives enough energy to leave its lattice site and take part in the cascade [1, 79].

In Figure B.1 are shown the particles and the gravity center at the instant and at the distance when the collision occurs, i.e. the distance of closest approach between atoms. The motion of the gravity center is considered as long as the particles gain positions P_f and T_f in which

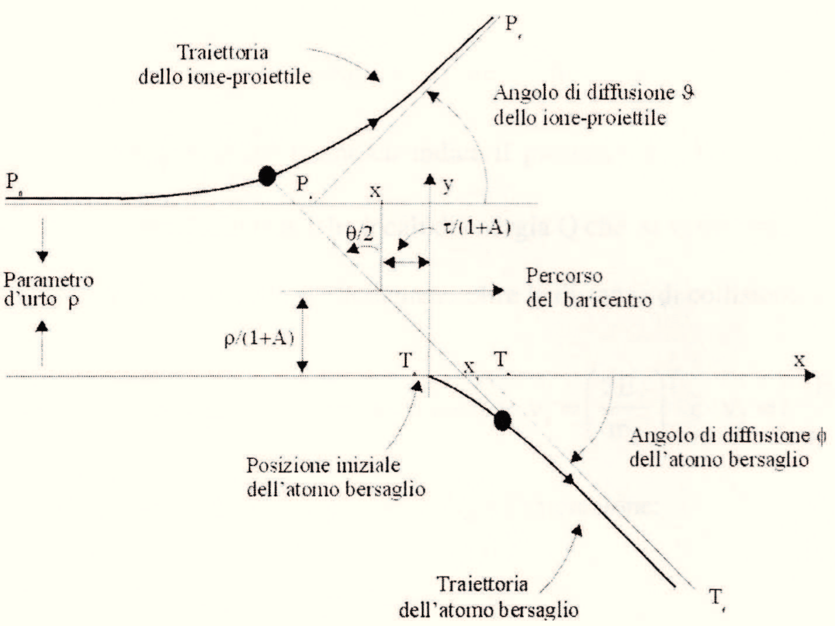

Figure B.1.: Diagram of a collision between projectile ions and target atoms. All parameters describing the interaction are shown: the projectile ion of mass m_1 and kinetic energy E_0 and the motionless target atom of mass m_2, which are initially located respectively in P_0 and T_0. The particles and the gravity center are shown at the instant and at the collision distance, i.e. the distance of closest approach between atoms.

the interactions are again ignored. The projectiles properties are estimated in P_a and T_a, which are the intersection points of the particle trajectory asymptotes.

The figure also illustrates fundamental variables of collision problems, such as the impact parameter, the time interval τ in which the two atoms interact, the collision angles ϑ and ϕin the laboratory system, and θ on gravity center system. The relationship between them is given by [79]:

$$\tan \vartheta = \frac{Af \sin \theta}{1 + Af \cos \theta} \tag{B.1}$$

$$\tan \phi = \frac{f \sin \theta}{1 - f \cos \theta}, \tag{B.2}$$

where A is the ratio between the interacting particle masses $m_2/m_1$and $f = \left[1 - (1 + A)\, Q/AE_0\right]^{1/2}$, which reciprocal value indicates the interaction over time due to local inelastic energy losses Q.

As the two particles move over the collision distance, they procede with constant speeds $v_1 = (2E_1/m_1)^{1/2}$ and $v_2 = (2E_2/m_2)^{1/2}$, being $E_1$and E_2 the energies of the two particles after the interaction:

$$E_1 = \frac{\left[(1 - fA)^2 + 4fA \cos^2(\theta/2)\right] E_0}{(1 + A)^2} \tag{B.3}$$

$$E_1 = \frac{\left[(1 - fA)^2 + 4fA \sin^2(\theta/2)\right] E_0}{(1 + A)^2}. \tag{B.4}$$

Obviously, the target atom must have an energy higher than the binding energy E_b to leave its lattice site, its kinetic energy is therefore reduced to E_2- E_b. Crystal Trim Code may adopt different values for $E_b$depending on the different cases which can occur during the collisional cascade. Any collision can be divided into an elastic to inelastic part. The elastic part produces the projectile deflection as a result of the interaction between the incident energetic particles and target atoms. In Crystal Trim the local inelastic energy loss in a collision, due to electronic excitations of the involved atoms is the product of the specific loss of Lindhard, Scharff and Schiott [54] to an exponential function of the collision distance [6, 34, 54, 79]:

$$Q\left(p,E\right)=KE^{\frac{1}{2}}\frac{\gamma^{2}}{2\pi a^{2}}\exp\left(\frac{-\gamma R\left(p,E\right)}{a}\right), \tag{B.5}$$

where *R(p, E)* is the collision distance, E the kinetic projectile energy, a the shielding length, γ a parameter. $K = aK_L$ being a a fitting parameter and

$$K_L=\frac{1.216\cdot Z_1^{\frac{7}{6}}\cdot Z_2}{\left(Z_1^{\frac{2}{3}}+Z_2^{\frac{2}{3}}\right)M_1^{\frac{1}{2}}}, \tag{B.6}$$

is the specific loss of Lindhard-Scharff with M_1 the mass of the ion incident in atomic mass units. The values of a vary according to the ion chosen and include the cross section dependence from the atomic number Z. The inelastic stopping cross section associated with Equation B.5 is [79]

$$S_e\left(E\right)=2\pi\int_0^{p_c}pQ\left(p,E\right)dp=K\,E^{\frac{1}{2}}\sigma\left(E\right), \tag{B.7}$$

where p_c is the maximum impact parameter value determined by the density and structure of the target and *σ(E)* is a function of the deflection which approaches the unity for high energies and assumes fractional values at lower ones. In the high energy approximation, Equation B.7 becomes:

$$S_e\left(E\right)=K\,E^{\frac{1}{2}}, \tag{B.8}$$

which is the one adopted by Cristal Trim Code.

In the original model of Oen-Robinson (OR) $\gamma = 0.3$ [1]. Most recent calculations of molecular orbitals [6] and local electron density [34] give a range of values for γ between 0.22 and 0.46 and this value increases with energy.

C. Wheeler phase-field formulation

We present the Wheeler phase-field methodology [3, 103, 104] applied to the simulation of dopant redistribution in Si during an excimer laser annealing process. The kinetic model, derived in the framework of the Ginsberg-Landau thermodynamic formalism, is made up by three coupled equations ruling the concurrent evolution of the thermal, phase and impurity fields.

The previously presented Karma phase-field formalism [41] (details are given on subsection 1.4.3), was applied for the simulation of the melting of an irradiated substrate. Summarizing, a continuum field φ (with $-1 \leq \varphi \leq 1$, being $\varphi = -1$ and $\varphi = 1$ in the pure liquid and solid phases, respectively) is used to describe smooth phase transitions. The phase field and heat equations, modeling thermal field and phase transition evolution[41] in the laser annealing process, are:

$$\tau \frac{\partial \varphi}{\partial t} = W^2 \nabla^2 \varphi - \varphi \left(\varphi^2 - 1 \right) - \lambda \frac{c_p}{L_{fus}} \left(T - T_M \right) \left(\varphi^2 - 1 \right)^2 \quad \text{(C.1)}$$

$$\rho c_p \frac{\partial T}{\partial t} - \nabla^2 \left(KT \right) = \frac{\rho L_{fus}}{2} \frac{15}{8} \left(\varphi^2 - 1 \right) \frac{\partial \varphi}{\partial t} + S\left(x, t \right), \quad \text{(C.2)}$$

where $S(x, t) = E_{las} P(t)(1 - R) a \exp(-ax)$ is the heat source due to the absorption of laser light. $E_{las}$is the incident laser energy, $P(t)$ is the normalized laser pulse shape, and R and a are the phase and temperature dependent surface reflectivity and the material absorption at the laser wavelength, respectively.

Hence, the Karma approach, from the dopant point of view, appears similar to more simplified models of alloy melting. Conventional models [105, 106] of the dopant distribution during excimer laser annealing (ELA) are based on the numerical solution of the heat diffusion equation, that allows to simulate the liquid-solid interface evolution. Furthermore, the dopant diffusion is based on a sharp-interface model of the alloy solidification and a step-like change of the mass transport properties across the interface. The matching between the solutions in the liquid and solid zones at the solid-liquid interface is obtained from the mass conservation and from a segregation model ruling the jump in concentration across the interface itself. The sharp-interface model, which de-couples thermal and mass evolution and does not consider the physical properties of the interface layer itself, allows only a phenomenological approach of the segregation problem. Indeed, the dependence of the segregation coefficient on the interface speed can be included by fitting the experimental results.

The Wheeler phase-field approach [103] improves the physical description of the moving phase boundary problem including a dopant concentration dependency of the system free energy, as done for the phase and temperature field. Therefore, phase-field, temperature and dopant density evolve concurrently according to proper coupled differential equations. Therefore, the dopant redistribution is automatically evaluated solving the complete evolution problem.

Likewise to the Karma formulation (subsection 1.4.3), Wheeler equations are based on the Ginsberg-Landau approach of the phase transition problem. According to that, the system Helmoltz free energy F is written as a functional of the phase parameter Φ (with $0 \leq \Phi \leq 1$), being $\Phi = 0$ and $\Phi = 1$ in the pure liquid and solid phases, respectively. The functional is an approximate continuum limit of the real system free energy and it has the following form

$$F = \int_{\Omega} \left[f\left(\Phi, T, c\right) + \frac{\epsilon}{2} |\nabla \Phi|^2 \right] dV \tag{C.3}$$

where ϵ is the (kinetic) parameter controlling the local fluctuations of the phase field. The volume integral in Eq. (Equation C.3) (dV is the volume increment) is extended to the whole system volume Ω. For a binary alloy, the potential part, $f(\Phi, T, c)$, depends on the solute density field c (and, of course, on the phase and thermal fields Φ and T). In the limit of a diluted solution of a dopant X in Si host we can express $f(\Phi, T, c)$ as a linear superposition of the two terms, f_{Si} and f_X, related to the two species, plus a term related to entropy of mixing i.e :

$$f(\Phi, T, c) = (1-c) f_{Si}(\Phi, T) + c f_X(\Phi, T) + \tag{C.4}$$

$$+\frac{kT}{v_m}[clnc + (1-c)ln(1-c)] \ ,$$

where v_m is the solvent molecular volume. The phase dependent factor is usually expressed as the sum of a double minimum function plus a term which drives the phase transition (here A=Si or X) [3]

$$\begin{aligned} f_A(\Phi, T) &= \frac{W}{4} g(\Phi) + \frac{W\beta_A(T)}{6} p(\Phi) = \\ &= \frac{W}{4}\Phi^2(1-\Phi^2) + \frac{W\beta_A(T)}{6}\Phi^2(3-2\Phi). \end{aligned} \tag{C.5}$$

Here $W = W_{Si} = W_X$ is the barrier height separating the minimum at $\Phi = 0$ from the minimum at $\Phi = 1$, (assumed to be independent from the solute presence), while $\beta_A(T)$ determines the absolute minimum (and therefore the stable phase) as a function of T.

The kinetic equations are formulated in terms of the functional derivatives of F with respect to Φ and c [3]:

$$\frac{\partial \Phi}{\partial t} = M_1 \frac{\delta F}{\delta \Phi} \ , \tag{C.6}$$

$$\frac{\partial c}{\partial t} = \nabla \left[M_2 c(1-c) \nabla \frac{\delta F}{\delta c} \right] \ . \tag{C.7}$$

The two positive parameters M_1 and M_2 are related to the interface and solute mobility, respectively. The previous equations should be joined to the heat diffusion equation in order to describe the system evolution. Therefore, our model is ruled by the following equations

$$\begin{aligned} \frac{\partial \Phi}{\partial t} &= D_\Phi \nabla^2(\Phi) - \\ &- \frac{2D_\Phi}{l^2} \left[\Phi(1-\Phi)(0.5 + c\beta_X(T) + (1-c)\beta_{Si}(T) - \Phi) \right] \ , \end{aligned} \tag{C.8}$$

$$\begin{aligned} \frac{\partial c}{\partial t} = \ & \nabla \ \ [D_c(\Phi)\nabla c] + \\ + \ & W(\beta_X(T) - \beta_{Si}(T)) \nabla \left[M_2 c(1-c)\Phi(1-\Phi)\nabla\Phi \right] \ , \end{aligned} \tag{C.9}$$

$$\begin{aligned} \frac{\partial u}{\partial t} &= \rho c_V \frac{\partial T}{\partial t} + 6\Phi(1-\Phi)[L_{\mathrm{Si}} + c\Delta L_{\mathrm{Si-X}}] \frac{\partial \Phi}{\partial t} = \\ &= \nabla \left[K(\Phi)\nabla T \right] + S(\mathbf{r}, t). \end{aligned} \tag{C.10}$$

In these equations, L_{Si} is the latent heat of pure silicon, $\Delta L_{\mathrm{Si-X}}$ is its change due to the solute, ρ is the Si density, c_V the (constant volume) specific heat. We indicate with $S(\mathbf{r}, t)$ the time and space dependent external heat sources. Moreover, we assume that the phase dependent thermal conductivity, $K(\Phi)$, interpolates linearly between the values in the solid and liquid phase: $K(\Phi) = K_{sol}\Phi + K_{liq}(1-\Phi)$. The microscopic parameters in Eqs. (Equation C.8-Equation C.10) can be related to macroscopic ones by means of the following relations: [3]

$$\begin{aligned} \epsilon^2 &= 6\sigma l, \;\; W = 12\sigma l, \\ \beta_A(T) &= \frac{l v_A^{int}(T)}{2\mu\sigma}, \;\; \mu = 6M_1 l \\ D_\Phi &= 6M_1\sigma l \;, \;\; D_c = \frac{M_2 v_{Si}^{int}}{kT} \;. \end{aligned} \tag{C.11}$$

Here σ is the surface energy, l the interface thickness, μ the kinetic coefficient (also know as interface mobility), $v_A^{int}(T)$ the interface speed as function of T, D_Φ the phase-field diffusivity, $D_c(\Phi)$ the dopant diffusivity. In the pure solvent case, a Fulcher-Vogel like [92] expression for the interface speed $v_{\mathrm{Si}}^{int}(T)$ as a function of T can be adopted:

$$v_{Si}^{int}(T) \propto \exp\left[-\frac{E_g}{k(T-T_g)}\right] \times exp\left[-\frac{L_{Si}(T-T_{melt})}{kN_{Si}TT_{melt}}\right] \tag{C.12}$$

where N_{Si} is the Si atomic density while the parameter values are $E_g = 0.082$ eV and $T_g = 1040$ K [92]. We fix the free pre-factor in Eq. (Equation C.12) by imposing the maximum value of v_{Si}^{int} for the different (crystal, amorphous) phases as reported in Table I [14]. In the diluted alloy approximation [16] we can neglect the solute effect on all microscopic parameters except than on the difference $\beta_X(T) - \beta_{Si}(T)$. Moreover, we can approximate in Equation C.9

$$W(\beta_X(T) - \beta_{Si}(T))M_2 \sim -D_c(\Phi)ln(K_0) \tag{C.13}$$

where K_0 is the equilibrium segregation coefficient. Our simulation code is based on Equation C.8 - Equation C.10, that can describe the concurrent evolution of the thermal, phase and dopant density fields, during the laser irradiation. Generally, such equations have to be solved using an explicit scheme and a proper discrete approximation of the continuum equations over a one dimensional grid. Simulation results for the melting and the re-growth stages respectively, show that the phase-field has a quasi-soliton like behaviour. Indeed, we note that, in the case of constant temperature ($T = T^*$) and pure solvent (c $\equiv$ 0), the analytical solution of the phase-field equation (Equation C.8) is an hyperbolic tangent wave moving with a fixed speed $v^{int}(T^*)$ [3], i.e.

$$\Phi(x,t) = \frac{1}{2}\left[1 - tanh\left(\frac{t - v^{int}(T^*)t}{2l}\right)\right]. \tag{C.14}$$

Our phase-field simulations can be used to understand experimental data and to study the dopant redistribution during ELA process. Before that, in order to show the code capability, we discuss here the phase and density field evolution obtained in an ideal simulation, taken as example case.

We considered, in fact, a stack on top of a c-Si substrate formed by 50 nm thick a-Si and 3 nm thick SiO_2. We consider the following initial conditions: an uniform thermal field with a temperature $T_{in} = 450°C$, the solid phase $\Phi = 1$ for all the materials, an ideal box-like density field extending from the SiO_2/a-Si interface down in the bulk for a depth of 40 nm, with a plateau of 2.5×10^{20} cm^{-3}. For the sake of generality, we consider an ideal impurity atom and we choose the impurity dependent parameters (diffusivities, phase field thresholds and equilibrium segregation coefficient) as $D_{liq} = 2. \times 10^{-4}$ cm^2/s , $D_{sol} = 1. \times 10^{-10}$ cm^2/s , $D_{SiO_2} = 1. \times 10^{-10}$ cm^2/s, $K_0 = 0.1$. The other parameters related to the thermal properties of the materials are reported in Table C.1.

In our case, the moving boundary preserves approximately a hyperbolic tangent shape, while the related instantaneous speed varies consistently with the thermal and solute density field evolution. During melting, the dopant redistribution (see dashed lines in Figure C.1) is then governed by the boundary motion. In the re-growth stage (see solid line in Figure C.1) the impurity atoms redistribution is characterized by the segregation phenomenon, which determines the impurity atom local density level incorporated in the solid phase. Indeed, we note how the segregation peak follows the boundary motion, being its evolution strictly connected to that of the phase-field in the transition zone $0 < \Phi(t) < 1$.

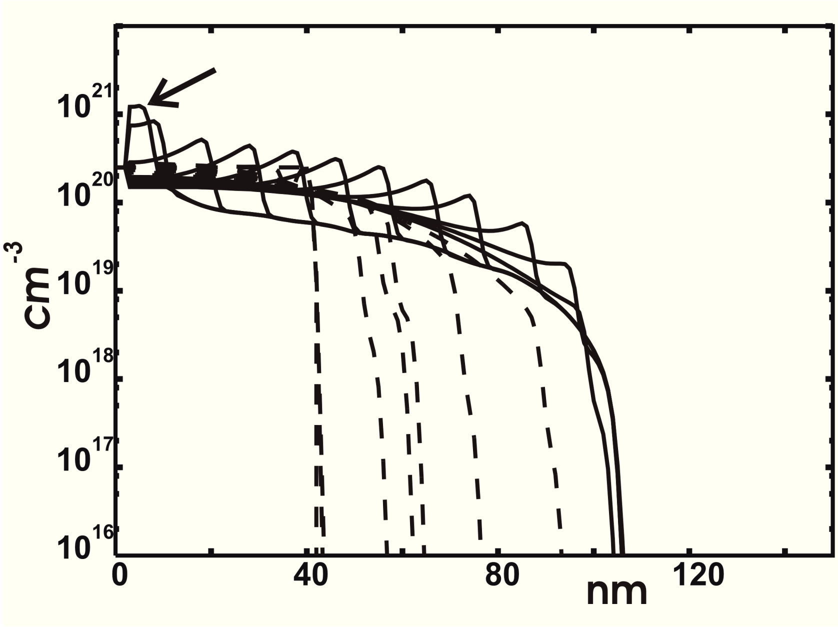

Figure C.1.: Example of density field evolution during an ELA process at 0.717 J/cm^2 energy density (single shot). Solid (dashes) line indicates the profiles in the re-growth (melting) state, while the black arrow points to final profile. The time interval between two density profile is $\delta t = 5$ns.

The non equilibrium solute trapping, as well as the solute drag (i.e., the free energy dissipated by the moving boundary) phenomena, have a natural description in the phase-field formalism [3]. In the uniform temperature case ($\nabla T \equiv 0$), the analysis of the equations, similar to that used in our modeling, have shown [3] that such phenomena significantly occur when the boundary speed is large enough. In such conditions, in fact, the diffusion flux of the solute atoms across the boundary is comparable to the flux spanned by the moving boundary. In turn, equilibrium properties are recovered at low speed.

The main characteristic of Wheeler phase-field formulation, with respect to the sharp interface approximation or Karma formulation, is the most realistic (if we consider the atomic description) finite dimension of the alloy solid-liquid boundary, which, according to rigorous thermodynamic considerations, has a proper inner kinetic. In this framework, dopant redistribution due to laser pulse is the result of the overall non-equilibrium kinetics evolution. Typical non equilibrium phenomena, like the solute trapping and drag, are consistently described without including extrinsic parameters (e.g. a non-equilibrium segregation parameter dependent on the boundary speed).

Par.	value or expression [14, 21, 102]	units
$K_{c-Si}(T < 1200)$	$1523.7(T)^{-1.226}$	$[J/(scmK)]$
$K_{c-Si}(T \geq 1200)$	$9.(T)^{-0.502}$	$[J/(scmK)]$
K_{a-Si}	0.018	$[J/(scmK)]$
K_{l-Si}	$0.502 + 2.93 \times 10^{-4}(T - T_c)$	$[J/(scmK)]$
$K_{SiO_2}(T < 1170)$	$1.005 \times 10{-}2 + 1.298 \times 10^{-5}T$	$[J/(scmK)]$
$K_{SiO_2}(T \geq 1170)$	2.512×10^{-2}	$[J/(scmK)]$
c_{c-Si}	$0.6949\exp(2.375 \times 10^{-4}T)$	$[J/(gK)]$
c_{a-Si}	$0.6949\exp(2.375 \times 10^{-4}T)$	$[J/(gK)]$
c_{l-Si}	1	$[J/(gK)]$
c_{SiO_2}	$0.604 + 5.118 \times 10^{-4}(T - T_c)$	$[J/(gK)]$
T_{melt-c}	1690	$[K]$
T_{melt-a}	1420	$[K]$
L_c	1780	$[J/g]$
L_a	1320	$[J/g]$
σ_c	3.45×10^{-5}	$[J/cm^2]$
σ_a	1.8×10^{-5}	$[J/cm^2]$
μ_c	600	$[cm^4/Js]$
μ_a	600	$[cm^4/Js]$
l_c	1×10^{-7}	$[cm]$
l_a	1×10^{-7}	$[cm]$
v_{int-c}^{max}	1500	$[cm/s]$
v_{int-a}^{max}	2500	$[cm/s]$

Table C.1.: Values of the thermal parameters used in the simulations of the ELA process of doped SiO_2-Si stacks

Acknowledgments

I would like to acknowledge Dr. Antonino La Magna for guidance, support and patience throughout this PhD period and Prof. Giovanni Piccitto for his tutoring work.

I am grateful to Dr. Vittorio Privitera for the prolific scientific discussions and the experimental planning which lies at the basis of the Ph. D. research activity.

I would like to thank Dr. Ioannis Deretzs for his computational support and the ultimate revision of the present thesis.

I am grateful to Dr. Karim Huet and Dr. Julien Venturini of EXCICO Company, France for the planning, management and post-processing analysis of the whole experimental scenario, i.e. implantation, laser annealing and SIMS measurements of the processed specimens, widely discussed on chapter 3 concerning phosphorus activation and boron pile-up on laser irradiated implanted silicon.

I am also grateful to Markus Italia for the SRP measurements of the irradiated samples.

I would like to thank Prof. Lourdes Pelaz, Prof. Luis A. Marqués, Prof. Maria Aboy, Prof. Pedro Lopez, Prof. Pedro Castrillo Romón and all department co-workers for hospitality and collaboration during the four-months period spent at the Departamento de Electrónica Universidad de Valladolid (Spain) from February to May 2011. Within this collaboration I developed from scratch the Kinetic Monte Carlo code presented on chapter 4.

I would also like to thank the remaining people of the CNR-IMM research group: Massimo Camarda, Giovanni Mannino, Giovanna Pellegrino, Silvia Scalese, Viviana Scuderi, Alessandra Alberti, Rosaria Puglisi, Cristina Garozzo, Rosa Ruggeri, Antonio Marino, Aldo Spada, Giuseppe Nicotra. A special thanks goes to all CNR-IMM staff as well as the institute director Dr. Corrado Spinella.

Finally a big thanks to family and friends.

Curriculum Vitae

Giuseppe Fisicaro was born on the 2nd of May 1981 in Ragusa. He attained his Degree in Physics (Condensed Matter Physics) from the University of Catania in 2008 (110/110 cum laude). In 2008 he was also admitted to the Ph.D. course in Physics at the University of Catania, developing his research activities in collaboration with the Institute for Microelectronics and Microsystems (IMM) of the CNR. During the Ph. D. period he spent four months as visiting student at the Department of Electronics, University of Valladolid (Spain). He has also collaborated with the EXCICO Laser Company of France. His research activities concern: the theoretical investigation of materials by statistical and kinetic methods (e. g. Monte Carlo and continuum models); the development and implementation of codes for the simulation of materials for microelectronics, manufacturing processes (e. g. laser and thermal heating, dielectrophoretic cell isolation devices) and semiconductor device operation (dopant activation and melting redistribution under laser irradiation). He is author or coauthor of several publications in international journals (JCR). During the Ph.D. course he has presented the results of his work at the following conferences, giving oral contributions: 17th IEEE International Conference on Advanced Thermal Processing of Semiconductors - RTP 2009 (Albany, NY), E-MRS Spring Meeting 2010 (Strasbourg, France), XCVI National Congress of the Italian Physical Society 2010 (Bologna, Italy), 12th International Symposium on Laser Precision Microfabrication 2011 (Takamatsu, Giappone), E-MRS-Spring Meeting 2011 (Nizza, Francia). He is a member of the Italian Physical Society (SIF) and the European Materials Research Society (EMRS).

List of Publications

This thesis is based on the following publications:

1. A. La Magna, G. Fisicaro, G. Mannino, V. Privitera, G. Piccitto, B. G. Svensson, and L. Vines, “Defect and dopant kinetics in laser anneals of Si”, *Mater. Sci. Eng., B* **154-155**, 35-38 (2008)
2. K. Huet, G. Fisicaro, J. Venturini, H. Besaucèle, and A. La Magna, “Defect kinetics and dopant activation in submicrosecond laser thermal processes”, *Appl. Phys. Lett.* **95**(3), 231901 (2009)
3. G. Mannino, C. Spinella, R. Ruggeri, A. La Magna, G. Fisicaro, E. Fazio, F. Neri, and V. Privitera, “Crystallization of implanted amorphous silicon during millisecond annealing by infrared laser irradiation”, *Appl. Phys. Lett.* **97**(2), 022107 (2010)
4. G. Fisicaro, M. Italia, V. Privitera, G. Piccitto, K. Huet, J. Venturini, and A. La Magna, “Dopant activation and damage evolution in implanted silicon after excimer laser annealing”, *Phys. Status Solidi C* **8**(3), 940-943 (2011)
5. G. Fisicaro, M. Italia, V. Privitera, G. Piccitto, K. Huet, J. Venturini, and A. La Magna, “Solid phase phosphorous activation in implanted silicon by excimer laser irradiation”, *J. Appl. Phys.* **109**, 113513 (2011)
6. G. Fisicaro, A. La Magna, G. Piccitto, and V. Privitera, “Laser annealing of SiGe and Ge based devices”, *Microelectron. Eng.* **88**(4), 488-491 (2011)
7. G. Fisicaro, M. Italia, V. Privitera, G. Piccitto, L. Pelaz, P. Lopez, K. Huet, J. Venturini, and A. La Magna, “Dopant activation modeling in implanted Silicon under multi-pulsed excimer

laser irradiation", *Proceedings of LPM2011 - the 12th International Symposium on Laser Precision Microfabrication*, (2011)

Bibliography

[1] Computer studies of the reflection of light ions from solids. *Nucl. Instr. Meth.*, 132.

[2] Laser and electron beam processing of materials edited by c. w. white and p. s. peercy. *Academic Press*, 1980.

[3] N. A. Ahamd, A. A. Wheeler, W. J. Boettinger, and G. B. McFadden. Solute trapping and solute drag in a phase-field model of rapid solidification. *Phys. Rev. E*, 58:3436–3450, Sep 1998. doi: 10.1103/PhysRevE.58.3436. URL `http://link.aps.org/doi/10.1103/PhysRevE.58.3436`.

[4] S. I. Anisimov, B. L. Kapeliovich, and T. L. Perel'man. Electron emission from metal surfaces exposed to ultrashort laser pulses. *Soviet Physics Jetp-Ussr*, 39:375, Feb 1974.

[5] M. J. Aziz, J. Y. Tsao, M. O. Thompson, P. S. Peercy, and C. W. White. Solute trapping: Comparison of theory with experiment. *Phys. Rev. Lett.*, 56:2489–2492, 1986.

[6] J. P. Biersack and L. G. Haggmark. A monte carlo computer program for the transport of energetic ions in amorphous targets. *Nucl. Instr. Meth.*, 174(1-2):257–269, 1980. ISSN 0029-554X. doi: 10.1016/0029-554X(80)90440-1. URL `http://www.sciencedirect.com/science/article/pii/0029554X80904401`.

[7] M. Birnbaum. Modulation of the reflectivity of semiconductors. *J. Appl. Phys.*, 36(2):657–658, 1965. ISSN 00218979. doi: DOI:10.1063/1.1714053. URL `http://dx.doi.org/10.1063/1.1714053`.

[8] M. Birnbaum. Semiconductor surface damage produced by ruby lasers. *J. Appl. Phys.*, 36(11):3688–3689, 1965. ISSN 00218979.

doi: DOI:10.1063/1.1703071. URL `http://dx.doi.org/10.1063/1.1703071`.

[9] L. M. Blinov. *Soviet Physics - Solid State*, 9:666, 1967.

[10] P. Blöchl, E. Smargiassi, R. Car, D. B. Laks, W. Andreoni, and S. Pantelides. First-principles calculations of self-diffusion constants in silicon. *Phys. Rev. Lett.*, 70:2435–2438, Apr 1993. doi: 10.1103/PhysRevLett.70.2435. URL `http://link.aps.org/doi/10.1103/PhysRevLett.70.2435`.

[11] A. Bongiorno, L. Colombo, and T. D. de la Rubia. Structural and binding properties of vacancy clusters in silicon. *Europhys. Lett.*, 43(6):695, 1998. URL `http://stacks.iop.org/0295-5075/43/i=6/a=695`.

[12] H. Bracht. Self- and foreign-atom diffusion in semiconductor isotope heterostructures. i. continuum theoretical calculations. *Phys. Rev. B*, 75(3):035210, Jan 2007. doi: 10.1103/PhysRevB.75.035210.

[13] H. Bracht, N. A. Stolwijk, and H. Mehrer. Properties of intrinsic point defects in silicon determined by zinc diffusion experiments under nonequilibrium conditions. *Phys. Rev. B*, 52(23):16542–16560, Dec 1995. doi: 10.1103/PhysRevB.52.16542.

[14] P. H. Bucksbaum and J. Bokor. Rapid melting and regrowth velocities in silicon heated by ultraviolet picosecond laser pulses. *Phys. Rev. Lett.*, 53:182–185, Jul 1984. doi: 10.1103/PhysRevLett.53.182. URL `http://link.aps.org/doi/10.1103/PhysRevLett.53.182`.

[15] G. Caginalp. Stefan and hele-shaw type models as asymptotic limits of the phase-field equations. *Phys. Rev. A*, 39:5887–5896, Jun 1989. doi: 10.1103/PhysRevA.39.5887. URL `http://link.aps.org/doi/10.1103/PhysRevA.39.5887`.

[16] G. Caginalp and W. Xie. Phase-field and sharp-interface alloy models. *Phys. Rev. E*, 48:1897–1909, Sep 1993. doi: 10.1103/PhysRevE.48.1897. URL `http://link.aps.org/doi/10.1103/PhysRevE.48.1897`.

[17] D. Caliste and P. Pochet. Vacancy-assisted diffusion in silicon: A three-temperature-regime model. *Phys. Rev. Lett.*, 97(13): 135901, Sep 2006. doi: 10.1103/PhysRevLett.97.135901.

[18] J. Crank. *Free and Moving Boundary Problems.* Clarendon Press, Oxford, 1984.

[19] F. Cristiano, N. Cherkashin, X. Hebras, P. Calvo, Y. Lamrani, E. Scheid, B. de Mauduit, B. Colombeau, W. Lerch, S. Paul, and A. Claverie. Ion beam induced defects in crystalline silicon. *Nucl. Instrum. Methods Phys. Res. B*, 216 (0):46 – 56, 2004. ISSN 0168-583X. doi: 10.1016/j.nimb.2003.11.019. URL `http://www.sciencedirect.com/science/article/pii/S0168583X03021244`. ¡ce:title¿Proceedings of the E-MRS 2003 Symposium E on Ion Beams for Nanoscale Surface Modifications¡/ce:title¿.

[20] A. W. Date. A strong enthalpy formulation for the stefan problem. *International Journal of Heat and Mass Transfer*, 34:2231–2283, 1991.

[21] E. P. Donovan, F. Spaepen, D. Turnbull, J. M. Poate, and D. C. Jacobson. Heat of crystallization and melting point of amorphous silicon. *Appl. Phys. Lett.*, 42(8):698–700, 1983. doi: 10.1063/1.94077. URL `http://link.aip.org/link/?APL/42/698/1`.

[22] P. Fahey, G. Barbuscia, M. Moslehi, and R. W. Dutton. Kinetics of thermal nitridation processes in the study of dopant diffusion mechanisms in silicon. *Appl. Phys. Lett.*, 46:784, 1985.

[23] P. M. Fahey, P. B. Griffin, and J. D. Plummer. Point defects and dopant diffusion in silicon. *Rev. Mod. Phys.*, 61:289–384, Apr 1989. doi: 10.1103/RevModPhys.61.289. URL `http://link.aps.org/doi/10.1103/RevModPhys.61.289`.

[24] R. B. Fair and J. C. C. Tsai. A quantitative model for the diffusion of phosphorus in silicon and the emitter dip effect. *J. Electrochem. Soc.*, 124(7):1107–1118, 1977. doi: 10.1149/1.2133492. URL `http://link.aip.org/link/?JES/124/1107/1`.

[25] G. Fisicaro, M. Italia, V. Privitera, G. Piccitto, K. Huet, J. Venturini, and A. La Magna. Dopant activation and damage evolution in implanted silicon after excimer laser annealing. *Phys. Status Solidi C*, 8(3):940–943, 2011. ISSN 1610-1642. doi: 10.1002/pssc.201000252. URL `http://dx.doi.org/10.1002/pssc.201000252`.

[26] G. Fisicaro, M. Italia, V. Privitera, G. Piccitto, K. Huet, J. Venturini, and A. La Magna. Solid phase phosphorous activation in implanted silicon by excimer laser irradiation. *J. Appl. Phys.*, 109:113513, 2011. doi: 10.1063/1.3592262.

[27] G. Fisicaro, A. La Magna, G. Piccitto, and V. Privitera. Laser annealing of sige and ge based devices. *Microelectron. Eng.*, 88(4):488 – 491, 2011. ISSN 0167-9317. doi: 10.1016/j.mee.2010.09.014. URL `http://www.sciencedirect.com/science/article/pii/S0167931710003473`.

[28] G. Fortunato. Polycrystalline silicon thin-film transistors: A continuous evolving technology. *Thin Solid Films*, 296(1-2): 82 – 90, 1997. ISSN 0040-6090. doi: 10.1016/S0040-6090(96)09378-9. URL `http://www.sciencedirect.com/science/article/pii/S0040609096093789`.

[29] G. Fortunato, L. Mariucci, A. La Magna, P. Alippi, M. Italia, V. Privitera, B. Svensson, and E. Monakhov. Electrical activation phenomena induced by excimer laser annealing in b-implanted silicon. *Appl. Phys. Lett.*, 85:2268, 2004. doi: 10.1063/1.1793352.

[30] L. F. Giles, B. Colombeau, N. Cowern, W. Molzer, H. Schaefer, K. H. Bach, P. Haibach, and F. Roozeboom. Transient enhanced diffusion of b at low temperatures under extrinsic conditions. *Solid-State Electron.*, 49(4):618 – 627, 2005. doi: DOI: 10.1016/j.sse.2004.12.007. URL `http://www.sciencedirect.com/science/article/pii/S0038110105000043`.

[31] C. J. Glassbrenner and G. A. Slack. Thermal conductivity of silicon and germanium from 3°k to the melting point. *Phys. Rev.*, 134:A1058–A1069, May 1964. doi: 10.1103/PhysRev.134.

A1058. URL `http://link.aps.org/doi/10.1103/PhysRev.134.A1058`.

[32] L. Gomez, P. Hashemi, and J. L. Hoyt. Enhanced hole transport in short-channel strained-sige p-mosfets. *IEEE Trans. Elen. Dev.*, 56:2644–2651, 2009.

[33] J. P. Goss, P. R. Briddon, and R. Jones. Calculated properties of a 113 planar vacancy aggregate in si. *J. Phys.: Condens. Matter*, 16(20):3311, 2004. URL `http://stacks.iop.org/0953-8984/16/i=20/a=002`.

[34] P. L. Grande and G. Schiwietz. Energy loss of slow ions: one-band calculation for alkaline metals. *Phys. Lett. A*, 163(5-6): 439 – 446, 1992. ISSN 0375-9601. doi: 10.1016/0375-9601(92)90853-E. URL `http://www.sciencedirect.com/science/article/pii/037596019290853E`.

[35] M. Hernandez, J. Venturini, D. Berard, G. Kerrien, T. Sarnet, D. Debarre, J. Boulmer, C. Laviron, C. Camel, J.-L. Santailler, and H. Akhouayri. Laser thermal processing using an optical coating for ultra shallow junction formation. *Mater. Sci. Eng. B*, 114:105–108, 2004.

[36] J. S. Hsiao. An efficient algorithm for finite difference analysis of heat transfer with melting and solidification. *Numerical Heat Transfer*, 8:653–666, 1985.

[37] K. Huet, G. Fisicaro, J. Venturini, H. Besaucèle, and A. La Magna. Defect kinetics and dopant activation in submicrosecond laser thermal processes. *Appl. Phys. Lett.*, 95(23):231901, 2009. doi: 10.1063/1.3268472. URL `http://link.aip.org/link/?APL/95/231901/1`.

[38] M. Jaraiz, G. H. Gilmer, J. M. Poate, and T. D. de la Rubia. Atomistic calculations of ion implantation in si: Point defect and transient enhanced diffusion phenomena. *Appl. Phys. Lett.*, 68:409, 1996.

[39] G. E. Jellison and D. H. Lowndes. Measurements of the optical properties of liquid silicon and germanium using nanosecond time-resolved ellipsometry. *Appl. Phys. Lett.*, 51:352–354, 1987.

[40] R. Kalyanaraman, T. E. Haynes, O. W. Holland, H. J. L. Gossmann, C. S. Rafferty, and G. H. Gilmer. Binding energy of vacancies to clusters formed in si by high-energy ion implantation. *Appl. Phys. Lett.*, 79(13):1983–1985, 2001. ISSN 00036951. doi: DOI:10.1063/1.1405814.

[41] A. Karma and W. J. Rappel. Quantitative phase-field modeling of dendritic growth in two and three dimensions. *Phys. Rev. E*, 57(4):4323–4349, 1998.

[42] K. F. Kelton, A. L. Greer, and C. V. Thompson. Transient nucleation in condensed systems. *J. Chem. Phys.*, 79(12):6261–6276, 1983. ISSN 00219606. doi: DOI:10.1063/1.445731. URL `http://dx.doi.org/doi/10.1063/1.445731`.

[43] Khaibulin. *Viniti*, 2061:74Dep, 1974.

[44] S. Kim and S. Anghaie. An effective conduction length model in the enthalpy formulation for the stefan problem. *International Communications in Heat and Mass Transfer*, 28:733–741, 2001.

[45] H. Kodera. Diffusion coefficients of impurities in silicon melt. *Jpn. J. Appl. Phys.*, 2(4):212–219, 1963. doi: 10.1143/JJAP.2.212. URL `http://jjap.jsap.jp/link?JJAP/2/212/`.

[46] M. Kuwahara, O. Suzuki, N. Taketoshi, Y. Yamakawa, T. Yagi, P. Fons, K. Tsutsumi, M. Suzuki, T. Fukaya, J. Tominaga, and T. Baba. Measurements of temperature dependence of optical and thermal properties of optical disk materials. *Jpn. J. Appl. Phys.*, 45(2B):1419–1421, 2006. doi: 10.1143/JJAP.45.1419. URL `http://jjap.jsap.jp/link?JJAP/45/1419/`.

[47] A. La Magna, S. Coffa, and L. Colombo. A lattice kinetic monte carlo code for the description of vacancy diffusion and self-organization in si. *Nucl. Instrum. Methods Phys. Res. B*, 148(1-4):262 – 267, 1999. ISSN 0168-583X. doi: DOI:10.1016/S0168-583X(98)00798-8. URL `http://www.sciencedirect.com/science/article/pii/S0168583X98007988`.

[48] A. La Magna, S. Coffa, and L. Colombo. Role of extended vacancy-vacancy interaction on the ripening of voids in silicon. *Phys. Rev. Lett.*, 82:1720–1723, 1999.

[49] A. La Magna, P. Alippi, V. Privitera, G. Fortunato, M. Camalleri, and B. G. Svensson. A phase-field approach to the simulation of the excimer laser annealing process in si. *J. Appl. Phys.*, 95:4806–4814, 2004.

[50] A. La Magna, P. Alippi, V. Privitera, S. Scalese, S. Pannitteri, G. Fortunato, and M. Camalleri. Material modifications induced by laser annealing in two-dimensional structures. *Appl. Phys. Lett.*, 84:4738–4740, 2004.

[51] A. La Magna, P. Alippi, V. Privitera, and G. Fortunato. Role of light scattering in excimer laser annealing of si. *Appl. Phys. Lett.*, 86:161905, 2005.

[52] A. La Magna, V. Privitera, G. Fortunato, M. Cuscunà, B. G. Svensson, E. Monakov, K. Kuitunen, J. Slotte, and F. Tuomisto. Vacancy generation in liquid phase epitaxy of si. *Phys. Rev. B*, 75:235201, Jun 2007. doi: 10.1103/PhysRevB.75.235201. URL `http://link.aps.org/doi/10.1103/PhysRevB.75.235201`.

[53] A. La Magna, G. Fisicaro, G. Mannino, V. Privitera, G. Piccitto, B. G. Svensson, and L. Vines. Defect and dopant kinetics in laser anneals of si. *Mater. Sci. Eng., B*, 154-155:35 – 38, 2008. doi: DOI:10.1016/j.mseb.2008.08.008. URL `http://www.sciencedirect.com/science/article/pii/S0921510708002833`.

[54] J. Lindhard and M. Scharff. Energy dissipation by ions in the kev region. *Phys. Rev.*, 124:128–130, Oct 1961. doi: 10.1103/PhysRev.124.128. URL `http://link.aps.org/doi/10.1103/PhysRev.124.128`.

[55] C. S. Liu, Z. G. Zhu, J. Xia, and D. Y. Sun. Molecular dynamics simulation of the local inherent structure of liquid silicon at different temperatures. *Phys. Rev. B*, 60(5):3194–3199, 1999.

[56] G. Mannino, A. La Magna, V. Privitera, J. S. Christensen, L. Vines, and B. G. Svensson. Boron electrical activation in crystalline si after millisecond nonmelting laser irradiation. *J. Electrochem. Soc.*, 155(8):H603–H605, 2008. doi: 10.1149/1.

2939129. URL `http://link.aip.org/link/?JES/155/H603/1`.

[57] G. Mannino, C. Spinella, R. Ruggeri, A. La Magna, G. Fisicaro, E. Fazio, F. Neri, and V. Privitera. Crystallization of implanted amorphous silicon during millisecond annealing by infrared laser irradiation. *Appl. Phys. Lett.*, 97(2):022107, 2010. ISSN 00036951. doi: DOI:10.1063/1.3459959. URL `http://dx.doi.org/doi/10.1063/1.3459959`.

[58] J. R. Meyer, M. R. Kruer, and F. J. Bartoli. Optical heating in semiconductors: Laser damage in ge, si, insb, and gaas. *J. Appl. Phys.*, 51(10):5513–5522, 1980. ISSN 00218979. doi: DOI: 10.1063/1.327469. URL `http://dx.doi.org/doi/10.1063/1.327469`.

[59] S. Mirabella, D. De Salvador, E. Bruno, E. Napolitani, E. F. Pecora, S. Boninelli, and F. Priolo. Mechanism of boron diffusion in amorphous silicon. *Phys. Rev. Lett.*, 100:155901, 2008.

[60] S. Mizuo, T. Kusaka, A. Shintani, M. Nanba, and H. Higuchi. Effect of si and sio2 thermal nitridation on impurity diffusion and oxidation induced stacking fault size in si. *J. Appl. Phys.*, 54:3860, 1983.

[61] E. V. Monakhov, B. G. Svensson, M. K. Linnarsson, A. La Magna, M. Italia, V. Privitera, G. Fortunato, M. Cuscunà, and L. Mariucci. The effect of excimer laser pretreatment on diffusion and activation of boron implanted in silicon. *Appl. Phys. Lett.*, 87:192109, 2005. doi: 10.1063/1.2126144.

[62] E. V. Monakhov, B. G. Svensson, M. K. Linnarsson, A. La Magna, M. Italia, V. Privitera, G. Fortunato, M. Cuscunà, and L. Mariucci. Boron distribution in silicon after multiple pulse excimer laser annealing. *Appl. Phys. Lett.*, 87(8):081901, 2005. doi: 10.1063/1.2032603. URL `http://link.aip.org/link/?APL/87/081901/1`.

[63] K. Ng. *Complete Guide to Semiconductor Devices.* McGraw-Hill, 1995.

[64] C. S. Nichols, C. G. Van de Walle, and S. T. Pantelides. Mechanisms of equilibrium and nonequilibrium diffusion of dopants in silicon. *Phys. Rev. Lett.*, 62:1049–1052, Feb 1989. doi: 10.1103/PhysRevLett.62.1049. URL `http://link.aps.org/doi/10.1103/PhysRevLett.62.1049`.

[65] E. L. Nolle. *Soviet Physics - Solid State*, 9:90, 1967.

[66] D. J. Norris, T. Walther, A. G. Cullis, M. Myronov, A. Dobbie, T. Whall, E. H. C. Parker, D. R. Leadley, B. D. Jaeger, W. Lee, M. Meuris, J. Watling, and A. Asenov. Tem analysis of ge-on-si mosfet structures with hfo2 dielectric for high performance pmos device technology. *Jour. of Phys.*, 209:012061, 2010.

[67] G. Olson and J. A. Roth. Kinetics of solid phase crystallization in amorphous silicon. *Mater. Sci. Rep.*, 3(1):1 – 77, 1988. ISSN 0920-2307. doi: 10.1016/S0920-2307(88)80005-7. URL `http://www.sciencedirect.com/science/article/pii/S0920230788800057`.

[68] C. Y. Ong, K. L. Pey, X. Li, X. C. Wang, C. M. Ng, and L. Chan. Laser annealing induced high ge concentration epitaxial sige layer in si1-xgex virtual substrate. *Appl. Phys. Lett.*, 93:041112, 2008.

[69] C. Y. Ong, K. L. Pey, K. K. Ong, D. X. M. Tan, X. C. Wang, H. Y. Zheng, C. M. Ng, and L. Chan. A low-cost method of forming epitaxy sige on si substrate by laser annealing. *Appl. Phys. Lett.*, 94:082104, 2009.

[70] K. K. Ong, K. L. Pey, P. S. Lee, A. T. S. Wee, Y. F. Chong, K. L. Yeo, and X. C. Wang. Formation of ultra-shallow p+/n junctions in silicon-on-insulator (soi) substrate using laser annealing. *Mater. Sci. Eng., B*, 114:25–28, 2004.

[71] C. J. Ortiz, P. Pichler, T. Faeuhner, F. Cristiano, A. Claverie, and B. Colombeau. A physically based model for the spatial and temporal evolution of self-interstitial agglomerates in ion-implanted silicon. *J. Appl. Phys.*, 96:4866, 2004.

[72] H. Park and J. W. Wilkins. Relative stability of extended interstitial defects in silicon: First-principles calculations. *Phys.*

Rev. B, 79:241203, Jun 2009. doi: 10.1103/PhysRevB.79.241203. URL `http://link.aps.org/doi/10.1103/PhysRevB.79.241203`.

[73] P. Pichler. *Intrinsic Point Defects, Impurities, and Their Diffusion in Silicon*. Springer, Wien, 2004.

[74] V. A. Pilipovich, G. D. Ivlev, Y. F. Morgun, N. V. Nechaev, V. I. Osinskii, and A. Y. Peshko. Formation of p-n junctions in gallium arsenide by laser irradiation. *Zhurnal Prikladnoi Spektroskopii*, 22:324–328, 1975. ISSN 0021-9037. URL `http://dx.doi.org/10.1007/BF00610077`. 10.1007/BF00610077.

[75] J. M. Poate and J. W. Mayer. *Laser Annealing of Semiconductors*. Academic, New York, 1982.

[76] J. S. C. Prentice. Coherent, partially coherent and incoherent light absorption in thin-film multilayer structures. *J. Phys. D: Appl. Phys.*, 33(24):3139, 2000. URL `http://stacks.iop.org/0022-3727/33/i=24/a=302`.

[77] V. Privitera, A. La Magna, G. Fortunato, L. Mariucci, M. Cuscunà, M. Camalleri, A. Magri, B. G. Svensson, and F. Simon. Integration of melting excimer laser annealing in power mos technology. *IEEE Transactions on Electronic Devices*, 54:852–860, 2007.

[78] M. Rappaz. Modeling of microstructure formation in solidification processes. *International Materials Reviews*, 34:93–198, 1989.

[79] M. T. Robinson. *Radiation effects and defects in Solids, Marlowe User's Guide*, volume 130-131. 1994.

[80] C. Sabatier, S. Rack, H. Beseaucèle, J. Venturini, T. Hoffmann, Y. Thomas, E. Rosseel, and J. Steenbergen. Laser annealing of double implanted layers for igbt power devices. *Proceedings of the 16th IEEE International Conference on Advanced Thermal Processing of Semiconductors, Las Vegas, NV*, pages 177–181, 2008.

[81] B. Sahli, K. Vollenweider, N. Zographos, and C. Zechner. Ab initio calculations of phosphorus and arsenic clustering parameters

for the improvement of process simulation models. *Mater. Sci. Eng., B*, 154-155:193 – 197, 2008. ISSN 0921-5107. doi: DOI:10.1016/j.mseb.2008.09.047. URL `http://www.sciencedirect.com/science/article/pii/S0921510708004042`.

[82] H. Sasaki, E. Tokizaki, K. Terashima, and S. Kimura. Density variation of molten silicon measured by an improved archimedian method. *Jpn. J. Appl. Phys.*, 33(Part 1, No. 7A): 3803–3807, 1994. doi: 10.1143/JJAP.33.3803. URL `http://jjap.jsap.jp/link?JJAP/33/3803/`.

[83] H. Sasaki, E. Tokizaki, K. Terashima, and S. Kimura. Density variations in molten silicon dependent on its thermal history. *Jpn. J. Appl. Phys.*, 33(Part 1, No. 11):6078–6081, 1994. doi: 10.1143/JJAP.33.6078. URL `http://jjap.jsap.jp/link?JJAP/33/6078/`.

[84] H. Sasaki, Y. Anzai, X. Huang, K. Terashima, and S. Kimura. Surface tension variation of molten silicon measured by the ring method. *Jpn. J. Appl. Phys.*, 34(Part 1, No. 2A):414–418, 1995. doi: 10.1143/JJAP.34.414. URL `http://jjap.jsap.jp/link?JJAP/34/414/`.

[85] H. Sasaki, A. Ikari, K. Terashima, and S. Kimura. Temperature dependence of the electrical resistivity of molten silicon. *Jpn. J. Appl. Phys.*, 34(Part 1, No. 7A):3426–3431, 1995. doi: 10.1143/JJAP.34.3426. URL `http://jjap.jsap.jp/link?JJAP/34/3426/`.

[86] H. Sasaki, E. Tokizaki, X. Huang, K. Terashima, and S. Kimura. Temperature dependence of the viscosity of molten silicon measured by the oscillating cup method. *Jpn. J. Appl. Phys.*, 34 (Part 1, No. 7A):3432–3436, 1995. doi: 10.1143/JJAP.34.3432. URL `http://jjap.jsap.jp/link?JJAP/34/3432/`.

[87] E. Schroer and M. Uematsu. Simulation of clustering and pile-up during post-implantation annealing of phosphorus in silicon. *Jpn. J. Appl. Phys.*, 38:7, 1999.

[88] W. Skorupa, T. Gebel, R. A. Yankov, S. Paul, W. Lerch, D. F. Downey, and E. A. Arevalo. Advanced thermal processing of

ultrashallow implanted junctions using flash lamp annealing. *J. Electrochem. Soc.*, 152(6):G436–G440, 2005. doi: 10.1149/1.1899268. URL `http://link.aip.org/link/?JES/152/G436/1`.

[89] C. Spinella, S. Lombardo, and F. Priolo. Crystal grain nucleation in amorphous silicon. *J. Appl. Phys.*, 84:5383, 1998.

[90] J. Stefan. Ueber die theorie der eisbildung, insbesondere ÃŒber die eisbildung im polarmeere. *Annalen der Physik*, 278(2):269–286, 1891. ISSN 1521-3889. doi: 10.1002/andp.18912780206. URL `http://dx.doi.org/10.1002/andp.18912780206`.

[91] D. Stiebel, P. Pichler, and N. E. B. Cowern. A reduced approach for modeling the influence of nanoclusters and 113 defects on transient enhanced diffusion. *Appl. Phys. Lett.*, 79(16):2654–2656, 2001. ISSN 00036951. doi: DOI:10.1063/1.1406147. URL `http://dx.doi.org/doi/10.1063/1.1406147`.

[92] S. R. Stiffler, P. V. Evans, and A. L. Greer. Interfacial transport kinetics during the solidification of silicon. *Acta Metallurgica et Materialia*, 40(7):1617 – 1622, 1992. ISSN 0956-7151. doi: 10.1016/0956-7151(92)90103-L. URL `http://www.sciencedirect.com/science/article/pii/095671519290103L`.

[93] P. A. Stolk, H. J. Gossmann, D. J. Eaglesham, D. C. Jacobson, C. S. Rafferty, G. H. Gilmer, M. Jaraiz, J. M. Poate, H. S. Luftman, and T. E. Haynes. Physical mechanisms of transient enhanced dopant diffusion in ion-implanted silicon. *J. Appl. Phys.*, 81:6031, 1997.

[94] S. Takeda. An atomic model of electron-irradiation-induced defects on {113} in si. *Jpn. J. Appl. Phys.*, 30(Part 2, No. 4A):L639–L642, 1991. doi: 10.1143/JJAP.30.L639. URL `http://jjap.jsap.jp/link?JJAP/30/L639/`.

[95] M. Tang, L. Colombo, J. Zhu, and T. D. de la Rubia. Intrinsic point defects in crystalline silicon: Tight-binding molecular dynamics studiesof self-diffusion, interstitial-vacancy recombination, and formation volumes. *Phys. Rev. B*, 55:14279–

14289, Jun 1997. doi: 10.1103/PhysRevB.55.14279. URL `http://link.aps.org/doi/10.1103/PhysRevB.55.14279`.

[96] M. Uematsu. Simulation of high-concentration phosphorus diffusion in silicon taking into account phosphorus clustering and pile-up. *Jpn. J. Appl. Phys.*, 38:6188, 1999. doi: 10.1143/JJAP.38.6188. URL `http://jjap.jsap.jp/link?JJAP/38/6188/`.

[97] P. J. Ungar, T. Halicioglu, and W. A. Tiller. Free energies, structures, and diffusion of point defects in si using an empirical potential. *Phys. Rev. B*, 50:7344–7357, Sep 1994. doi: 10.1103/PhysRevB.50.7344. URL `http://link.aps.org/doi/10.1103/PhysRevB.50.7344`.

[98] A. Ural, P. B. Griffin, and J. D. Plummer. Fractional contributions of microscopic diffusion mechanisms for common dopants and self-diffusion in silicon. *J. Appl. Phys.*, 85:6440, 1999.

[99] J. A. V. Vechten. *Laser and Electron-Beam Interactions with Solids*, 1982.

[100] V. C. Venezia, L. Pelaz, H. J. L. Gossmann, T. E. Haynes, and C. S. Rafferty. Binding energy of vacancy clusters generated by high-energy ion implantation and annealing of silicon. *Appl. Phys. Lett.*, 79:1273, 2001.

[101] V. R. Voller and C. Swaminathan. Fixed grid techniques for phase change problems: a review. *International Journal for Numerical Methods in Engineering*, 30:875–898, 1990.

[102] H. C. Webber, A. G. Cullis, and N. G. Chew. Computer simulation of high speed melting of amorphous silicon. *Appl. Phys. Lett.*, 43(7):669–671, 1983. doi: 10.1063/1.94440. URL `http://link.aip.org/link/?APL/43/669/1`.

[103] A. A. Wheeler, W. J. Boettinger, and G. B. McFadden. Phase-field model for isothermal phase transitions in binary alloys. *Phys. Rev. A*, 45:7424–7439, May 1992. doi: 10.1103/PhysRevA.45.7424. URL `http://link.aps.org/doi/10.1103/PhysRevA.45.7424`.

[104] A. A. Wheeler, W. J. Boettinger, and G. B. McFadden. Phase-field model of solute trapping during solidification. *Phys. Rev. E*, 47(3):1893–1909, Mar 1993. doi: 10.1103/PhysRevE.47.1893.

[105] S. Whelan, A. La Magna, V. Privitera, G. Mannino, M. Italia, C. Bongiorno, G. Fortunato, and L. Mariucci. Dopant redistribution and electrical activation in silicon following ultra-low energy boron implantation and excimer laser annealing. *Phys. Rev. B*, 67:075201, Feb 2003. doi: 10.1103/PhysRevB.67.075201. URL `http://link.aps.org/doi/10.1103/PhysRevB.67.075201`.

[106] R. F. Wood, J. R. Kirkpatrick, and G. E. Giles. Macroscopic theory of pulsed-laser annealing. ii. dopant diffusion and segregation. *Phys. Rev. B*, 23:5555–5569, May 1981. doi: 10.1103/PhysRevB.23.5555. URL `http://link.aps.org/doi/10.1103/PhysRevB.23.5555`.

[107] R. F. Wood, C. W. White, and R. T. Young. *Semiconductors and Semimetals*, volume 23. Academic, New York, 1984.